

https://dspace.org/

Reciprocating wear of WC-6 wt.% Co alloys in synthetic mine water

Makhwathana, Ntakandzeni Phanuel

2016

http://hdl.handle.net/10539/20636

Downloaded from a DSpace repository. https://dspace.org/

Reciprocating wear of WC-6 wt. % Co alloys in synthetic mine water

Ntakadzeni Phanuel Makhwathana

A research report submitted to the Faculty of Engineering and the Built Environment, of the University of the Witwatersrand, Johannesburg, South Africa in partial fulfilment of the Masters of Science in Engineering

Declaration

I hereby declare that the contents of this report are my own unaided work, except for the work properly referenced

Name : Makhwathana Ntakadzeni

Student no : 0708849E

Signature : 

Date : 24 February 2016

Abstract

The focus in this study was to conduct an investigation on the corrosive wear behaviour of WC-6 wt.% Co hardmetals used for drilling in a mining environment. The wear behaviour was characterised by sliding the WC-6 wt.% Co buttons against 3CR12 stainless steel and mild steel, in a ball-on-flat configuration (ASTM G133) in synthetic mine water, with distilled water as a reference solution, and identifying the wear mechanisms. Standard potentio-dynamic corrosion tests were conducted to determine the corrosion behaviour. The WC-6 wt.% Co experienced higher wear rates when sliding against 304L stainless steel than mild steel. The dimensional wear rate coefficient indicated that the WC-6 wt.% Co/3CR12 sliding system was 52% more severe than the WC-6wt.% Co/mild steel system. Discolouration of both the WC-6 wt.% Co and the steel counterfaces were noted as evidence of chemical reactions during sliding. The wear mechanism of the steel counterfaces was severe plastic deformation, followed by groove formation caused by ploughing. The wear mechanism of the WC-6 wt.% Co was characterized by the removal of the cobalt binder matrix, followed by micro-cracking of the exposed WC grains. Adhesion of the steels to the WC-6 wt.% Co buttons was confirmed by EDS analysis. The corrosion rate of WC-6 wt.% Co was found to be 40% more in synthetic mine water when compared to the distilled water reference solution and indicated pseudo passivation behavior. Synthetic mine water showed an aggressive corrosive-wear synergism in the carbide-steel sliding systems, which led to a reduction in life of the materials.

Acknowledgements

1. Prof. N Sacks (Supervisor)

2. Dineo Lioma

3. Dr J van der Merwe

4. Mr N Nelwalani

5. Tshiwela Makhwathana (Wife)

I wish to extend my gratitude to the above mentioned people for their contributions and support towards making my research project a success, may ALMIGHTY ELOHIM be with you all the time and may all your righteous wishes comes true in his name.

Table of Contents

Declaration……i

Abstract……..ii

Acknowledgements……...iii

Table of Contents……..iv

List of Figures……..viii

List of Tables……xiv

Introduction……...1

1.1 Research aim and objectives 2

1.2 Layout of report.....3

Literature Review……..4

2.1 WC-Co hardmetals.....4

2.2.2 General overview 4
2.1.2 Manufacturing process of WC-Co hardmetals 5
2.1.3 WC-Co alloy constituents.....6
2.1.4 Application of cemented carbides.....9
2.1.5 Properties of WC-Co alloy.....11

2.2 Wear 14

2.2.1 Reciprocating sliding wear 14
2.2.2 Wear of WC-Co hardmetals.....16

2.3 Corrosion of WC-Co alloys.....20

2.3.1 Corrosion and corrosive wear 20
2.3.2 Corrosion of cobalt 20
2.3.3 Corrosion and corrosive wear of WC-Co hardmetals.....21

Experimental Procedure…….23

3.1 Material characterization.....23

3.1.1 Materials 23
3.1.2 Sample preparation 24
3.1.3 Hardness.....25
3.1.4 Fracture toughness 26
3.1.5 Density and porosity 26
3.2.2 Microstructure.....27
3.1.7 Phase analysis 28

3.2 Reciprocating sliding wear tests.....28

3.2.1 Test description.....28
3.2.2 Wear rate calculations.....30

3.3 Corrosion tests.....32

3.3.1 Sample preparation 32
3.3.2 Test Procedure 32

3.4 Examination of wear scars 34

Results……...35

4.1 Material characterisation.....35

4.1.1 Microstructural analysis.....35
4.1.2 Phase analysis 37
4.1.3 Material properties.....43

4.2 Reciprocating wear.....44

4.2.1 Wear of mild steel and 3CR12 stainless steel in distilled and synthetic mine water 44
4.2.2 Wear of WC-6 wt. % Co buttons in distilled water and synthetic mine water ..53

4.3 Wear scar analyses 55

4.3.1 Typical wear tracks 55
4.3.2 Wear scars of mild steel and WC-6 wt.% Co buttons in distilled water and synthetic mine water 56
4.3.2 Wear scars of the stainless steel counterface and WC-6 %wt. Co in distilled water and synthetic mine water 63

4.4 Corrosion tests 70

4.2.1 Corrosion of WC-6 wt.% Co buttons 70
4.4.2 Corrosion of 3CR12 stainless steel 72
4.4.3 Corrosion of mild steel 74
4.4.4 Corrosion rates comparison of WC-6wt%Co buttons, mild steel and 3CR12 stainless steel 76

Discussion……78

5.1 Microstructural analysis……78

5.2 Corrosion behavior of the test materials 79

5.2.1 Corrosion of WC-6 wt.% Co buttons 79
5.2.2 Corrosion of 3CR12 stainless steel 80
5.2.3 Corrosion of mild steel 80
5.2.4 Comparison of corrosion response of test materials 81

5.3 Reciprocating wear of the test materials 81

5.3.1 Reciprocating wear synergism between WC-6 wt.% Co and mild steel 82
5.3.2 Reciprocating wear synergism between WC-6 wt.% Co and 3CR12 stainless steel……..83
5.3.3 Comparison of the corrosive wear synergisms of the WC-6 wt.% Co buttons sliding against mild steel and 304L stainless steel 84

5.4 Experimental testing error 86

Conclusions……...87

Future studies……...89

References…….90

Appendix A: Hardness test data…….94

Appendix B: Fracture toughness data……96

Appendix C: Density and porosity data……..97

Appendix D: Reciprocating wear data……98

Appendix E: Contact areas of WC-6 wt.% Co buttons and steel counterfaces during wear testing……104

Appendix F: Corrosion data and repeatability polarization curves……...106

Appendix G: SEM images of the wear scars…….111

Appendix H: Corrosion surface…….117

List of Figures

Figure 2. 1: Statistical overview of elemental tungsten consumption in various fields [4].....4

Figure 2. 2:The direct carburization production process for WC [4]. 7

Figure 2. 3: Illustration of the effect of cobalt content on properties of cemented carbides [1]. 8

Figure 2. 4: Field of application of cemented carbides and their percent distribution in engineering sector [4]. 9

Figure 2. 5: Modern button bit tools for drilling purposes [4].....11

Figure 2. 6: Load and crack length relationship as a function of material surface preparation [27].....13

Figure 2. 7: Wear regime map for unlubricated sliding of steel on steel in the pin on disc [32]. 16

Figure 2. 8: Wear resistance vs. hardness of WC-Co alloys [34].....17

Figure 2. 9: The volume loss vs. binder content of WC-Co hardmetals in dry and wet wear conditions [12]. 18

Figure 2. 10: A SEM micrograph showing wear mechanism of WC-Co hardmetals [35].....19

Figure 2. 11: The pH and potential relationship for Co in aqueous solution at 25°C [39].....21

Figure 2. 12: Corrosion resistance of cemented carbides as a function of pH [1].....22

Figure 3. 1: Physical appearance of the cemented carbide buttons……..23

Figure 3. 2: Physical appearance of the steel counterfaces.....24

Figure 3. 3: The reciprocating wear testing machine. 29

Figure 3. 4: Configuration for buttons' worn volume calculations [1].....31

Figure 3. 5: Corrosion test set-up.....33

Figure 3. 6: Schematic showing the Tafel plots from which the values of I_{corr} and E_{corr} is determined [26].....34

Figure 4. 1: Optical micrograph of the 3CR12 stainless steel sample at 50X magnification..35
Figure 4. 2: Optical microstructure of the mild steel sample at 50X magnification.....36
Figure 4. 3: An SEM microstructure of the WC- 6wt.% Co cemented carbide button at 2500 magnification. 37
Figure 4. 4: XRD pattern for the mild steel in an as received condition. 37
Figure 4. 5: XRD pattern for the 3CR12 stainless steel in an as received condition.....38
Figure 4. 6: EDS for the mild steel sample (a) Scanned spectrum area (b) spectrum analysis. 39
Figure 4. 7: EDS for the 3CR12 stainless steel sample (a) Scanned spectrum area (b) spectrum analysis. 40
Figure 4. 8: XRD pattern for the WC-6 wt.% Co buttons in an as received condition. 41
Figure 4. 9: EDS for the WC-6 wt.% Co button (a) Scanned spectrum area (b) spectrum analysis.....42
Figure 4. 10: Cumulative volume loss of the mild steel sliding against WC-6 wt.% Co buttons in distilled water.....44
Figure 4. 11: Cumulative volume loss for the mild steel sliding against WC-6 wt.% Co buttons in synthetic mine water. 45
Figure 4. 12: Comparison of the cumulative volume loss of the mild steel sliding against WC-6 wt.% Co in distilled water and synthetic mine water.....46
Figure 4. 13: Wear rate coefficient of the mild steel sliding against WC-6 wt.% Co buttons in distilled water.....47
Figure 4. 14: Wear rate of the mild steel sliding against WC-6 wt.% Co buttons in synthetic mine water.....47
Figure 4. 15: Comparison of the wear coefficient of the mild steel sliding against WC-6 wt.% Co buttons in distilled and synthetic mine water. 48

Figure 4. 16: Cumulative volume loss of the 3CR12 stainless steel sliding against WC-6 wt.% Co buttons in distilled water. 49
Figure 4. 17: Cumulative volume loss of the 3CR12 stainless steel sliding against WC-6 wt.% Co buttons in synthetic mine water solution. 49
Figure 4. 18: Cumulative volume loss of the 3CR12 stainless steel sliding against WC-6 wt.% Co buttons in distilled water and synthetic mine water solutions. 50
Figure 4. 19: Wear rate coefficient of the 3CR12 stainless steel sliding against WC-6 wt.% Co buttons in distilled water solution. 51
Figure 4. 20: Wear rate coefficient of the 3CR12 stainless steel sliding against WC-6 wt.% Co buttons in synthetic mine water solution. 51
Figure 4. 21: Comparison of wear rate coefficient for the 3CR12 stainless steel sliding against WC-6 wt.% Co in distilled water and synthetic mine water solutions. 52
Figure 4. 22: Comparison of the wear rate coefficients of the mild steel and 3CR12 stainless steel in distilled water and synthetic mine water solutions. 53
Figure 4. 23: Comparison of the average material volume loss of the WC- 6wt. % Co buttons sliding against mild steel and 3CR12 stainless steel in distilled water and synthetic mine solutions. 54
Figure 4. 24: Comparison of the average material volume loss of the WC-6 wt.% Co buttons sliding against mild steel and 3CR12 stainless steel in distilled water and synthetic mine solutions. 54
Figure 4. 25: Typical wear track on the steel counterfaces caused by the WC-6 wt.% Co buttons during sliding. 55
Figure 4. 26: Typical wear scar on the WC-6 wt.% Co buttons caused by the sliding action. 56
Figure 4. 27: Wear scars of mild steel sample sliding against WC-6 wt.% Co, (a) and (b) in distilled water, (c) and (d) in synthetic mine water. 57

Figure 4. 28: EDS analyses on the wear scar of the mild steel in distilled water (a) spectrum area (b) spectrum analysis.....58
Figure 4. 29: EDS analyses on the wear scar of the mild steel in synthetic mine water (a) Scanned spectrum area (b) spectrum analysis. 59
Figure 4. 30: Wear scars of WC-6 wt.% Co button sliding against mild steel, (a) & (b) in distilled water and (c) & (d) in synthetic mine water. 60
Figure 4. 31: EDS analyses on the wear scar of the WC-6 wt.% Co in distilled water (a) Scanned spectrum area (b) spectrum analysis. 61
Figure 4. 32: EDS analyses on the wear scar of the WC-6 wt.% Co in synthetic mine water (a) Scanned spectrum area (b) spectrum analysis. 62
Figure 4. 33: Wear scars of 3CR12 stainless steel, (a), (b) in distilled water and (c), (d) in synthetic mine water. 63
Figure 4. 34: EDS analyses on the wear scar of the 3CR12 stainless steel in distilled water (a) Scanned spectrum area (b) spectrum analysis. 64
Figure 4. 35: EDS analyses on the wear scar of the 3CR12 stainless steel in synthetic mine water (a) Scanned spectrum area (b) spectrum analysis. 65
Figure 4. 36: Wear scars of WC-6 wt.% Co buttons (a) & (b) in distilled water, (c) & (d) in synthetic mine water. 67
Figure 4. 37: EDS analyses on the wear scar of the WC-6 wt.% Co in distilled water (a) Scanned spectrum area (b) spectrum analysis. 68
Figure 4. 38: EDS analyses on the wear scar of the WC-6 wt.% Co in synthetic mine water (a) Scanned spectrum area (b) spectrum analysis. 69
Figure 4. 39: Comparison of the potentiodynamic curves of the WC-6 wt.% Co buttons in distilled water and synthetic mine water. 71
Figure 4. 40: Comparison of corrosion rates for the WC-6 wt.% Co buttons. 72

Figure 4. 41: Comparison of potentio-dynamic curves for 3CR12 stainless steel in distilled and synthetic mine water. 73

Figure 4. 42: Comparison of corrosion rates for 3CR12 stainless steel in distilled water and synthetic mine water. 74

Figure 4. 43: Comparison of potentiodynamic curves of the mild steel in distilled and synthetic mine water. 75

Figure 4. 44: Comparison of corrosion rates for the mild steel in distilled water and synthetic mine water.....76

Figure 4. 45: Corrosion rates of all samples in distilled and synthetic mine water. 77

Figure E. 1: Wear scar contact area for the WC-6 wt.% Co buttons sliding against mild steel in distilled water, (b) synthetic mine water……104

Figure E. 2: Wear scar contact area for the WC-6 wt.% Co buttons sliding against 3CR12 stainless steel in (a) distilled water, (b) synthetic mine water. 104

Figure E. 3: Wear tracks produced by the WC-6 wt.% Co buttons on mild steel in (a) distilled water, (b) synthetic mine water.....105

Figure E. 4: Wear tracks produced by the WC-6 wt.% Co on 3CR12 stainless steel in (a) distilled water, (b) synthetic mine water.....105

Figure F. 1: Polarisation curves for WC-6 wt.% Co showing repeatability in distilled water…….....107

Figure F. 2: Polarisation curves for the WC-6 wt.% Co showing repeatability in synthetic mine water.....107

Figure F. 3: Polarisation curves for the 3CR12 stainless steel showing repeatability in distilled water.....108

Figure F. 4: Polarisation curves for the 3Cr12 stainless steel showing repeatability in synthetic mine water. 108

Figure F. 5: Polarisation curve for the mild steel in distilled water.....109
Figure F. 6: Polarisation curve for the mild steel in distilled water.....109
Figure F. 7: Polarisation curve for the mild steel in synthetic mine water. 110
Figure F. 8: Polarization curve for the mild steel in synthetic mine water. 110
Figure G. 1: Wear scars on mild steel sliding against WC-6 wt.% Co buttons in distilled water (a and b) Plane view, (c and d) cross section view……...111
Figure G. 2: Wear scars on mild steel sliding against WC-6 wt.% Co buttons in distilled water (a and b) plane view, (C and d) cross section view) 112
Figure G. 3: Wear scars on 3CR12 stainless steel sliding against WC-6 wt.% Co in distilled water (a and b) plane view, (c and d) cross section view. 113
Figure G. 4: Wear scars on 3CR12 stainless steel sliding against WC-6 wt.% Co buttons in synthetic mine water (a and b) plane view, (c and d) cross section view. 114
Figure G. 5: Wear scars on WC-6 wt.% Co sliding against mild steel in (a and b) distilled water, (c and d) synthetic mine water. 115
Figure G. 6: Wear scars on WC-6 wt.% Co sliding against 3CR12 stainless steel in (a and b) distilled water, (c and d) synthetic mine water. 116
Figure H. 1: Corroded surface for the 3CR12 stainless steel.……117

List of Tables

Table 3. 1: WC-6 wt.% Co button composition and dimensions.....23

Table 3. 2: Chemical composition of steel counterfaces 24

Table 3. 3: Grinding and polishing routine for WC-6 wt.% Co buttons.....25

Table 3. 4: Composition of Murakami's reagent [26] 27

Table 3. 5: Composition of synthetic mine water [40]. 30

Table 3. 6: A summary of wear test parameters. 30

Table 3. 7: A summary of corrosion test parameters. 33

Table 4. 1: Elemental composition for the mild steel sample. 39

Table 4. 2: Elemental composition for 3CR12 stainless steel. 40

Table 4. 3: Elemental composition for WC-6 wt.% Co buttons. 42

Table 4. 4: Mechanical and physical properties of the WC-6 wt.% Co Buttons. 43

Table 4. 5: Material properties of the mild steel and 3CR12 stainless steel. 43

Table 4. 6: Elemental composition of mild steel wear scar in distilled water. 58

Table 4. 7: Elemental composition of mild steel wear scar in synthetic mine water. 59

Table 4. 8: Elemental composition on WC-6 wt.% Co button wear scar in distilled water. ...61

Table 4. 9: Elemental composition on cemented carbide button wear scar in synthetic mine water. 62

Table 4. 10: Elemental composition on 3CR12 stainless steel wear scar in distilled water. ...65

Table 4. 11: Elemental composition on 3CR12 stainless steel wear scar in synthetic mine water. 66

Table 4. 12: Elemental composition on WC-6 wt.% Co button wear scar in distilled water. .68

Table 4. 13: Elemental composition on WC-6 wt.% Co button wear scar in synthetic mine water. 69

Table 4. 14: Electrochemical corrosion parameters of the WC-6 wt.% Co buttons. 71

Table 4. 15: Electrochemical corrosion parameters for 3CR12 stainless steel. 73

Table 4. 16: Electrochemical corrosion parameters for mild steel. 75

Table 5. 1: Wear coefficients for the sliding pairs in synthetic mine water. 85

Table A. 1: Vickers hardness test data for WC-6 wt.% Co sample 1. 94

Table A. 2: Vickers hardness test data for WC-6 wt.% Co sample 2. 94

Table A. 3: Vickers hardness test data for mild steel. 95

Table A. 4: Vickers hardness test data for 3CR12 stainless steel. 95

Table B. 1: Fracture toughness data for WC-6 wt.% Co buttons 96

Table C. 1: Density data for the WC-6 wt.% Co buttons 97

Table C. 2: Density data for the mild steel. 97

Table C. 3: Density data for the 3CR12 stainless steel. 97

Table D. 1: Mass loss data for the mild steel sliding against WC-6 wt.% Co in distilled water 98

Table D. 2: Volume loss data for the mild steel sliding against WC-6 wt.% Co in distilled water. 98

Table D. 3: Wear rate coefficient data for the mild steel sliding against WC-6 wt.% Co in distilled water. 99

Table D. 4: Mass loss data for the mild steel sliding against WC-6 wt.% Co in synthetic mine water. 99

Table D. 5: Volume loss data for the mild steel sliding against WC-6 wt.% Co in synthetic mine water. 99

Table D. 6: Wear rate coefficient data for the mild steel sliding against WC-6 wt.% Co in synthetic mine water. 100

Table D. 7: Mass loss data for the 3CR12 stainless steel sliding against WC-6 wt.% Co in distilled water. 100

Table D. 8: Volume loss data for the 3CR12 stainless steel sliding against WC-6 wt.% Co in distilled water. 100
Table D. 9: Wear rate coefficient data for the 3CR12 stainless steel sliding against WC-6 wt.% Co in distilled water. 101
Table D. 10: Mass loss data for the 3CR12 stainless steel sliding against WC-6 wt.% Co in synthetic mine water. 101
Table D. 11: Volume loss data for the 3CR12 stainless steel sliding against WC-6 wt.% Co in synthetic mine water. 101
Table D. 12: Wear rate coefficient data for the 3CR12 stainless steel sliding against WC-6 wt.% Co in synthetic mine water. 102
Table D. 13: Wear data for the WC-6 wt.% Co button sliding against mild steel counterfaces in distilled water. 102
Table D. 14: Wear data for the WC-6 wt.% Co buttons sliding against mild steel counterfaces in synthetic mine water. 102
Table D. 15: Wear data of the WC-6 wt.% Co buttons sliding against 3CR12 stainless steel counterfaces in distilled water. 103
Table D. 16: Wear data for the WC-6 wt.% Co buttons sliding against 3CR12 stainless steel counterfaces in synthetic mine water. 103
Table F. 1: Corrosion data for the WC-6 wt.% Co buttons 106
Table F. 2: Corrosion data for the 3CR12 stainless steel. 106
Table F. 3: Corrosion data for the mild steel. 106

CHAPTER 1

Introduction

Cemented tungsten carbides, also known as hardmetals are powder metallurgically sintered materials, whose properties, i.e. hardness, toughness, wear resistance and thermal stability, have made them successfully suitable for use in industrial applications such as metal cutting, aerospace, mining and rock drilling [1-3]. In this alloy, the high hardness and wear resistance is provided by the tungsten carbide (WC) phase, which is cemented by the ductile binder, typically cobalt (Co) phase [4]. In a mining environment, specifically in rotary percussive drilling and rotary crushing drilling, WC-Co inserts are used to facilitate rock drilling by a crushing and sliding action against the rocks [5]. During this drilling process the cemented carbides inserts experience very complex operating conditions caused by the variation in rock properties resulting in impact, wear and spalling [5]. These factors can lead to a reduction in the insert's design life and may cause premature failure [6]. One type of wear mechanism experienced during the drilling process is reciprocating wear due to the sinusoidal drilling action. According to Finger *et al* [7], in percussion drilling a reciprocating downhole piston assembly is used to apply impact loading either to a convectional roller-cone bit or to a one piece bit set with tungsten carbide inserts.

Due to the vast application of WC-Co hardmetals in the mining industry, it is important to study, and further understand the wear behaviour of these materials in this aggressive environmental condition. This is primarily due to the fact that wear is not an intrinsic material property, but a system property [8], meaning that a slight change in environment influences the wear behaviour, which may also lead to a change in the failure mechanisms. According to Glaeser *et al* **[**8**],** understanding the operating variables and wear behaviour of materials under service conditions is important when trying to solve wear problems.

Several studies have been conducted to determine the wear and corrosion behaviour of WC-Co hardmetals when used as drill bit inserts in the mining environment. Hardness of the counterface has been found to have an influence on wear of cemented carbides [9]. The general wear mechanisms from studies done indicated that the cobalt binder is

selectively removed leaving the WC grains exposed to further wear which often results in fracture of the grains [1,9-12]. The use of nanostructured cemented carbides has been seen to provide high hardness and high wear resistance which may improve the service life of drill bits [13]. Corrosion has also been found to be one of the surface degradation processes of cemented carbides in some mining applications [7]. Corrosion studies have indicated that the corrosion behaviour depends mainly on the pH of the environment [1, 14]. It has been shown that low pH values causes the Co binder to be dissolved into the solution leaving, the WC grains exposed, which may result in higher wear rates [14].

To author's knowledge no publication have been done to assess the corrosive wear behaviour of WC-Co alloys in a mining environment under controlled reciprocating wear conditions. Therefore this aspect was selected as a focus of the current research project. Reciprocating wear tests and corrosion tests of WC-6wt% Co inserts were conducted in order to assess the synergistic effect of corrosion and wear of the material in the mining environment. Two industrial steels were used as the counterfaces in the wear tests, since the rock material proved difficult to machine to the required dimensions. Synthetic mine water simulated the mining environment, while distilled water was used as a standard control, against which the aggressiveness of mine water solution was compared. The outcome of this project contributes to the current knowledge base and provides better understanding of wear mechanisms experienced by those inserts during mining operations.

1.1 Research aim and objectives

The aim of this study was to conduct an investigation on the corrosive wear behaviour of WC-6 wt. % Co hardmetals used for drilling in a mining environment. This aim was achieved through the following objectives:

- Assessing the reciprocating wear behaviour of WC-6 wt.% Co alloys in synthetic mine water and identifying the wear mechanisms;
- Determining the corrosion response of WC-6 wt.% Co alloys in synthetic mine water and identifying the corrosion mechanisms;
- Characterizing the microstructure of the alloy prior to testing and after testing;
- Evaluating the synergistic effect of corrosion and wear

1.2 Layout of report

The remainder of this report is structured as follows: Chapter 2 provides a literature review of cemented carbides in terms of the manufacturing process, general material properties, industrial applications, and wear and corrosion characteristics. Descriptions of the experimental procedures are addressed in Chapter 3. The results are presented in Chapter 4 and discussed in chapter 5. The conclusions drawn from the research are given in Chapter 6, while recommendations for the future work are listed in Chapter 7. Detailed test results are provided in Appendices A to H.

Chapter 2

Literature Review

A literature review was conducted to understand the structure and nature of cemented tungsten carbide materials, their industrial applications, wear and corrosion properties. This background research focused on important aspects from published research done on cemented carbides. The findings from the various studies are discussed in this chapter.

2.1 WC-Co hardmetals

2.2.2 General overview

Cemented carbides represent a group of hardmetals and wear resistant refractories in which hard carbide particles are cemented together by a ductile and tough binder matrix. The discovery of this material increased elemental tungsten consumption worldwide to about 58 % [4] as indicated in figure 2.1. These hardmetals combine high hardness and strength from the WC, with toughness and plasticity from the Co matrix. WC-Co hardmetal properties can be tailor-made to suit different applications by adjusting the composition of the cobalt binder and/or by the addition of other metals such as vanadium (V), chromium (Cr), titanium (Ti) and tantalum (Ta). [4]. In this project, only WC-Co alloys were studied, and therefore the remainder of this review is based on this alloy system.

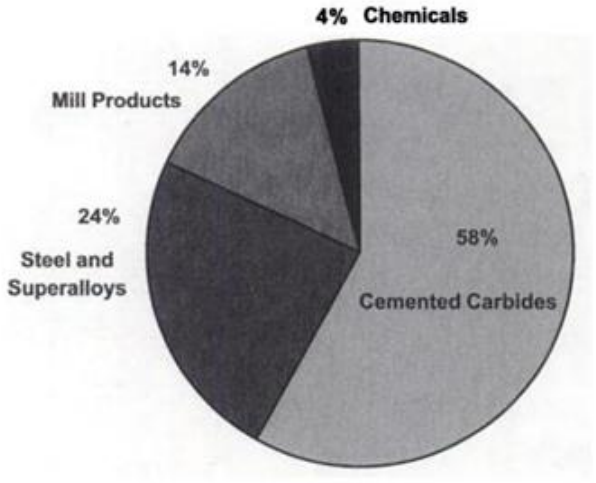


Figure 2. 1: Statistical overview of elemental tungsten consumption in various fields [4].

2.1.2 Manufacturing process of WC-Co hardmetals

The manufacturing process and the final microstructure formed influence the properties of the cemented carbides. Tungsten carbide alloys are produced by powder metallurgical processes, where the carbide powders are mixed with either a Co or Ni binder depending on the application requirement [15]. The production of cemented carbides involves several steps:

- Milling,
- Pressing,
- Pre-sintering and
- Sintering.

Milling involves mixing of the WC particles and Co binder according to the required composition [4]. The milling process is normally done in ball, attritor or vibratory mills [1**,** 5]. This process in done to ensure the following:

- Reduction of the powder particle size,
- Provide uniformity of the mixture to ensure that each WC particle is coated with Co.

Upadhyaya [5] indicated that the mechanical properties, and elimination of porosity from sintered products, depend on the uniformity from the mixing process. In most cases, milling is normally done in slurry conditions, to reduce temperature and prevent oxidation of the powder. Agents like water, alcohol and acetone. are used as milling media. The milled product is filtered by vacuum or centrifuge, and then spray dried to remove the milling medium. Annealing may also be done to remove any oxygen pick up by the powder during milling [16].

Several techniques have been devised for pressing or compaction of cemented carbide grades, varying from semi to automatic press machines. The tooling used in pressing includes tungsten carbide dies, punches or core rods which have high wear resistances [1]. The compaction is done using external pressure and the product from this stage is called a green compact due to the fact that it is un-sintered [5,15]. The compaction process gives shape to the green compact and offers dimensional control. A green

density of up to 60 % of the theoretical density can be achieved for a given hardmetal composition [5, 16].

Pre-sintering is carried out before final sintering to provide a measure of stability to the green compact. In this stage a certain amount of strength is obtained and the compact is able to maintain its shape. The process is normally done in a temperature range of 750 ^{o}C - 1000 °C [5].

Sintering of cemented carbides is performed under controlled inert conditions to prevent oxidation [5]. The temperature range of this process is 1300 ^{o}C -1600 ^{o}C, but the precise temperature depends on the amount of Co present. The final sintering temperature is where the binder melts, and therefore this process is called liquid phase sintering. Liquid phase sintering promotes the coalescence of WC particles and produces a fully dense and low porosity microstructure [1]. Eutectic liquid forms at 1320 ^{o}C in the WC-Co system [1, 5, 16]. During sintering, cobalt diffuses between the carbide particles and an increase in temperature may cause the WC to dissolve in the Co. The dissolution of WC particles is temperature dependent, and upon cooling the WC particles precipitate out of the binder phase. The stoichiometric carbon content of the alloys should be 6.13 wt.%. It has been reported that any deviation from this value will influence the quality of the alloy by formation of undesired products. When the C is < 6.13 wt%, then carbon precipitates out in form of graphite resulting in porosity thereby lowering fracture toughness, and when the C is > 6.13 wt%, then the brittle η - phase precipitates, which reduces the transverse rupture strength [16].

2.1.3 WC-Co alloy constituents

The WC-Co alloys consist of two phases, namely WC and Co, which are respectively known as the hard carbide component and the binder metal. The cobalt content is varied depending on the application with a range of 3-10 wt. % in cutting applications and up to 30 wt. % in wear part applications [4].

a. Tungsten carbide (WC)

WC is a composite material which shows little or no plastic deformation, and is technically classified as brittle [17]. There are two types of individual carbides that can

be established in the W-C system, namely W_2C and WC. Their crystal structures have been confirmed by diffraction studies with W_2C being rhombic while WC is a simple hexagonal structure [5]. WC decomposes at 2600 $^{\circ}$C and W_2C melts at 2750 $^{\circ}$C. Both carbides are very hard and brittle. This material can be melted and cast, but the challenge is the formation of a coarse structure having many flaws which would fracture easily [2]. The powder metallurgy route became the preferred manufacturing process which could maximize the hardness and wear resistance properties possessed by WC [2].

WC can be produced by several processes including carburization, chemical vapor reactions and spray conversion [5]. Each production process has an effect on the size of the WC particles/grains that are produced. Figure 2.2 illustrates the direct carburization process that leads to WC as the final product [4].

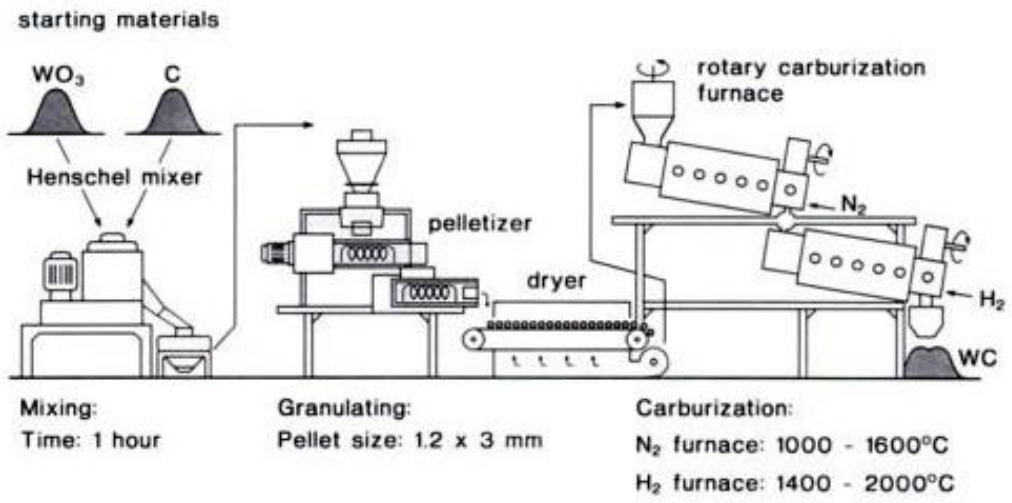


Figure 2. 2:The direct carburization production process for WC [4].

Parameters such as time, temperature and hydrogen flow rate must be regulated since they affect powder characteristics such as grain size distribution, apparent density and compaction behaviour [4]. WC grains can be classified as ultrafine, submicron or nano-sized [4-5]. The size of the WC grains plays a major role in determining the mechanical properties of the cemented carbides. It has been shown that at constant binder content, the hardness and abrasion wear resistance decreases, as the WC grain size increases [15**,** 18].

b. Cobalt (Co)

Co is the predominant binder used in hardmetals due to its outstanding wetting and adhesive characteristics on the WC grains [1-2]. Co has a low temperature hexagonal phase and a high temperature face centred cubic phase which occurs at a transition temperature of 415 °C [1]. Purity, dissolved tungsten and rate of temperature change determine the temperature at which the allotropic transformation occurs [5]. In sintered cemented carbides containing WC, Co has a cubic lattice which cannot be transformed by annealing due to the stabilization of the cubic phase by the dissolved W and C [5]. The manufacturing of Co generally involves a reduction process of cobalt oxides, or it can be derived from organic salts; particularly cobalt oxalate [1]. Figure 2.3 illustrates the influence of cobalt content up to 30% on the mechanical properties of cemented carbides. The hardness and density decreases with increase in cobalt content whereas the fracture and transverse rupture strength increase with increase with increase in Cobalt content [1, 15, 18].

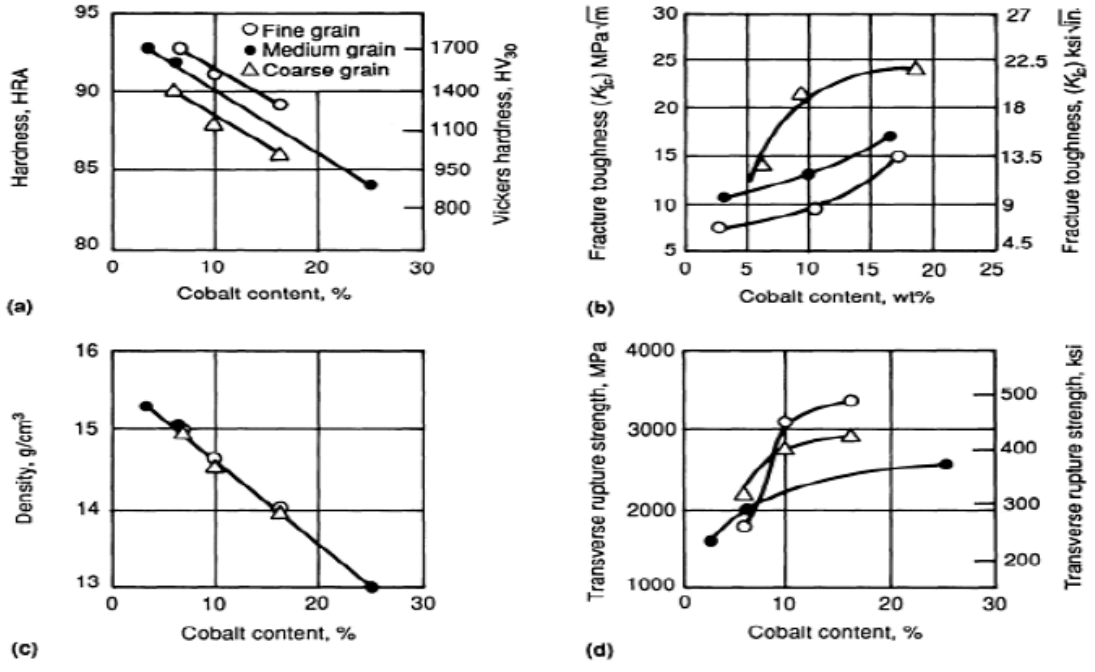


Figure 2. 3: Illustration of the effect of cobalt content on properties of cemented carbides [1].

2.1.4 Application of cemented carbides

The use of WC-Co materials is in applications where they must be able to withstand deflection, deformation, high wear rates, impact and corrosive wear. The durability of these hardmetals depends on the quality and properties achieved during the manufacturing process [5, 15, 18]. Widespread applications of these materials include metal cutting, wear parts, military components and mining tools (i.e. rock drilling) [1**,** 19]. Figure 2.4 illustrates the different fields of application and the percent distribution in various engineering sectors of cemented carbides [4].

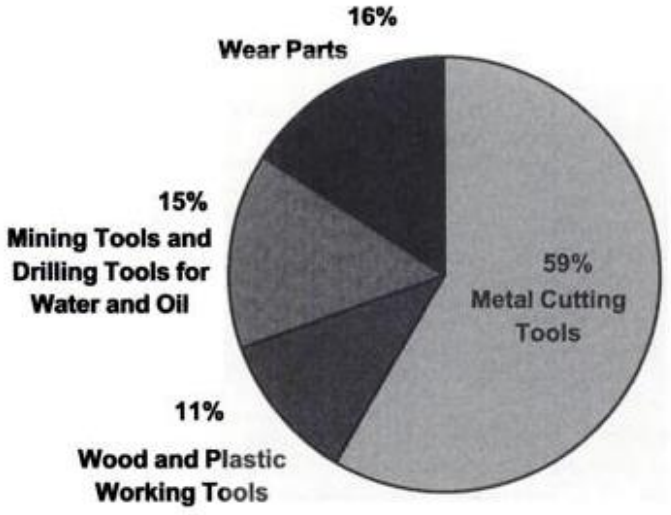


Figure 2. 4: Field of application of cemented carbides and their percent distribution in engineering sector [4].

The main advantages of using WC-Co hardmetals include [20]:

- Excellent wear resistance,
- Greater hardness than high speed steel, and
- Increased productivity due to the ability to withstand high speeds and high feed rates.

The focus in this study is the application of WC-Co hardmetals in the mining environment, specifically drilling operations. According to Upadhyaya [5], there are

three types of drilling methods which are used and each generates different wear mechanism.

a. Percussive drilling

This method is said to be relatively effective in the drilling of hard rocks. In this application the hardmetal wedge inserts are allowed to impact the rocks at least 2000-3000 times/min. Abrasive wear plays an important role in the wear of the inserts used, but the major damage is caused by micro-spalling and thermal cracking [5].

b. Rotary drilling

Rotary drilling resembles a machining tool wherein the drilling is done by the drag bit. The cutting is done by the hardmetal inserts which are mounted onto the cylinder. This method in normally used for tunnel boring and excavation, but not for drilling hard rocks, due to excessive wear that occurs on the material [5].

c. Percussive-Rotary drilling

This type of drilling is done by roller bits with small hardmetal inserts mounted onto them. The process is such that the inserts are pressed against the rock under a certain load. The rollers turn by friction as the whole bit turns, thereby removing some material by crushing. The formation of cracks at the contact area facilitates the rock removal by cutting and sliding in the second cycle [5]. Figure 2.5 shows the WC-Co hardmetal buttons (inserts) mounted on the drill bit [4].

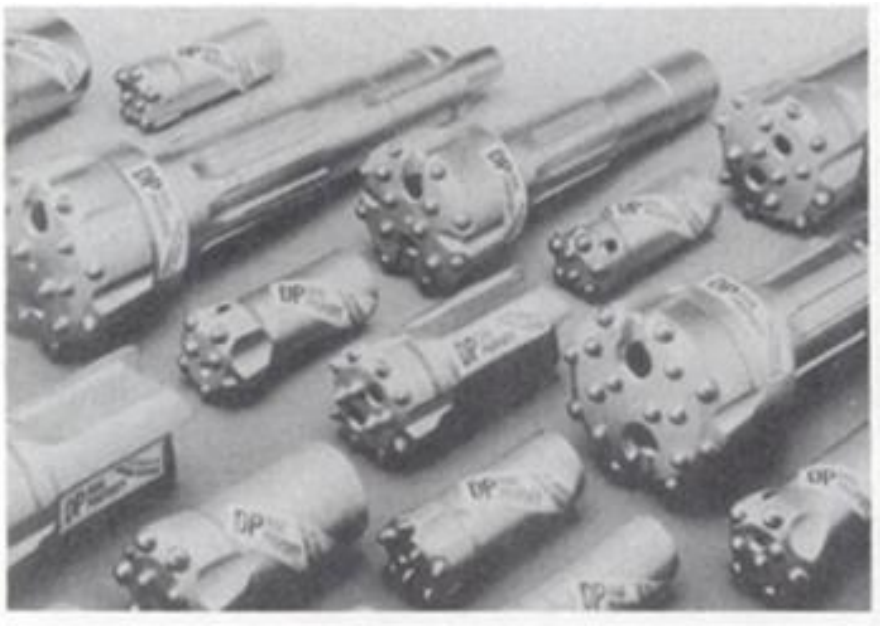


Figure 2. 5: Modern button bit tools for drilling purposes [4].

2.1.5 Properties of WC-Co alloy

a. Density

Density is a measure of mass per unit volume of material, usually measured in $g.cm^{-3}$. In hardmetals density is very sensitive to composition but when the composition is fixed, density varies with the level of porosity [4]. The density of a WC-10 wt. %Co alloy is approximately 14.5 $g.cm^{-3}$ [17]. The composition of the constituents can be used to determine the theoretical density but this method does not account for the presence of porosity produced during manufacturing [1]. The preferred method of measuring density is the Archimedes principle [21]. This principle specifies that the volume of a solid completely immersed in a liquid is equal to the volume of the liquid which it displaces. An increase in binder content decreases the density of hardmetals [1]

b. Hardness

Hardness is a measure of resistance to plastic deformation or scratching. It is an important property in the application of hardmetals [5]. The balance between hardness and strength of hardmetals can be achieved by adjusting the binder content and WC grain size. Generally, the higher the Co content and the coarser the WC grain size, the lower the hardness **[**15**,** 22-23]. For a constant composition, the grain size and porosity

have a major effect on the hardness of cemented carbides [5]. According to Cha *et al* [24], the hardness of WC-10 wt. % Co cemented carbides increased with decreasing WC grain size following a Hall-Petch-type relationship given by Eq.1.

$$H_{WC} = a + bd^{\left(-\frac{1}{2}\right)}\left(\frac{Kg}{mm^2}\right) \qquad \text{(Eq. 1)}$$

Where:

- H_{wc} is the hardness of the material in $Kg.mm^{-2}$
- a and b are constants
- d is the grain size in mm

In cemented carbides there are several methods used to determine hardness, namely, the Vickers diamond pyramid indentation test (HV) or the A Scale Rockwell cone indentation test (HRA).

c. Fracture toughness

Fracture toughness is a measure of the resistance of a material to crack initiation and propagation [25]. This property is important since it provides information about the suitability of the material in specific applications where stress conditions are defined [5]. Fracture toughness has been found to increase with an increase in Co content and WC grain size [1]. For WC-Co hardmetals, the fracture toughness is typically determined using the Palmqvist method which involves measurement of the crack lengths which emanate from the corners of a Vickers hardness indentation [5**,** 26-27]. A study conducted by Exner [27] showed that the crack length generated by the indentation load depends on the sample preparation (grinding and polishing). The main findings were [27]:

- Coarse grinding reduces tensile thermal stresses in the Co phase thereby reducing crack lengths, due to the increase in damage and deformation of the surface by mechanical action.
- Grinding of cemented carbides should be done using diamond disks rather than silicon carbide disks.

- Polishing increases the crack length due to the removal of the deformed layer generated during grinding.

It has also been found that the Palmqvist crack length in cemented carbides has a linear relationship with the applied indentation load and changes are due to sample preparation methods [27-28]. Figure 2.6 shows, the load and crack length relationship as a function of sample surface preparation. The figure illustrates that the longer crack length is influenced by the polishing process whereas coarse grinding reduces the crack length which is as a result of how both processes affect the final surface condition.

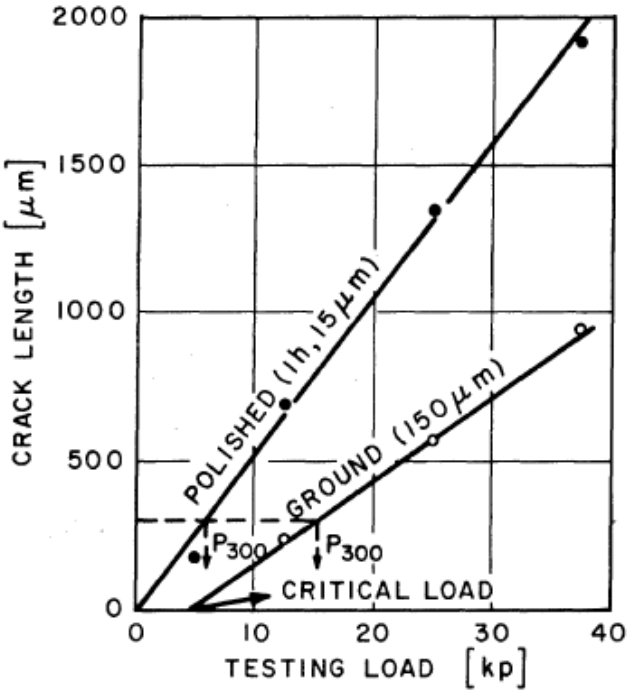


Figure 2. 6: Load and crack length relationship as a function of material surface preparation [27].

There are several equations that may be used to calculate the fracture toughness using the Palmqvist crack lengths, including the Shetty indicated in Eq. 2 [29].

$$K_{IC} = 0.0889\left(\frac{H_V P}{\sum l}\right)^{\frac{1}{2}} \qquad \text{(Eq. 2)}$$

Where;

- K_{IC} is the fracture toughness in MPa.m$^{1/2}$

- H_V is hardness of the material in MPa
- P is the load in N
- *l* is the crack length that emanate from each indentation corner in m

2.2 Wear

Wear is removal of material from solid surfaces as a result of mechanical action [8, 30]. Wear is not an intrinsic material property as it is dependent on the operating conditions of the engineering system. Even though individual wear mechanisms can be identified for a specific application, wear is not a simple process because transitions between two or more types of wear mechanisms can occur, e.g. in an adhesive wear situation the surface can work-harden and the wear debris may cause abrasion of the surfaces [31]. According to Glaeser *et al* [8], an understanding of the operating variables and the wear behaviour of the material is important when trying to solve wear problems. There are different types of wear including sliding, abrasion, erosion and fretting.

Sliding wear occurs when two surfaces slide against each other in relative motion [1**,** 32]. Abrasive wear occurs when the material is removed from the surface when in contact with hard particles [1**,** 25]. Fretting wear occurs when there is a small oscillating movement between two surfaces [30]. Erosion wear involves the removal of the surface material by high speed impact of hard particles [30]. Each wear type is unique and is influenced by the materials in contact, operational and environmental factors [5]. In the current study the focus was on reciprocating sliding wear.

2.2.1 Reciprocating sliding wear

Reciprocating wear is a loss of surface material as a result of the linear back and forth sliding motion between interacting bodies [1**,** 33]. Reciprocating wear is a form of sliding wear which can occur under lubricated or dry conditions [33]. There are three material removal mechanisms associated with sliding wear namely, scuffing, scoring and galling. Scuffing is localised surface damage associated with solid state welding between sliding surfaces [32]. Scoring implies scratching by an abrasive particle but sometimes used as a synonym for scuffing [32]. Galling is a more severe form of scuffing due to local welding, and it is associated with gross surface damage [32].

Several techniques have been developed to measure sliding wear rates including block-on-ring (ASTM G77), pin-on-disk (ASTM G99), sphere-on-disk (DIN 50324), rotating pin-on-flat (ASTM G98) and reciprocating sliding wear ASTM G133 [32].

In this type of wear, friction plays an important role on the wear response of the materials. According to Hutchings [32] continuous measurement of friction during a wear test will not only provide a numerical value of the friction coefficient (μ) but will also allow any changes in the sliding behaviour to be monitored (e.g. rise and fall of the friction coefficient or changes from smooth to irregular friction patterns).

Wear processes are driven by the dissipation of frictional energy and this can lead to formation of oxides on the surface, phase transformations of the microstructure, and surface damage induced by thermal stresses [30]. Frictional energy is normally formed by a combination of the following factors [30**,** 32];

- Applied load
- Sliding speed
- Material property
- Contact area.

All these factors affect the dissipation of energy from the material. A study was conducted and a relationship between normal applied load and sliding velocity was obtained for unlubricated sliding of steel on steel in a pin-on-disk configuration and generated the wear regime map shown in Fig. 2.7 [32]. This wear regime map indicates the role of the operating conditions on the wear mechanisms. Wear rates and the wear mechanism changes, as the sliding velocity and normal load changes. Increasing the sliding velocity and normal load led to an increase in interfacial temperatures which could result in melting of the material surface [32].

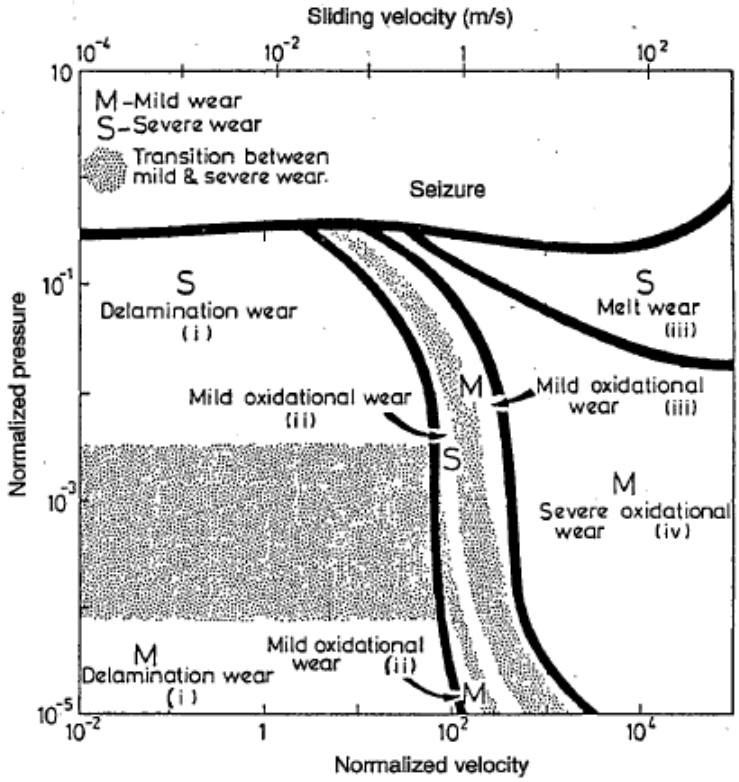


Figure 2. 7: Wear regime map for unlubricated sliding of steel on steel in the pin on disc [32].

2.2.2 Wear of WC-Co hardmetals

Superior abrasive wear resistance is one of the major properties that make cemented carbides the best material of choice in most industrial applications. The hard WC particles contribute to the wear resistance while the Co binder provides ductility to the WC-Co hardmetals [1]. Numerous studies have been conducted to understand the wear behaviour of WC-Co hardmetals. Material volume loss can be measured and then used to determine the wear rates, while the wear scars may be examined using microscopy to determine the wear mechanisms. The wear resistance of WC-Co hardmetals has been found to be influenced by the composition and microstructure [1**,** 15**,** 22].

Work done by Qiao *et al* [31] on abrasive and un-lubricated sliding wear of WC-Co hardmetals using a ball-on-disk tribo-meter indicated that the wear resistance is limited by the material hardness. A study done on alloys having 5-50 wt% Co and a WC grain size range of 0.6 - 5µm found that wear resistance increased in a parabolic manner until a critical value of hardness was reached, above which the relationship was exponential

[34]. The critical hardness was also found to decrease with an increase in the WC grain size [34]. Figure 2.8 illustrates this wear resistance – hardness relationship.

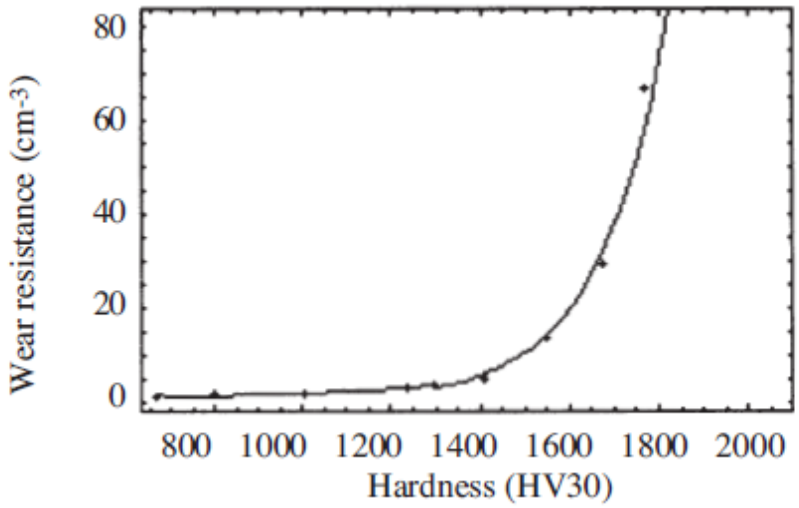


Figure 2. 8: Wear resistance vs. hardness of WC-Co alloys [34].

According to O' Quigley *et al* [18], hardness may be used as an indirect measure of abrasion wear resistance only at low hardness values, where wear is primarily due to plastic deformation. The authors found that at higher hardness values, micro-fracture plays a role in the wear process and then abrasion resistance depends on the WC grain size, Co content and operational parameters (load, speed at which surfaces are moving, and size and nature of the abrasive material). In a study done by Juhani *et al* [12], the wear behaviour of hardmetals in dry environment was found to be different when compared to the wear behaviour of hardmetals in wet environments. In this research two body abrasion tests were conducted on WC-Co alloys with a Co range of 0 -30 wt. % using a block-on-ring test method. The volume loss of the materials was found to increase linearly in dry conditions with an increase in the Co binder fraction, whereas in wet conditions the volume loss increased linearly up to 15 wt. % Co, and then decreased as shown in Figure 2.9 [12].

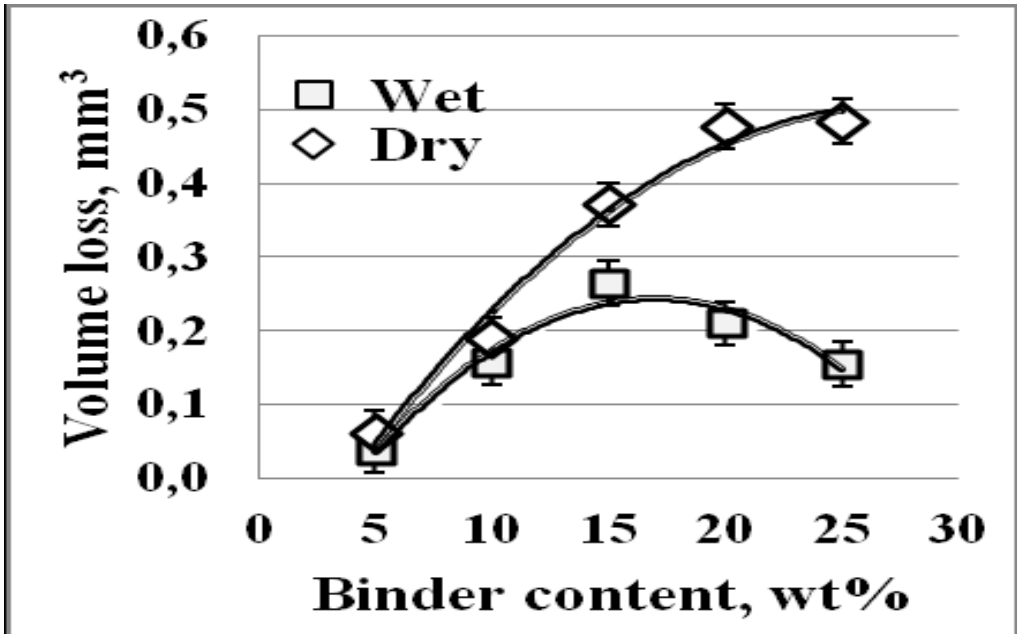


Figure 2. 9: The volume loss vs. binder content of WC-Co hardmetals in dry and wet wear conditions [12].

Shipway *et al* [10] indicated that the wear mechanism of WC-Co hardmetals also depend on the type and hardness of the abrasive/counter-body material used. In this study, three types of abrasive particle slurries of different hardness were used, namely diamond, silicon carbide and alumina. Silicon carbide and alumina caused wear by the removal of the binder phase followed by pulling out of the exposed WC grains, and it was found that the wear rates increased with an increase in the binder phase fraction. Diamond did not show any pull-out of the WC grains, and no clear distinction of the WC phase could be made on the wear scars, which was said to be an indication of the surface wearing out at a constant rate [10]. Figure 2.10 is an example of general sliding wear on WC-Co hardmetals with smearing of Co and cracking of WC grains [35].

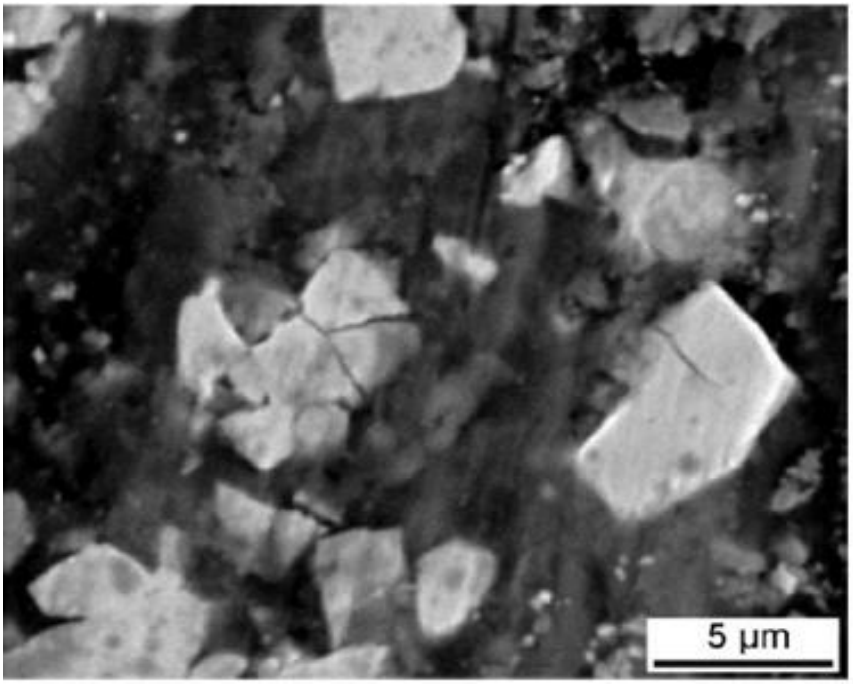


Figure 2. 10: A SEM micrograph showing wear mechanism of WC-Co hardmetals [35].

Wear resistance of hardmetals can also be enhanced by the addition of grain growth inhibitors such as Cr_3C_2 and VC which are added during the liquid phase sintering process [11]. According to the study done by Bonny *et al* [11**]**, on the impact of Cr_3C_2/VC addition on the dry sliding friction and wear response of WC-10 wt. % Co cemented carbides using a pin-on-flat test, the coefficient of static and dynamic friction was found to be smaller on the hardmetals where grain growth inhibitors were added when compared to the standard WC-10 wt. % Co hardmetals. The difference in coefficient of friction was attributed to adhesion, due to chemical composition, grain size and distribution of the binder. This addition of the grain growth inhibitors caused an increase in hardness due to grain refinement thereby enhancing wear performance. The sliding wear mechanisms identified were [11]:

- Polishing of the WC grains,
- Surface binder removal by plastic deformation, and
- Fracture of the WC grains and debris formation.

A study done by Bonny *et al* [36] on the dry reciprocating sliding friction and wear response of WC-Ni cemented carbides under a load of 25 N, sliding velocity of 0.3 m/s, stroke length of 15 mm and sliding distance of 10 km, emphasised the increase in the coefficient of friction as a function of the binder content. This was due to the adhesion

by the binder which increased the tangential force that restricted the sliding motion [36].

2.3 Corrosion of WC-Co alloys

2.3.1 Corrosion and corrosive wear

Corrosion is the deterioration of a material as a result of a chemical reaction with its environment. Corrosion is said to shorten the predicted design life of the material, which is the time span after when replacement is anticipated [37]. This phenomenon cannot be defined without reference to the environment because it has been found that every environment is corrosive to some degree however, corrosion will only occur once a corrosion cell is formed [37-38]. Corrosive wear is the synergistic action between corrosion and wear mechanisms when a material experiences wear in a corrosive environment.

Corrosion measurements are normally conducted using a potentiostat, which is an instrument that maintains the desired potential between the working and reference electrodes, while passing current between the working and counter electrodes. In this set-up the current applied can be controlled and the potential of the working electrode can be measured with respect to the reference electrode [39].

2.3.2 Corrosion of cobalt

The standard potential of cobalt is given by the electrochemical reaction in Eq. 3 [39].

$$Co^{2+} + 2e \longrightarrow Co \ldots\ldots\ldots\ldots\ldots\ldots E^{o} = -0.277V \qquad \text{(Eq.3)}$$

Cobalt is rapidly attacked by oxidizing acids and salts (i.e. HNO_3 and $FeCl_3$) but resistant to alkalis [39]. Cobalt can be cathodically protected from acids or neutral solutions by polarizing to active potentials of –0.5 V as illustrated in Figure 2.11. This figure shows the theoretical potential vs. pH domains of corrosion, immunity, and passivation of cobalt in aqueous solution at 25 ° C [39].

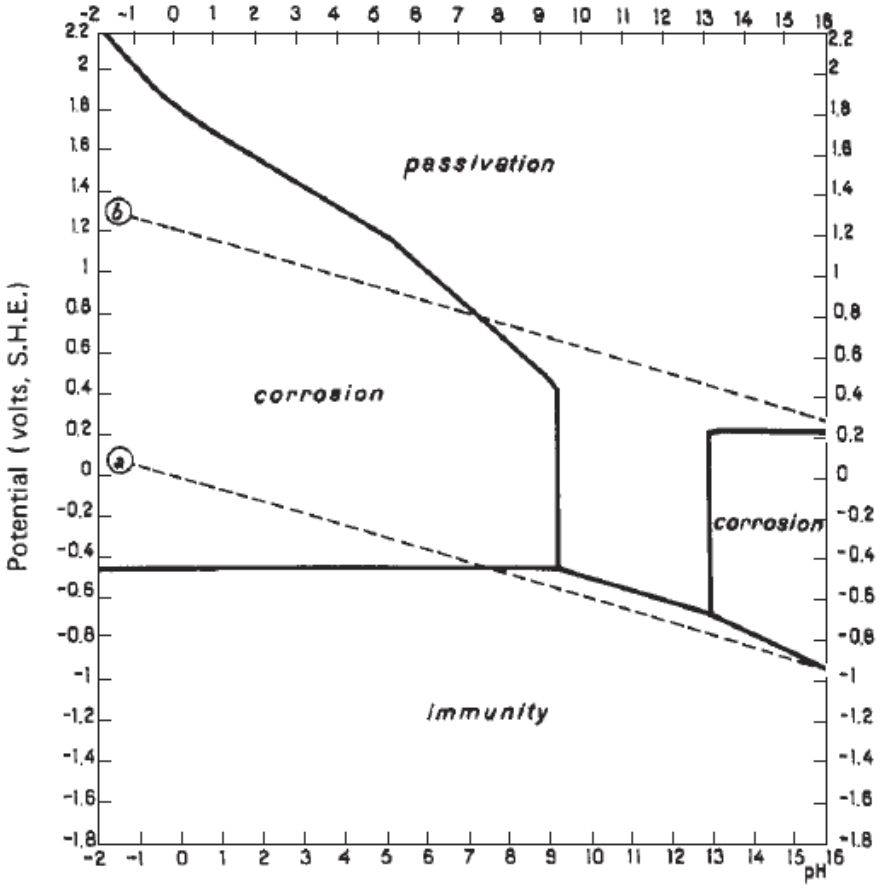


Figure 2. 11: The pH and potential relationship for Co in aqueous solution at 25°C [39].

2.3.3 Corrosion and corrosive wear of WC-Co hardmetals

Corrosion of cemented carbides is based on the corrosion behaviour of the two constituents, i.e. Co and WC. Co has a poor corrosion and oxidation resistance whereas WC has excellent corrosion resistance and good oxidation [1**,** 19]. In applications where corrosion, wear resistance and stiffness are equal requirements, cemented carbides become the material of choice [1]. Studies have shown that it is difficult to justify the use of WC-Co in an environment where corrosion is the only factor, but in the case where abrasion is also present then the correct grade of WC-Co should be considered [1**,**15]. Corrosion resistance of cemented carbides is generally limited to the susceptibility of Co to chemical attack, even though there are chemicals that are known to attack WC [5**,** 19].

According to Shipway *et al* [14] when WC-Co hardmetals are exposed to wear and corrosion simultaneously, corrosion has a significant influence on wear due to surface depletion of the binder phase. The corrosion of WC-Co is such that the Co binder

matrix is dissolved in the electrolyte, leaving the WC grains exposed, which are then easily eroded away by mechanical action due to little support [1**,** 14**,** 15**,** 19]. The result is a pitted surface which is dull in appearance. Severe pits act as stress raisers, thereby reducing the strength of the cemented carbides [15]. It has been found that for straight WC-Co hardmetals there is a direct relationship between cobalt content and corrosion [19]. Shipway *et al* [14] found that in neutral environments, the corrosion rate of the binder is relatively low, but a decrease in pH resulted in significant removal of the binder phase.

The corrosion resistance of WC-Co hardmetals can also be improved by the addition of alloying elements such as Cr [1]. Work done by Machio *et al* [40] on the effect of VC content on WC- 10 wt.% Co in NaCl and synthetic mine water showed that corrosion of the WC-Co is solution dependent. A high VC content improved the corrosion resistance of the WC-Co alloy in synthetic mine water substantially. Figure 2.12 illustrates the corrosion resistance of various grades of hardmetals as a function of pH.

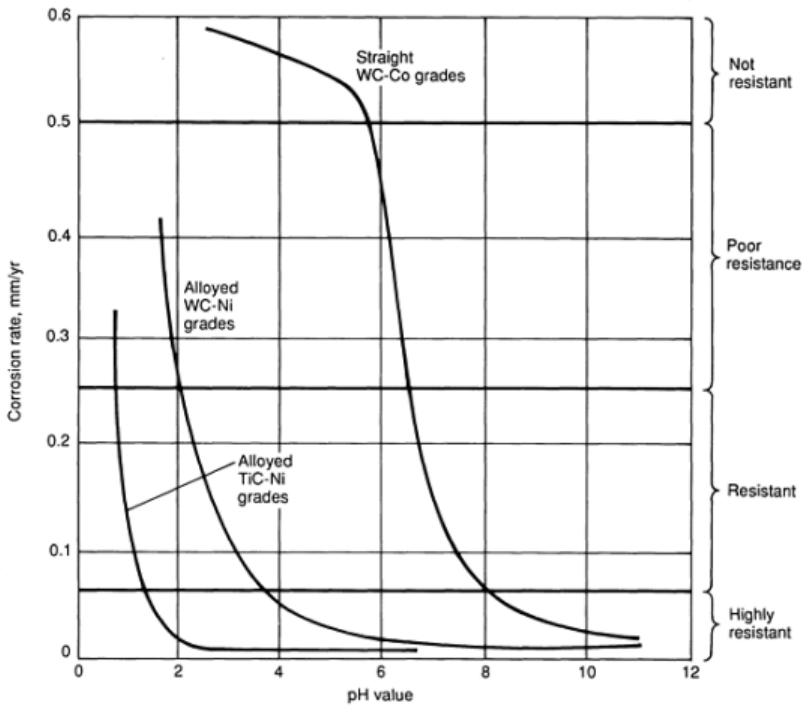


Figure 2. 12: Corrosion resistance of cemented carbides as a function of pH [1].

Chapter 3

Experimental Procedure

This chapter gives a description of the experimental procedure followed in determining the material properties, corrosion, and reciprocating wear response of cemented carbide buttons in synthetic mine water and distilled water, against two industrial steel substrates.

3.1 Material characterization

3.1.1 Materials

The buttons studied were straight grade cemented carbides of a bullet shape. These buttons are normally used in percussive rotary drilling [5, 4, 7]. Figure 3.1 indicates the physical appearance of the buttons whereas Table 3.1 gives composition and button dimensions.



Figure 3. 1: Physical appearance of the cemented carbide buttons.

Table 3. 1: WC-6 wt.% Co button composition and dimensions.

Composition		**Dimensions**	
Wt.% WC	Wt.% Co	Height (mm)	Diameter (mm)
96	6	13.3	9.2

The counterfaces used in the wear tests were commercial grades of mild steel and 3Cr12 stainless steel. These materials were supplied as rectangular bars with dimensions of 70 x 12 x 10 mm, and their physical appearance is given by Figure 3.2 in which (a) is 3CR12 stainless steel and (b) is mild steel. Table 3.2 gives the chemical composition of the steel counterfaces.

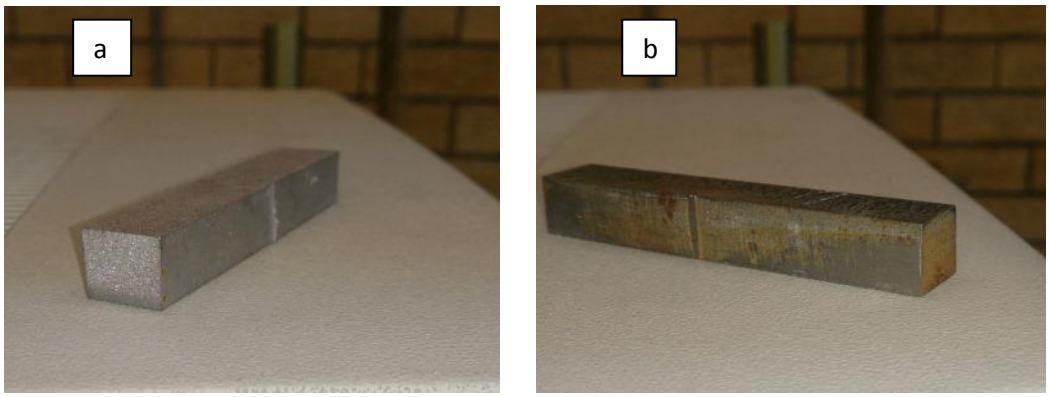


Figure 3. 2: Physical appearance of the steel counterfaces.

Table 3. 2: Chemical composition of steel counterfaces

Element	3Cr12 stainless steel	Mild steel
% C	0.012	0.0183
%Mn	0.893	0.772
%Si	0.744	0.223
%Cr	11.69	0.07
%Ni	0.744	0.112
%P	0.021	0.014
%Mo	0.066	0.001
% Cu	0.1	0.026
%S	0.0005	0.009
%Ti	0.13	0
%V	0.068	0.022

3.1.2 Sample preparation

For microstructural characterization, some of the tungsten carbide buttons were cut transversally and mounted in Polyfast resin. Grinding and polishing was done using an automated Saphir 520 machine to prepare the samples to a 1 µm surface finish. Water was used to remove debris and to prevent heat accumulation during grinding. Between

polishing stages the samples were rinsed using ethanol. Table 3.3 indicates the procedure followed.

Table 3. 3: Grinding and polishing routine for WC-6 wt.% Co buttons.

GRINDING					
Step	Time (min)	Pressure (N)	Speed (rpm)	Grinding disk	Abrasive aid and/or Coolant
1	4	80	300	Piano 120	Water
2	3	80	300	Piano 220	Water
3	3	80	300	Piano 1200	Water
POLISHING					
4	4	100	150	9 micron Nap	9µm premium diamond suspension and diamond extender
5	4	100	150	6 micron Nap	6µm premium diamond suspension and diamond extender
6	10	100	150	1 micron Nap	1µm premium diamond suspension and diamond extender

Cross sections from each steel counterface were sectioned and mounted in Polyfast resin. Grinding and polishing was done to prepare the samples for further testing. Grinding with grit sizes ranging from coarsest to finest [320 µm;1200 µm] was done using water as a coolant. Samples were polished to a surface finish of 1µm.

3.1.3 Hardness

Polished samples were used for hardness testing. A Future Tech FV-800 Vickers hardness tester was used to determine the hardness of the cemented carbide and steel samples. The machine is automated; after each indentation, one measures the diagonals at 20X magnification, and the machine computes the hardness measurement. A load of 30 kg was used for both the buttons and steel counterfaces. Two cemented carbides samples were used for hardness with 5 indentations per sample whereas one sample was used for each steel counterface with 5 indentations.

3.1.4 Fracture toughness

Determination of fracture toughness was done by measuring the length of the cracks which emanated from the edge of the Vickers hardness indentation as a function of applied load. This is the Palmqvist technique for determining fracture toughness in hardmetals [5**,** 27]. The fracture toughness values were calculated using the Shetty formula [29], given by Eg. 4.

$$K_{IC} = 0.0889\sqrt{HV\left(\frac{P}{4l}\right)} \qquad \text{(Eq.4)}$$

Where;

- K_{IC} is the fracture toughness MPa.$m^{1/2}$
- HV is the hardness of the material in MPa
- P is the indenting load in N
- *l* is the crack length that emanate from each indentation corner m

3.1.5 Density and porosity

Density is the proportion of mass to volume in a material. In this study the density of the WC-Co hardmetals was determined using the Archimedes submersion principle in a Sartorius machine whereas the density of the counterfaces was determined by dividing the mass by the volume. Dry mass, suspended mass and wet mass of the sample were measured in this machine. Density computation was done using Eq. 5 [21].

$$\rho_S = \rho_L \frac{m_{Dry}}{m_{Wet-mass} - m_{Susp}} \qquad \text{(Eq.5)}$$

Where ρ_S = Density of sample (g/cm^3)

ρ_L = Density of liquid used (g/cm^3)

M_{Dry} = Dry mass of sample (g)

$m_{wet\text{-}mass}$ = Wet mass of sample (g)

m_{Susp} = Suspended mass of sample (g)

The porosity present in the sample was calculated using Eq. 6 [21].

$$\%\,porosity = \frac{m_{wet-mass} - m_{Dry}}{m_{Wet-mass} - m_{Susp}} \times 100\% \qquad \text{(Eq.6)}$$

3.2.2 Microstructure

A LEICA CTR 600 light microscope was used at low magnification for evaluation of the microstructures. A CARL ZEISS field emission scanning electrom miscroscope (SEM) was used for high resolution images in order to characterize the microstructure. EDS was used for elemental analysis.

a. 3CR12 Stainless steel

The 3CR12 stainless steel samples were etched using a solution of 50 mL distilled water, 50 mL nitric acid (HNO_3) and 50 mL hydrochloric acid (HCl). The sample was immersed in the etchant for few seconds, rinsed in running water, followed by ethanol and then dried.

b. Mild steel

To reveal the microstructure of mild steel, 3% Nital (3% HNO_3 and 97% ethanol) was used for etching. The sample was immersed in etchant for 15 seconds. After etching, the sample was rinsed in running water followed by ethanol and then dried.

c. Cemented carbide buttons

To reveal the microstructure of cemented carbide buttons, the polished cemented carbide button samples were etched using Murakami‘s reagent and its composition is given in Table 3.4. Etching in the solution was done for about 90 seconds, followed by rinsing with water, then alcohol and finally dried.

Table 3. 4: Composition of Murakami’s reagent [26]

Compound	**Composition**
Distilled water	100 ml
Potassium hexacyanoferrate - $K_3Fe(CN)_8$	10 g
Sodium Hydroxide - NaOH	10 g

3.1.7 Phase analysis

X-ray diffraction (XRD) was conducted using cobalt anode with X-ray generator settings of 30 kV and 10 mA on a Bruker D2 Phaser diffractometer coupled with a Lynx Eye detector for identification of the phases present in the cemented carbide buttons and the two steel counterfaces. The measurements were made from 10 º to 90 º at a scan rate of 0.026 °per second.

3.2 Reciprocating sliding wear tests

3.2.1 Test description

Reciprocating wear tests were conducted using the wear test machine shown in Figure 3.3. The configuration of the test was pin on flat which is according to ASTM G133 [30]. In this set-up the stationary button is pressed against the flat steel counterface which is moved in a reciprocating motion. The reciprocating motion is generated by the crank arms which are connected to a drive motor through the cam belt. The flat counterface is fixed in the reciprocating stage. Several test parameters can be varied in this machine, including frequency of oscillation, applied load, and the sliding distance. The parts description is as follows;

A = Button sample holder

B = Load on the lever

C = Reciprocating stage (where flat steel sample is placed)

D = Drive crank

E = Drive motor

F = Lubrication container equipped with pump

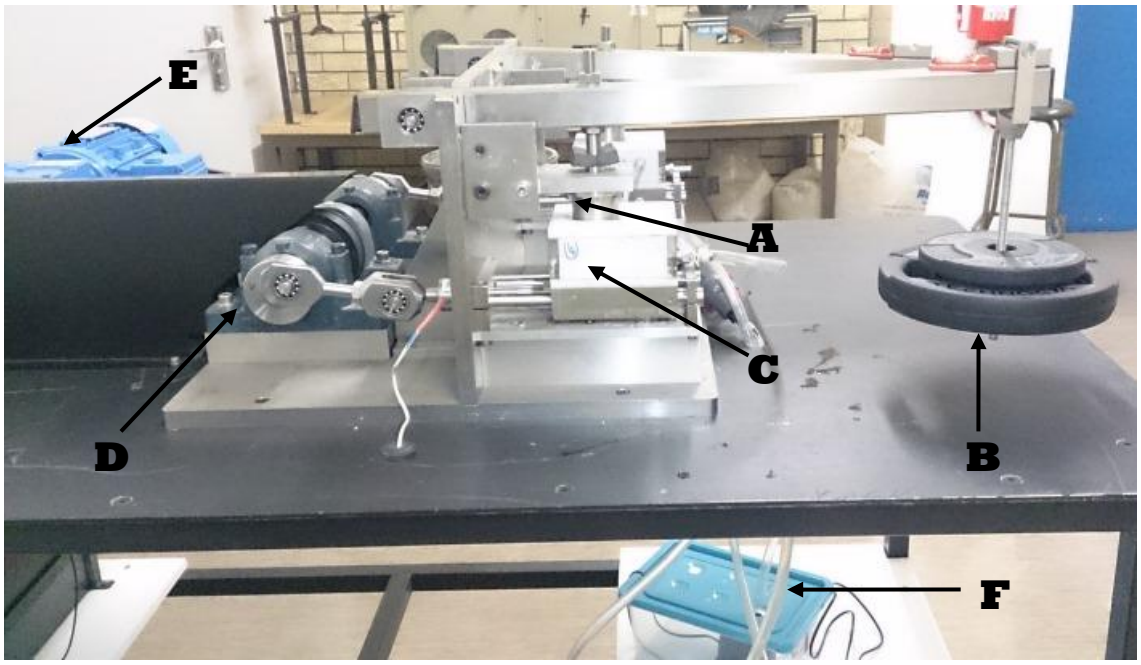


Figure 3. 3: The reciprocating wear testing machine.

The load used was 213 N generated by applying 61.3 N (6.25 Kg) on the lever as indicated by point B in Figure 3.3. The load was chosen based on previous studies where tests on drill bits were done using loads of 100 N- 200N [9]. The test duration was 60 min which corresponds to 109 m sliding distance. During testing, the mass loss was recorded at 10 min intervals using. Before weighing the samples ultrasonic cleaning was done using ethanol in an Integral System ultrasonic machine. The reciprocating wear machine was operated at an input motor frequency of 20 Hz. Tests were conducted on both steel counterfaces in synthetic mine water and distilled water solution. The composition of synthetic mine water is given in Table 3.5 gives. The distilled water was used as a standard control against which the aggressiveness of the mine water solution could be assessed. A summary of the test parameters used are given in Table 3.6.

Table 3. 5: Composition of synthetic mine water [40].

Compound	Concentration (mg/l)
Magnesium Sulphate -$MgSO_4$	199
Sodium Sulphate - Na_2SO_4	1237
Sodium Chloride - NaCl	1380
Calcium Chloride - $CaCl_2$	1038

A summary of the test parameters used in the reciprocating wear machine in determining the wear behavior of the materials is given in Table 3.5.

Table 3. 6: A summary of wear test parameters.

Parameter	Value
Applied load (N)	213
Input motor frequency (Hz)	20
Test duration (min)	60
Stroke (mm)	52
Number of cycles	3072
Sliding distance (m)	319

3.2.2 Wear rate calculations

As mentioned in section 3.2.1, mass loss of the sample was recorded at 10 min intervals. The mass loss recorded together with the density of the material was used to calculate the volume loss of the material during sliding with an aid of Eq. 7,

$$V = \frac{m}{\rho} \qquad \text{(Eq.7)}$$

Where;

- V is the volume of the material in mm^3
- M is the mass of the material in g
- ρ is the density of the material in $g.mm^{-3}$

The wear rate coefficient (k) was calculated using Archard wear equation shown in Eq. 8 [32].

$$k = \frac{V}{s \times F_N} \qquad \text{(Eq.8)}$$

Where:

- V is the volume loss of the material in mm^3
- s is the sliding distance in m
- F_N is the normal applied load in N
- k is the wear rate coefficient $mm^3/N.m$

The material volume loss calculations of the cemented carbide buttons were determined according to Eq. 9 and Eq. 10. This volume loss calculation is based on the measurement of the size of the wear scar which is converted to wear volume [1]. Figure 3.4 gives an indication of the dimensions used in calculating worn volume. The reason for using different equations for measuring the volume loss of the cemented carbide buttons compared to the method used for the steel counterfaces was that the mass loss of the hardmetal was too small to be measured using the analytical weighing balance.

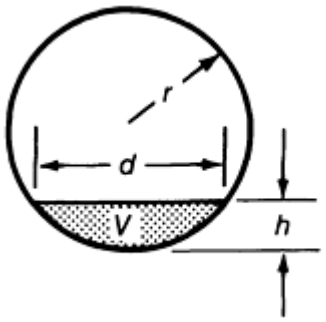


Figure 3. 4: Configuration for buttons' worn volume calculations [1].

$$V = \frac{\pi}{6} h\left(3\frac{d^2}{4} + h^2\right) = \frac{1}{3}\pi h^2(3r - h) \qquad \text{(Eq.9)}$$

$$but: h = r - \sqrt{r^2 - \frac{d^2}{4}} \qquad \text{(Eq.10)}$$

Where;

- d is the diameter of the wear scar in mm
- r is the radius of the ball/button in mm
- h is the worn height in mm
- *V* is the volume worn in mm^3

3.3 Corrosion tests

Standard potentio-dynamic corrosion tests were conducted in this project on both the cemented carbide buttons and the steel counterfaces using an Auto-lab 1 potentiostat. Synthetic mine water and distilled water were used as electrolytes. The aim of using distilled water was for reference purposes. The corrosion test were conducted in order to determine the behaviour of cemented carbide buttons in synthetic mine water and also determine if there was any synergistic effect with wear. The pH of both solutions was determined using a pH meter.

3.3.1 Sample preparation

The cemented carbide button, samples were cold mounted using resin and polished to a surface finish of 1 µm prior to testing. The mild steel and 3CR12 stainless steel samples were also cold mounted in resin and polished to a surface finish of 1200 µm. The samples were made electrically conductive by the attachment of a wire using an aluminium sticker.

3.3.2 Test Procedure

The corrosion tests were conducted using similar parameters obtained in a study done by Machio *et al* [40], except for the scan rate which was reduced to 0.5 mV/s. Table 3.7 gives the details of the parameters used. The working electrodes were cemented carbide buttons, mild steel and 3CR12 stainless steel, with platinum (Pt) and silver chloride (AgCl) were used as counter and reference electrodes respectively. The tests were repeated twice for repeatability purposes. The experimental set-up is illustrated in Figure 3.5.

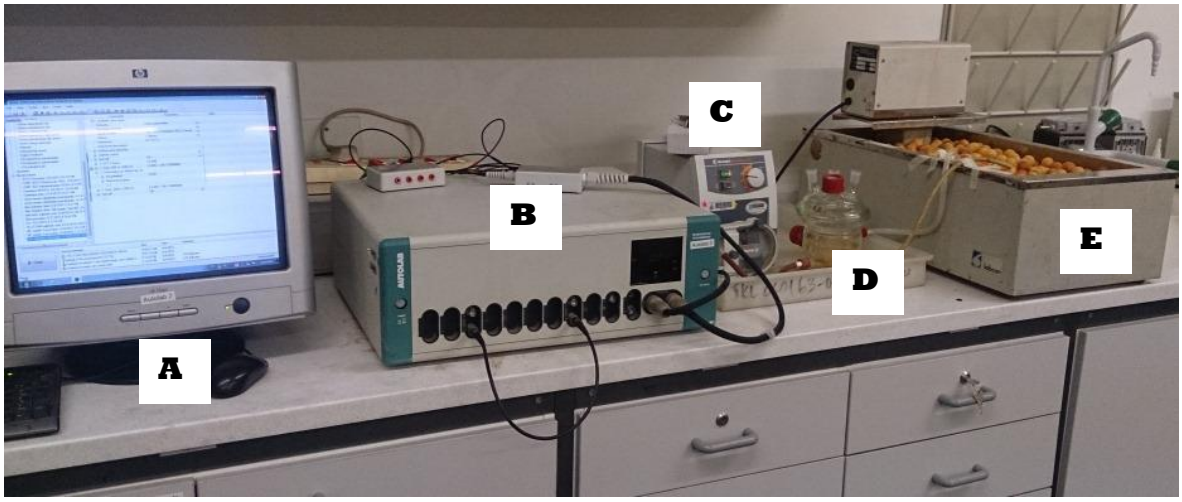


Figure 3. 5: Corrosion test set-up.

A = Computer screen

B = Scanner

C = Water pump

D = Corrosion cell

E = Temperature regulating bath

Table 3. 7: A summary of corrosion test parameters.

Parameter	Value
Scan potential (mV)	-600 to +1200
Scan rate (mV)	0.5
Temperature (°C)	25
Open Circuit Potential (hours)	2

The Tafel plots generated during the scanning on the Nova 1.10 Metrohm programme were used to calculate the corrosion rates. These calculations are done by extrapolation of the linear part of the anodic and cathodic Tafel slopes from the polarization scans. Once the scanning and the extrapolation on the Tafel plots was completed, the programme automatically calculates the corrosion parameters required namely corrosion potential (E_{corr}), corrosion current (I_{corr}), and corrosion rate (Corr-rate). Figure 3.6 illustrates the extrapolation process.

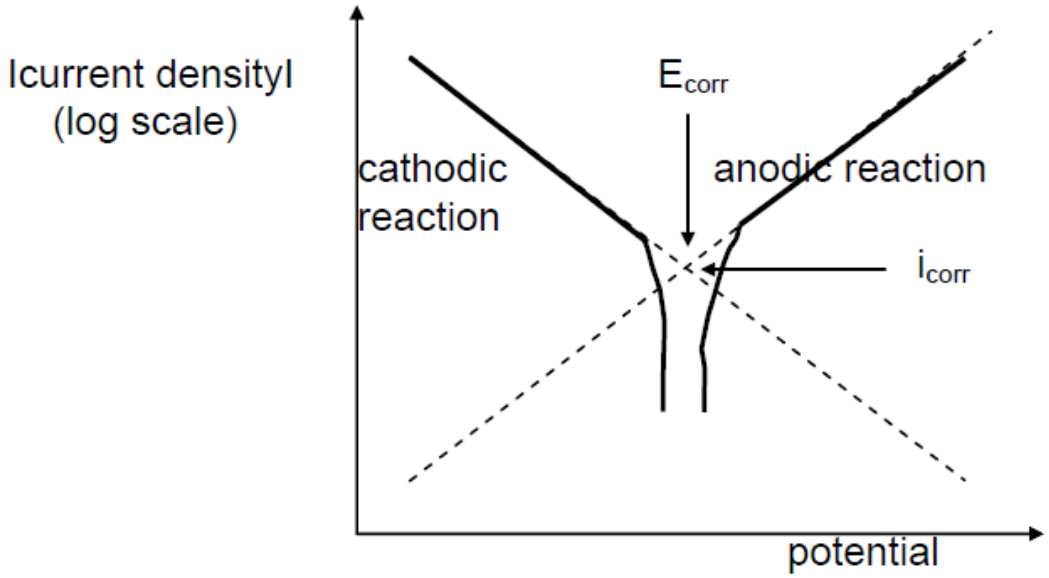


Figure 3. 6: Schematic showing the Tafel plots from which the values of I_{corr} and E_{corr} is determined [26].

3.4 Examination of wear scars

A Carl Zeiss field emission scanning electron microscope (FESEM) in backscattered and secondary mode was used for examination of the wear scars for identification of the wear mechanisms. Cross sections (on substrates) and planer surfaces of the wear scars were examined. INCA software was used to perform EDS for the elemental composition on the wear scars of the samples.

Chapter 4

Results

This chapter describes the results of the experimental work done on the cemented carbide buttons and steel counterfaces. This entails the physical, mechanical, microstructural, corrosion, as well as the reciprocating wear properties of the cemented materials.

4.1 Material characterisation

4.1.1 Microstructural analysis

Figure 4.1 shows the microstructure of the 3CR12 stainless steel sample. The microstructure consists of ferrite matrix and martensitic plates, aligned in one direction, which is an indication of rolling during the production process. This microstructure is in an as-received condition.

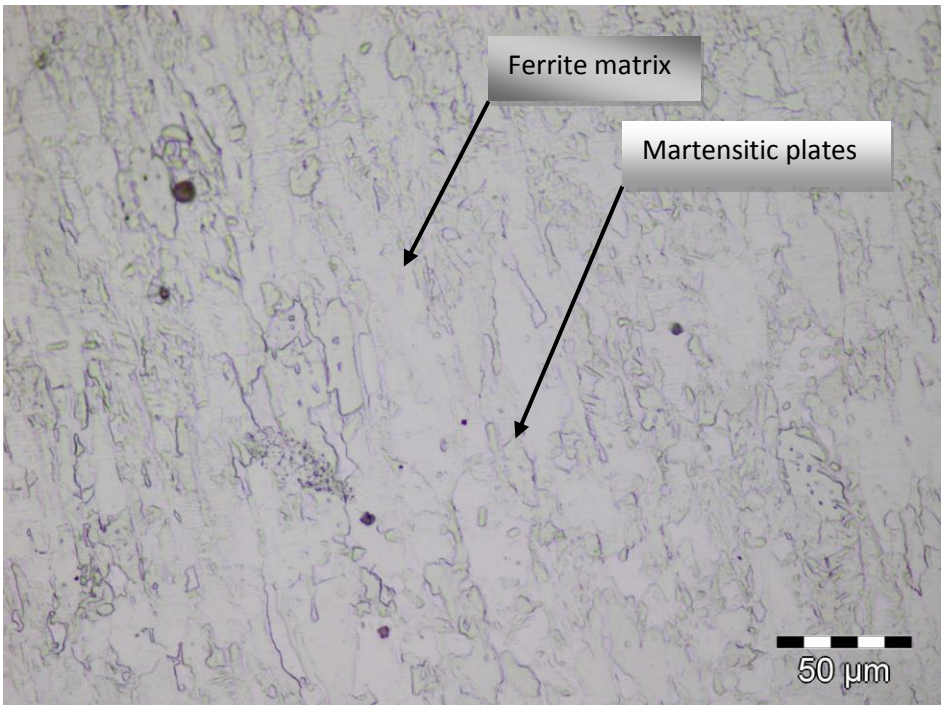


Figure 4. 1: Optical micrograph of the 3CR12 stainless steel sample at 50X magnification.

Figure 4.2 shows the microstructure of the mild steel sample. The image shows a typical carbon steel microstructure, consisting of ferrite (white constituent) and pearlite (dark constituent). The orientation of the grains is an indication that this steel was rolled during production.

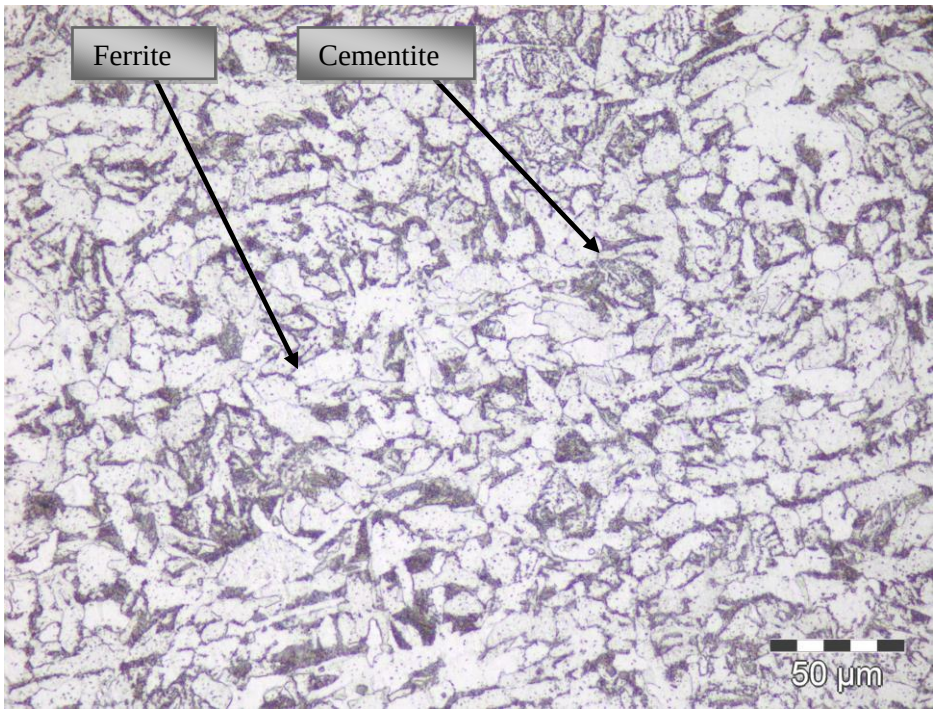


Figure 4. 2: Optical microstructure of the mild steel sample at 50X magnification.

Figure 4.3 shows an SEM microstructure of the WC-6 wt.% Co cemented carbide button. The microstructure consists of the typical angular tungsten carbide grains (grey), of various sizes and the cobalt (black) phase between the tungsten carbide grains. The apparent grain size of the WC-6 wt.% Co was estimated using ASTM B390-92 at a magnification of 1500X. The microstructure was found to be a mixture of coarse and fine WC grains, which according to ASTM B390-92, is Type 6-M with M denoting medium-sized grains and 6 indicating the cobalt content.

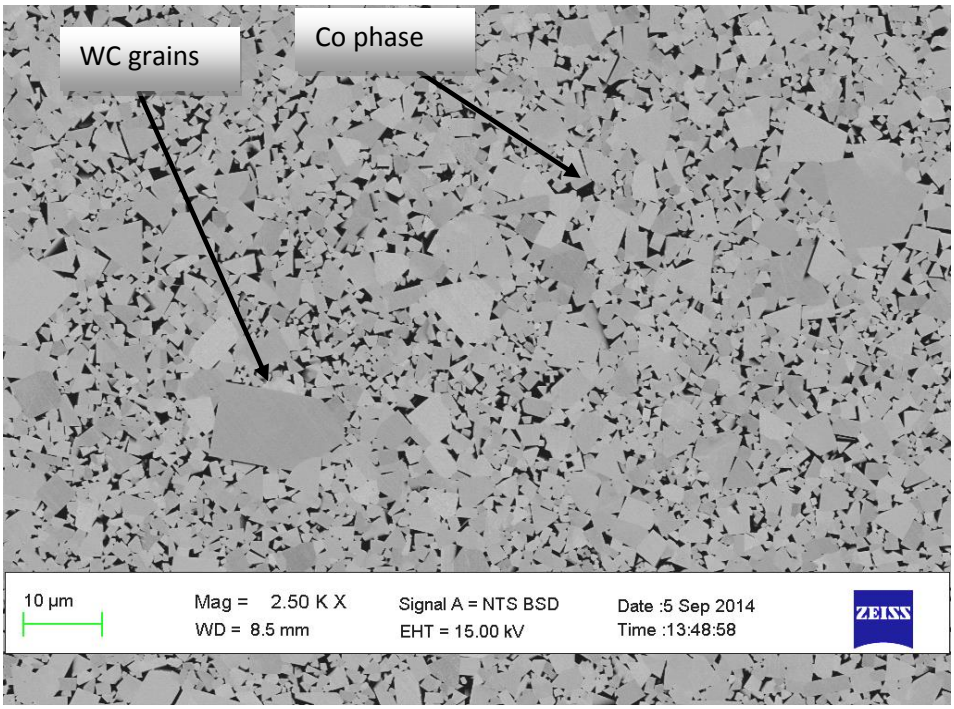


Figure 4. 3: An SEM microstructure of the WC- 6wt.% Co cemented carbide button at 2500 magnification.

4.1.2 Phase analysis

Figure 4.4 are the XRD pattern for mild steel in an as received condition. The pattern showed the presence of the typical mild steel elements, with no evidence of detrimental phases such as FeS which could reduce the mechanical properties.

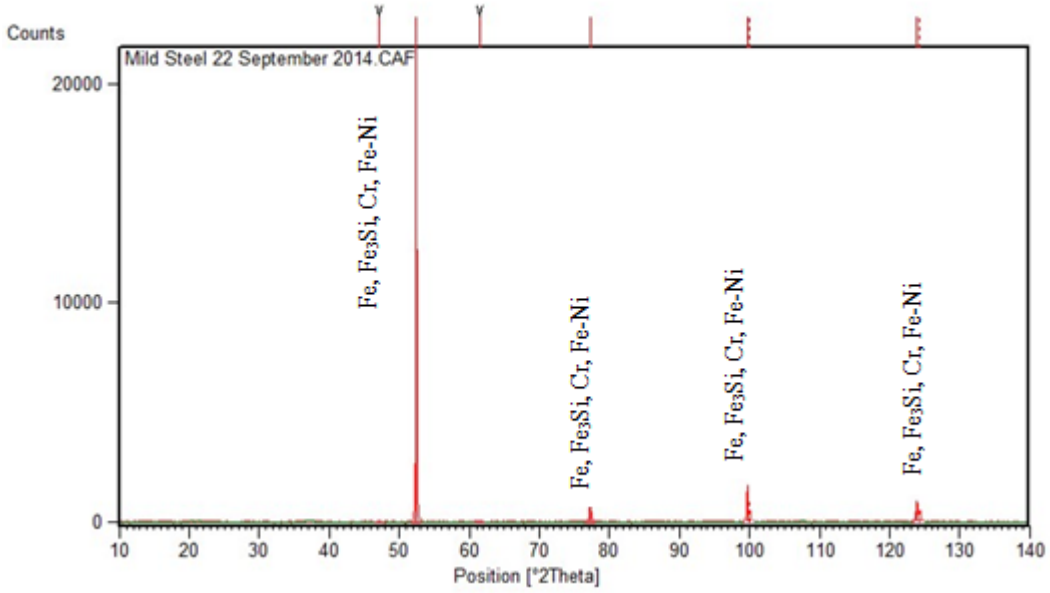


Figure 4. 4: XRD pattern for the mild steel in an as received condition.

Figure 4.5 is the XRD patterns for 3CR12 stainless steel in an as received condition. The pattern showed the presence of the typical 3CR12 stainless steel constituents, with no evidence of detrimental phases which could reduce the mechanical properties.

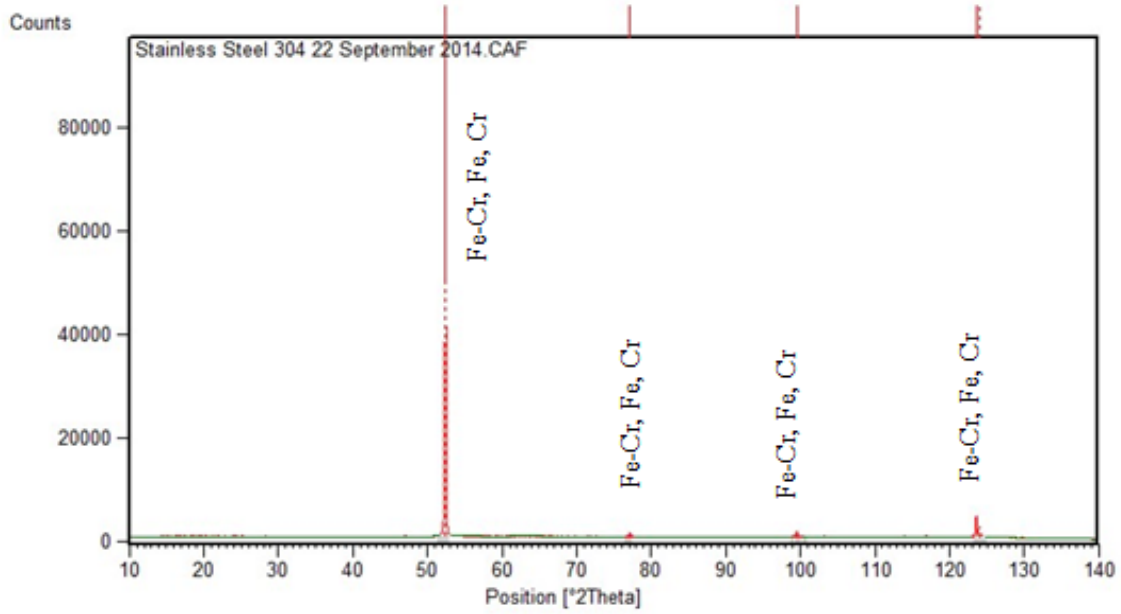
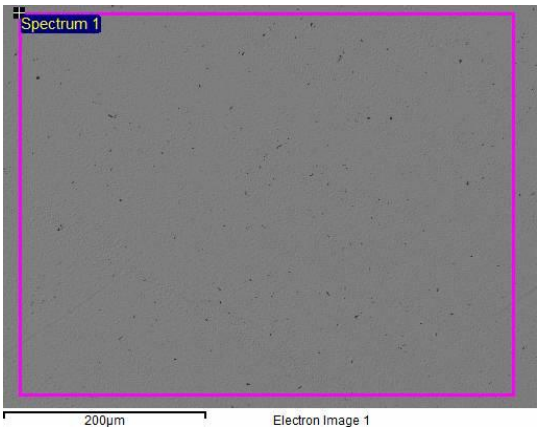
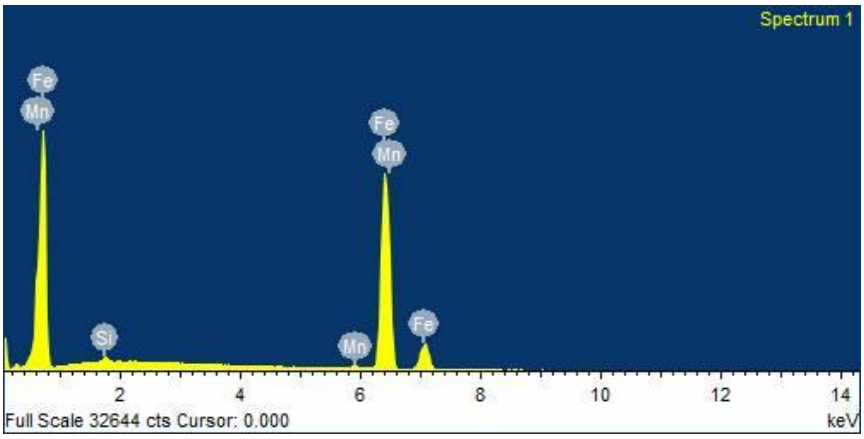


Figure 4. 5: XRD pattern for the 3CR12 stainless steel in an as received condition.

The EDS analysis of the mild steel is illustrated in Figures 4.6. In order to get the EDS results an area on the sample was analysed. The spectrum showed the presence of typical constituents of mild steel such as Iron (Fe), Manganese (Mn) and Silicon (Si). Table 4.1 gives the quantified elemental composition of mild steel from the EDS spectrum in Figure 4.6 which proves that the material is indeed mild steel**.**



a.



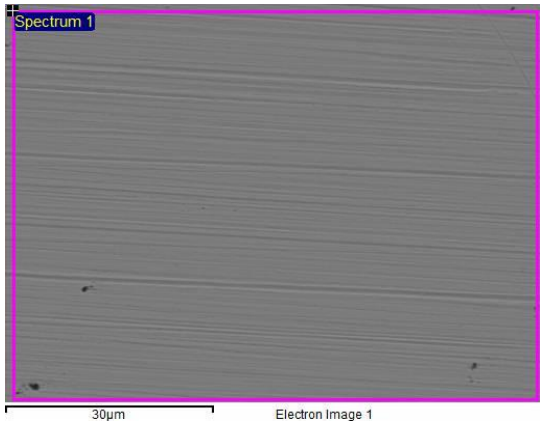
b.

Figure 4. 6: EDS for the mild steel sample (a) Scanned spectrum area (b) spectrum analysis.

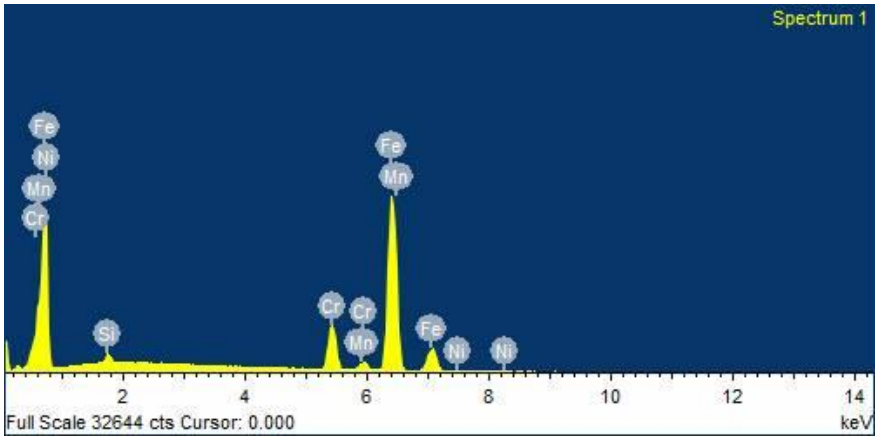
Table 4. 1: Elemental composition for the mild steel sample.

Element	Weight%	Atomic%
Si K	0.45	0.90
Mn K	1.04	1.05
Fe K	98.51	98.05
Totals	100.00	100

The EDS analysis of the 3CR12 stainless steel is illustrated in Figure 4.7. The spectrum shows the detection of major elements such as Chromium (Cr), Iron (Fe) and Nickel (Ni). Table 4.2 quantifies the composition of the elements detected from the EDS spectrum which proves that it is a typical composition for 3Cr12 stainless steel.



a.



b.

Figure 4. 7: EDS for the 3CR12 stainless steel sample (a) Scanned spectrum area (b) spectrum analysis.

Table 4. 2: Elemental composition for 3CR12 stainless steel.

Element	Weight%	Atomic%
Si K	0.83	1.62
Cr K	11.73	12.39
Mn K	0.99	0.99
Fe K	85.79	84.38
Ni K	0.66	0.62
Totals	100.00	100.00

Figure 4.8 is the XRD pattern for the cemented carbide button. The pattern indicates the presence of the WC and Co phases with no evidence of detrimental phases or impurities such as eta phase. Eta phase is known to increase hardness in cemented carbides resulting in loss of mechanical properties such as fracture toughness and strength.

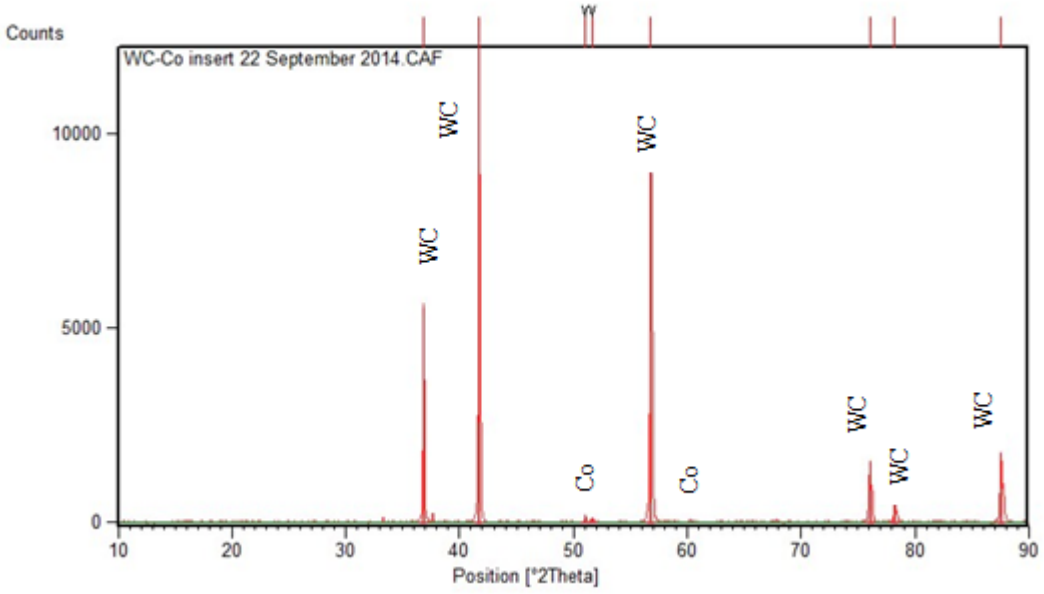
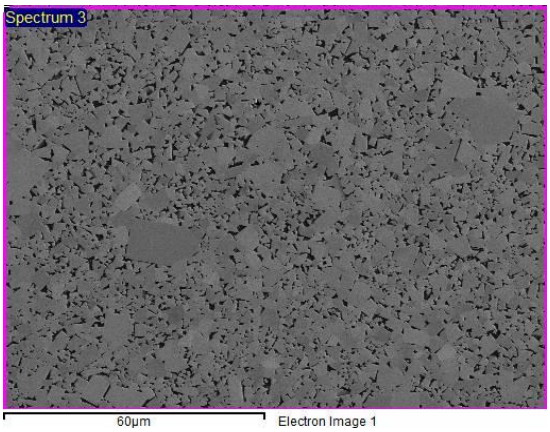
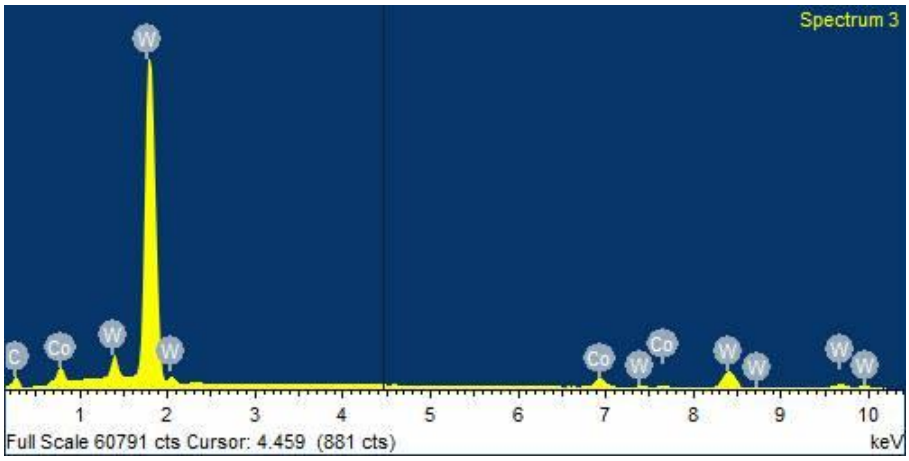


Figure 4. 8: XRD pattern for the WC-6 wt.% Co buttons in an as received condition.

Figure 4.9 illustrates the EDS analysis for the WC-6 wt.% Co cemented carbide button. The analysis on this sample was done on an area to generate the EDS map of elements detected. Table 4.3 gives quantified elemental composition of the WC-6 wt.% Co as shown on the spectrum analysis. Both Figure 4.9 and Table 4.3 confirmed that the buttons were indeed of composition WC-6 wt.% Co.



a.



b.

Figure 4. 9: EDS for the WC-6 wt.% Co button (a) Scanned spectrum area (b) spectrum analysis.

Table 4. 3: Elemental composition for WC-6 wt.% Co buttons.

Element	Weight%	Atomic%
C K	6.84	49.37
Co K	6.71	9.87
W M	86.45	40.76
Totals	100.00	100.00

4.1.3 Material properties

Table 4.4 highlights the physical and mechanical properties of cemented the carbide buttons (See Appendix A to C for detailed calculations of properties). The low porosity indicated the effectiveness of the sintering process. The density was equivalent to the typical range for cemented carbides with 6 wt.% Co [1], whereas the hardness was about 5-7% lower than the typical minimum hardness for this grade [1]. The lower hardness could have been as a result of grain coarsening and distribution during manufacturing. The fracture toughness of 14.6 $MPa.m^{1/2}$ is similar to that obtained by Scieszka [41] for a similar grade.

Table 4. 4: Mechanical and physical properties of the WC-6 wt.% Co Buttons.

Sample	Vickers Hardness HV_{30} ($kgf.mm^{-2}$)	Fracture Toughness K_{IC} ($MPA.m^{1/2}$)	Density ($g.cm^{-3}$)	Porosity (%)
WC-6 wt.% Co	1330±17	14.6±1.01	14.9±0.012	0.11±0.05

Table 4.5 lists the material properties of the steel counterfaces. The hardness obtained was typical for these materials while the density of these counterfaces was averaged at 7.7 $g.cm^{-3}$ [1].

Table 4. 5: Material properties of the mild steel and 3CR12 stainless steel.

Material	Vickers Hardness HV_{30} ($kgf.mm^{-2}$)	Density [$g.cm^{-3}$]
3CR12 stainless steel	171±2	7.67±0.010
Mild steel	156±1	7.78±0.037

4.2 Reciprocating wear

4.2.1 Wear of mild steel and 3CR12 stainless steel in distilled and synthetic mine water

Figures 4.10 and 4.11 are graphs showing the average cumulative volume loss of the mild steel against the cemented carbide buttons for a sliding distance of 319.5 m, in distilled water and synthetic mine water solutions. These figures show that the relationship between material volume loss and sliding distance is directly proportional.

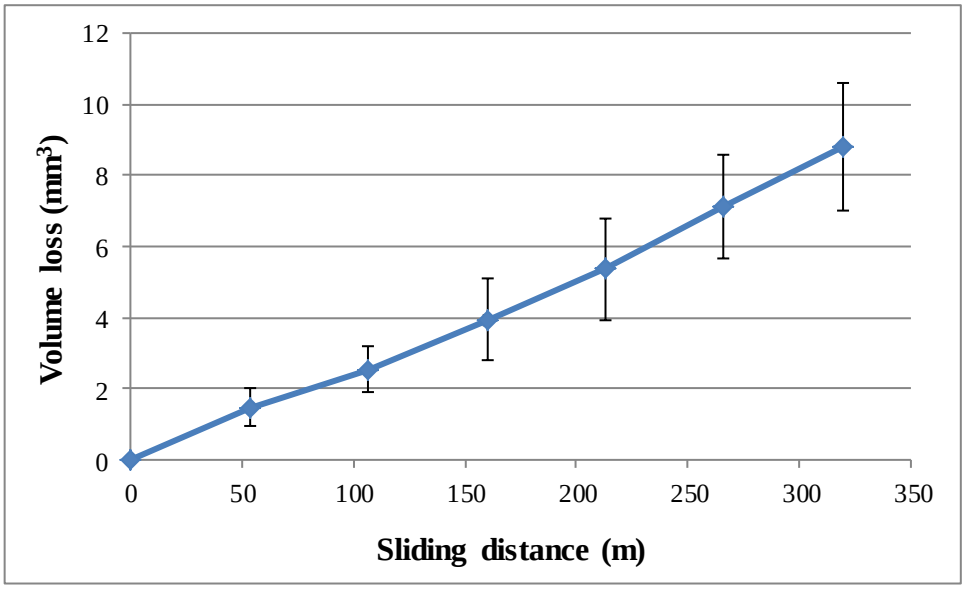


Figure 4. 10: Cumulative volume loss of the mild steel sliding against WC-6 wt.% Co buttons in distilled water.

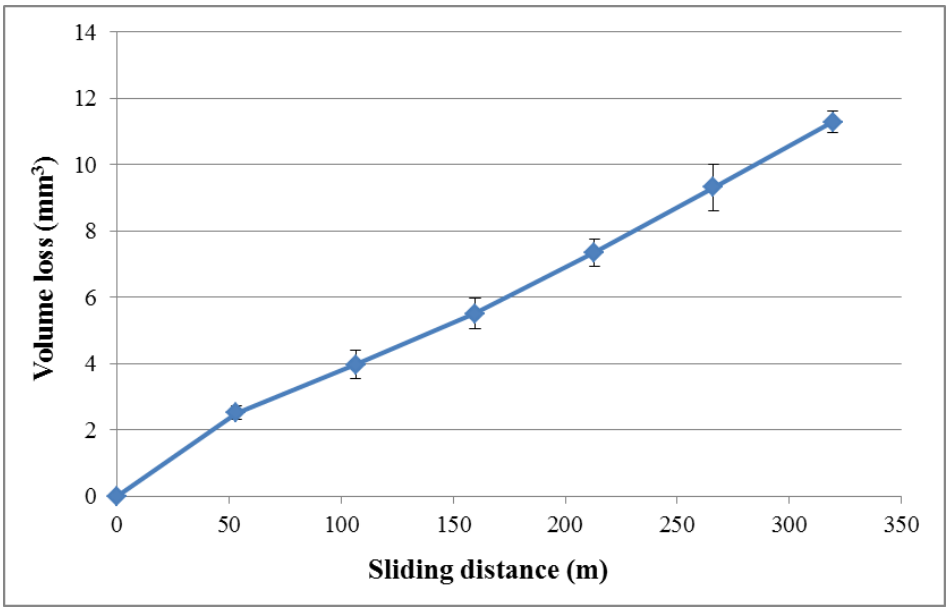


Figure 4. 11: Cumulative volume loss for the mild steel sliding against WC-6 wt.% Co buttons in synthetic mine water.

In Figure 4.12 the comparison between the average volume loss of the mild steel samples sliding against the WC-6 wt.% Co buttons in the two different solutions is shown. A consistently higher level of average material volume loss occurred on the mild steel samples exposed to synthetic mine water compared to those exposed to distilled water; indicating the aggressive nature of the synthetic mine water. It was also noted that the standard deviations of the volume loss on the samples exposed to synthetic mine water were smaller than those exposed to distilled water.

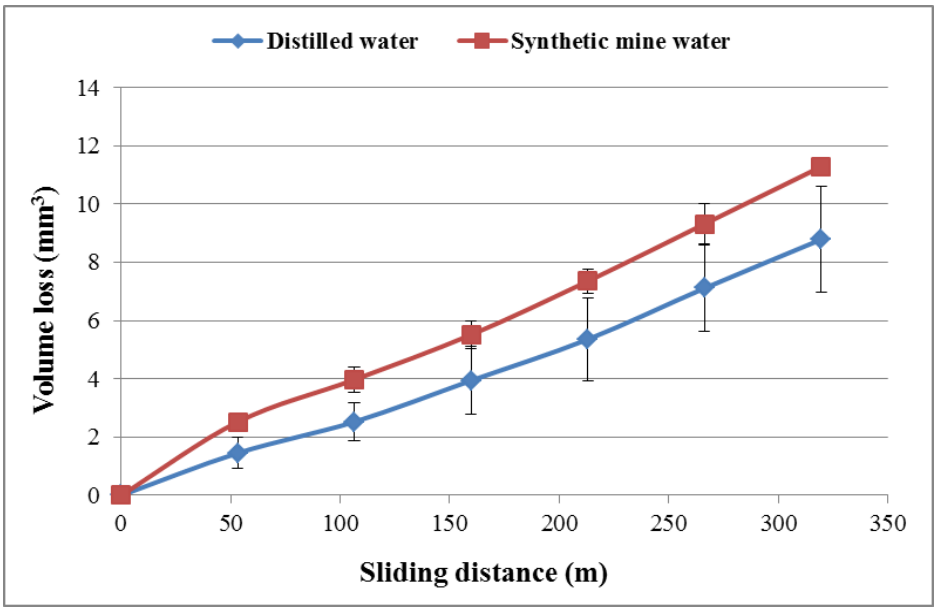


Figure 4. 12: Comparison of the cumulative volume loss of the mild steel sliding against WC-6 wt.% Co in distilled water and synthetic mine water.

Figures 4.13 and 4.14 illustrate the dimensional wear rate coefficients of the mild steel sliding against the WC-6 wt.% Co buttons in distilled water and synthetic mine water respectively. The dimensional wear coefficient is generally used to compare the wear rates of different materials [32]. In distilled water, an initial decrease in the wear rate coefficient was seen during the first 106 m of sliding followed by a slight, steady increase up to 320 m. In synthetic mine water, an initial decrease in the wear rate was noted. This response may be attributed to the running-in phase at the beginning of the wear process. In the mine water solution the wear rate then stabilised at a sliding distance of around 150 m and remained in this steady state for the duration of the test. The variations in the wear rates may be attributed to variations in microstructure and to the changing geometry at the point of contact, as the sliding distance increased.

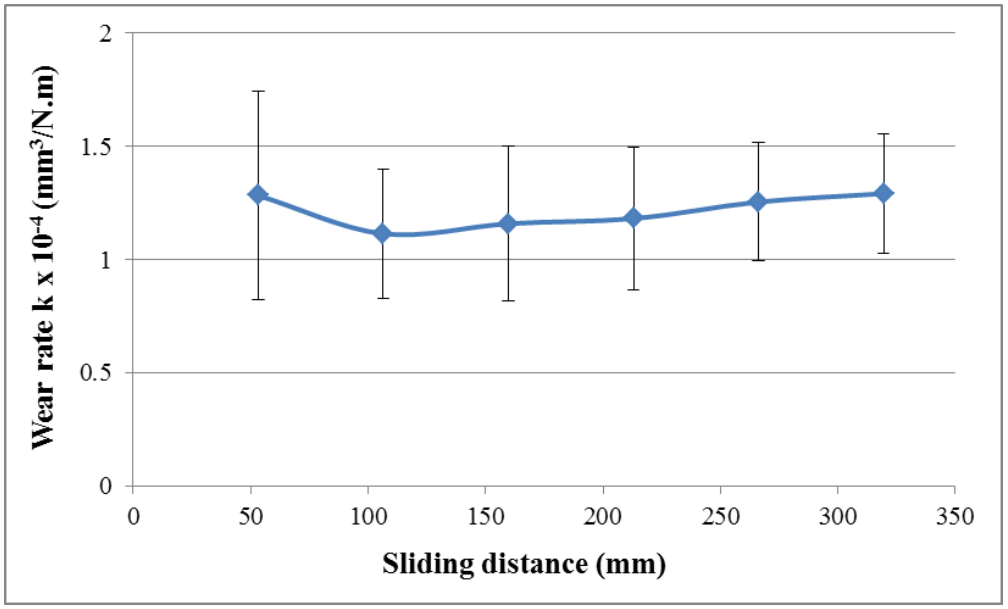


Figure 4. 13: Wear rate coefficient of the mild steel sliding against WC-6 wt.% Co buttons in distilled water.

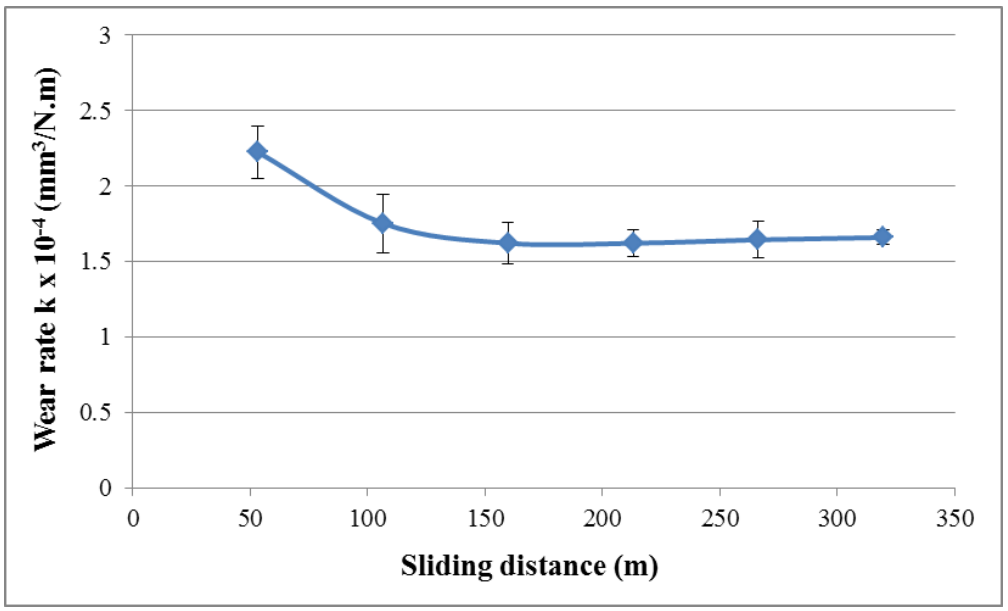


Figure 4. 14: Wear rate of the mild steel sliding against WC-6 wt.% Co buttons in synthetic mine water.

The comparison between the dimensional wear rate coefficients of the mild steel sliding against the WC-6 wt.% Co buttons in the two solutions is shown in Figure 4.15. The rapid stability of the mild steel's wear rate in the mine water solution compared to the distilled water was noted.

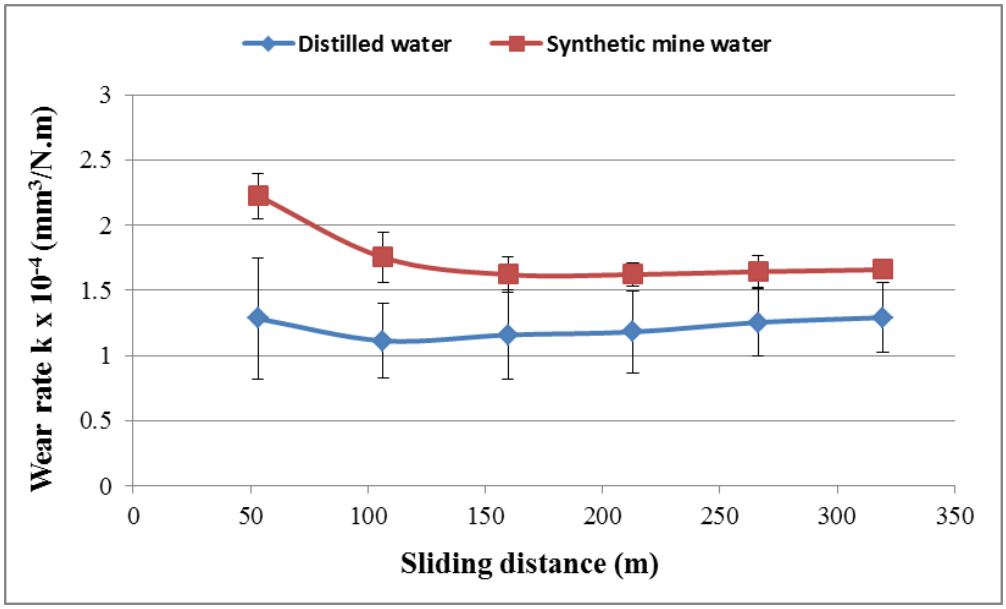


Figure 4. 15: Comparison of the wear coefficient of the mild steel sliding against WC-6 wt.% Co buttons in distilled and synthetic mine water.

Figures 4.16 and 4.17 show the average cumulative material volume loss of the 3CR12 stainless steel when sliding against the WC-6 wt.% Co buttons in distilled water and synthetic mine water respectively. A linear increase in volume loss was experienced as the sliding distance increased which indicates direct propotionally between sliding distance and volume loss. The behaviour of 3CR12 stainless steel is therefore similar to that of the mild steel samples.

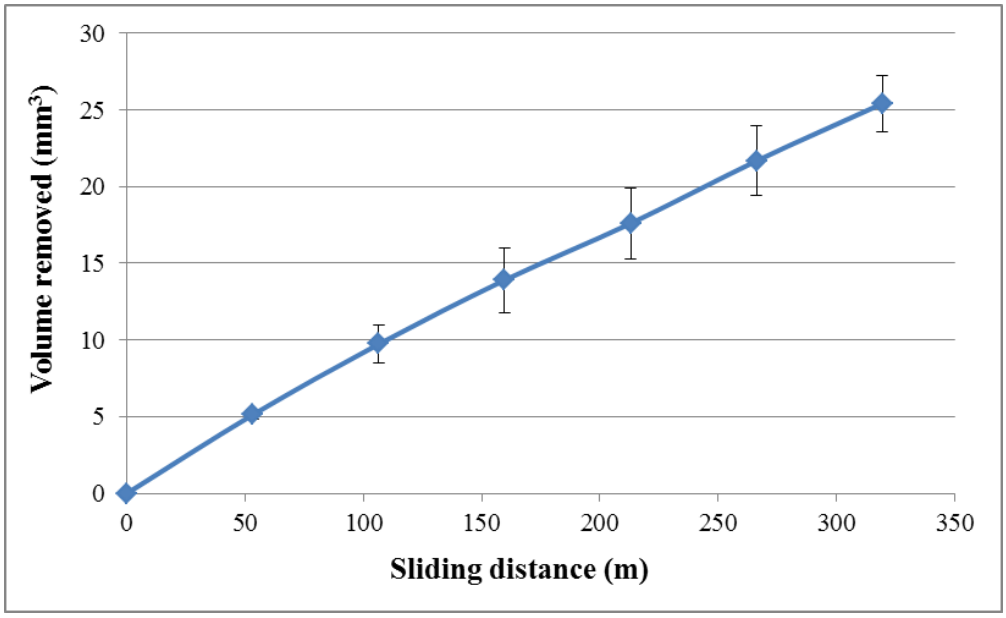


Figure 4. 16: Cumulative volume loss of the 3CR12 stainless steel sliding against WC-6 wt.% Co buttons in distilled water.

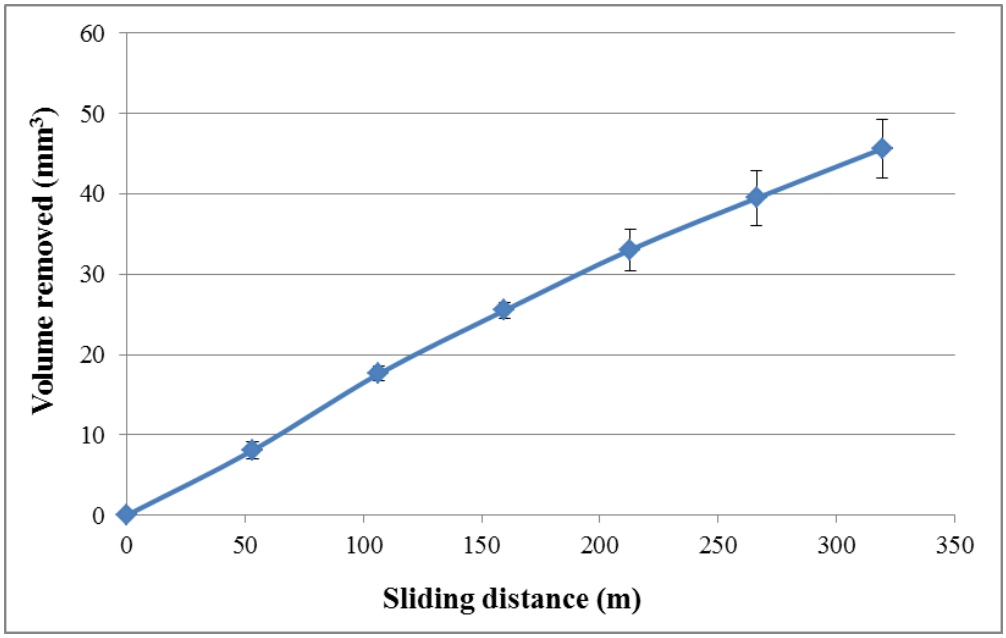


Figure 4. 17: Cumulative volume loss of the 3CR12 stainless steel sliding against WC-6 wt.% Co buttons in synthetic mine water solution.

Figure 4.18 gives the comparion of the average material volume loss for the 3CR12 stainless steel in the two different solutions. The 3CR12 stainless steel samples experienced a distinctly higher volume loss in sythetic mine water compared to distilled water. These results are once again an indication of the aggressive nature of the synthetic mine water solution. The standard deviations on the 3CR12 stainless steel was

found to be low compared to the mild steel and this may be attributed to the uniformity of the microstructure of the 3CR12 strainless steel.

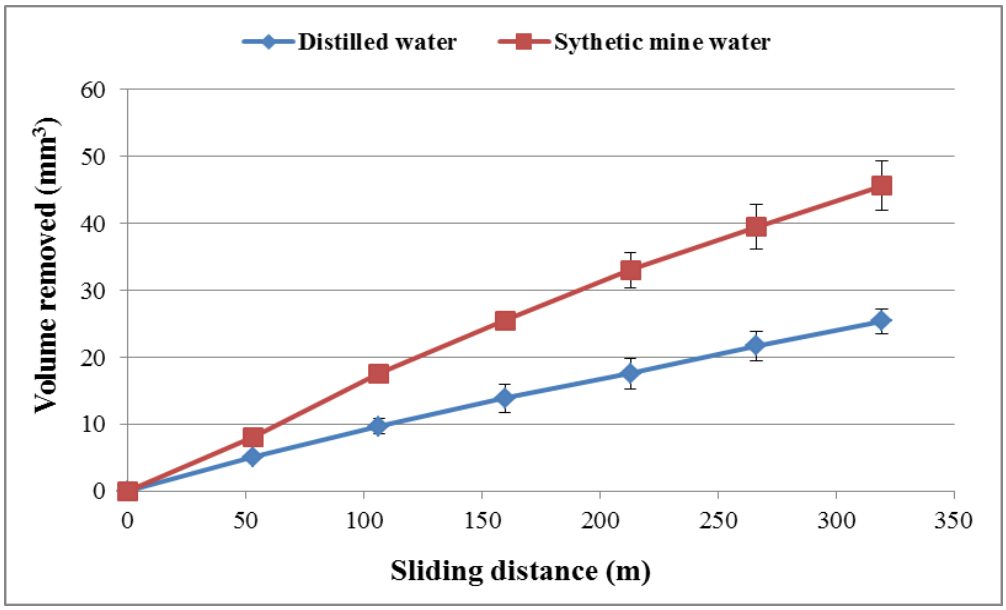


Figure 4. 18: Cumulative volume loss of the 3CR12 stainless steel sliding against WC-6 wt.% Co buttons in distilled water and synthetic mine water solutions.

Figures 4.19 and 4.20 show the dimensional wear rate coefficients of the 3CR12 stainless steel in the distilled and synthetic mine water solution respectively. In distilled water the wear rate coefficient decreases steadily for the duration of the test. In synthetic mine water an initial minor increase in the wear rate coefficient was observed for the first 109 m of sliding water followed by a steady decrease for the remainder of the test.

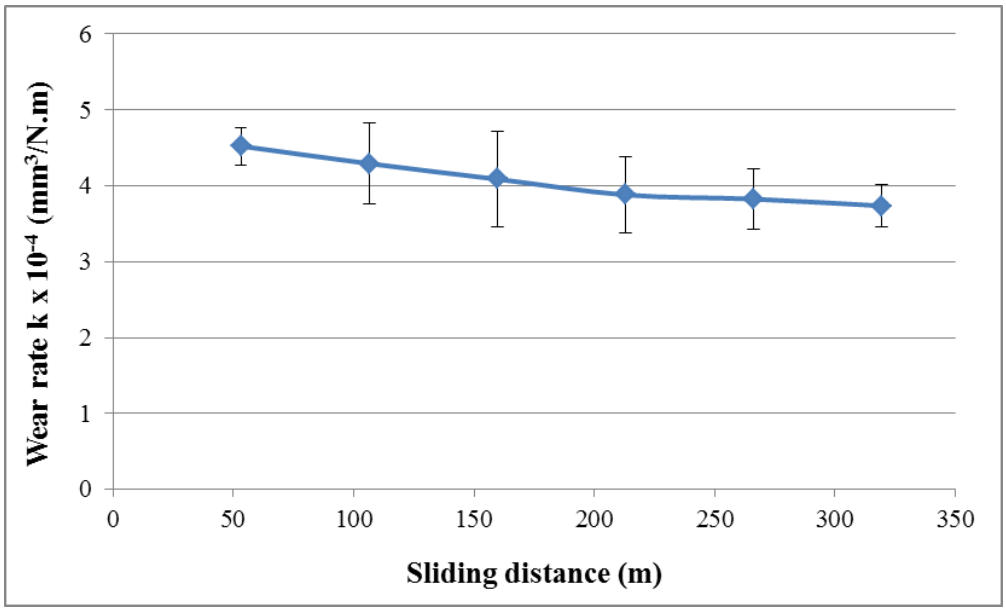


Figure 4. 19: Wear rate coefficient of the 3CR12 stainless steel sliding against WC-6 wt.% Co buttons in distilled water solution.

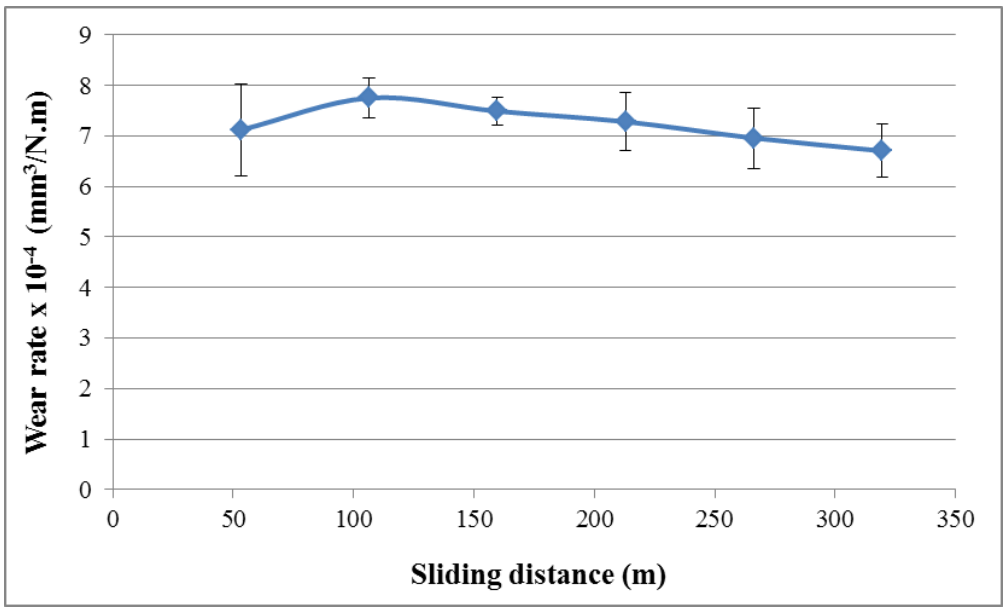


Figure 4. 20: Wear rate coefficient of the 3CR12 stainless steel sliding against WC-6 wt.% Co buttons in synthetic mine water solution.

Figure 4.21 illustrates the comparison of the wear rate coefficients for the 3CR12 stainless steels in both solutions. The wear rate coefficient was found to be higher in synthetic mine water when compared to that in distilled water.

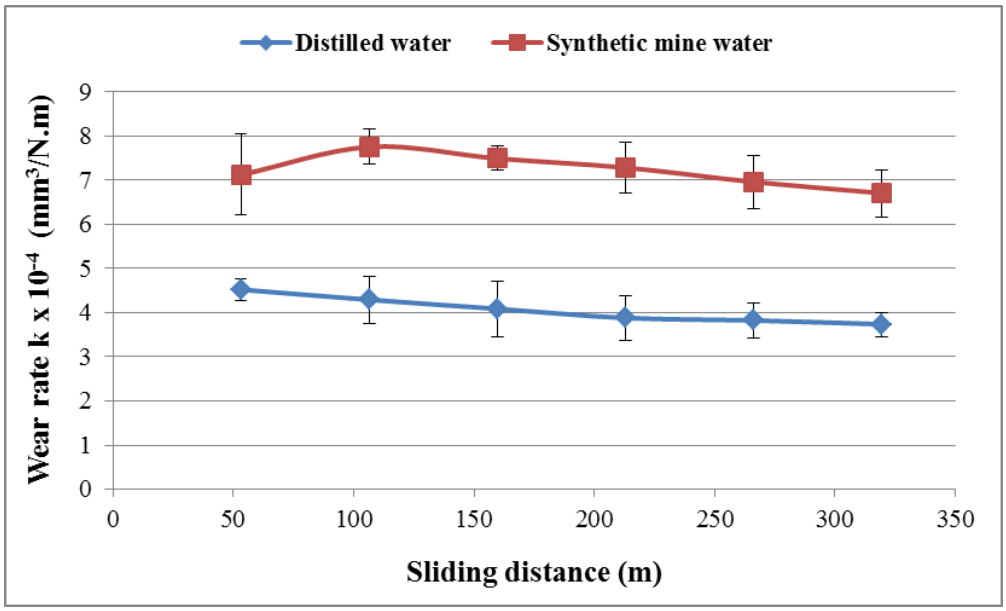


Figure 4. 21: Comparison of wear rate coefficient for the 3CR12 stainless steel sliding against WC-6 wt.% Co in distilled water and synthetic mine water solutions.

Figure 4.22 shows the specific wear rate coefficients for the mild steel and the 3CR12 stainless steel sliding for 320 m against the WC-6wt%Co buttons in distilled water and synthetic mine water. Despite the high initial hardness, the 3CR12 stainless steel experienced higher wear rate than mild steel in both environments. The high wear rate may be attributed to the difference in work hardening rate between mild steel and 3CR12 stainless steel.

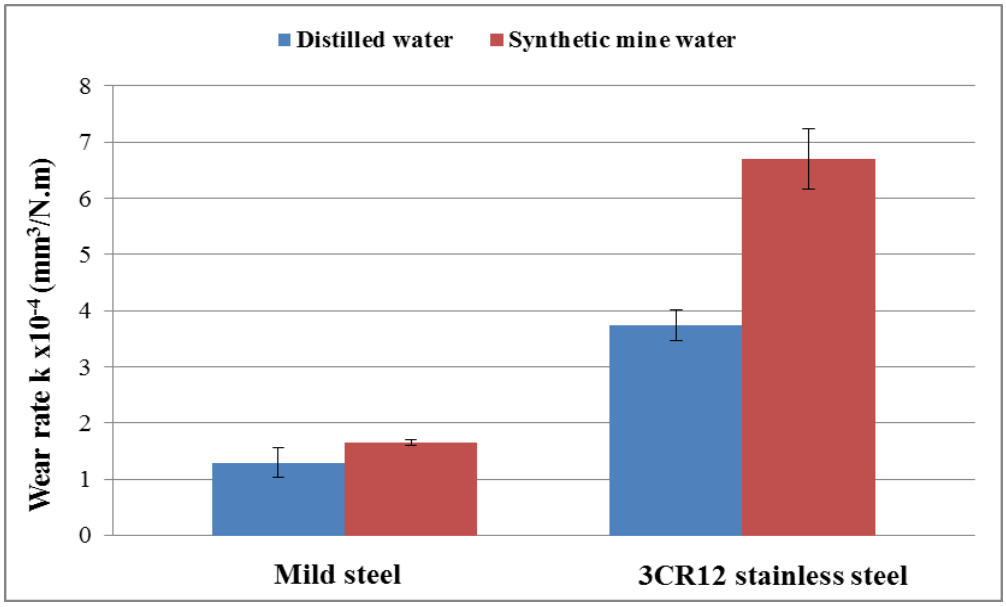


Figure 4. 22: Comparison of the wear rate coefficients of the mild steel and 3CR12 stainless steel in distilled water and synthetic mine water solutions.

4.2.2 Wear of WC-6 wt. % Co buttons in distilled water and synthetic mine water

A comparison of the average material volume loss of the WC-6 wt.% Co cemented carbide buttons when sliding against mild steel and 3CR12 stainless steel in distilled water and synthetic mine water is shown by Figure 4.23. A comparison of the wear rates coefficient is illustrated in Figure 4.24. The material volume loss of the carbide buttons when mild steel was used as a counterface is similar in distilled water and synthetic mine water. However there was a pronounced difference, approximately 54 %, in material volume loss for the carbide buttons in the two solutions when 3CR12 stainless steel was used as a counterface.

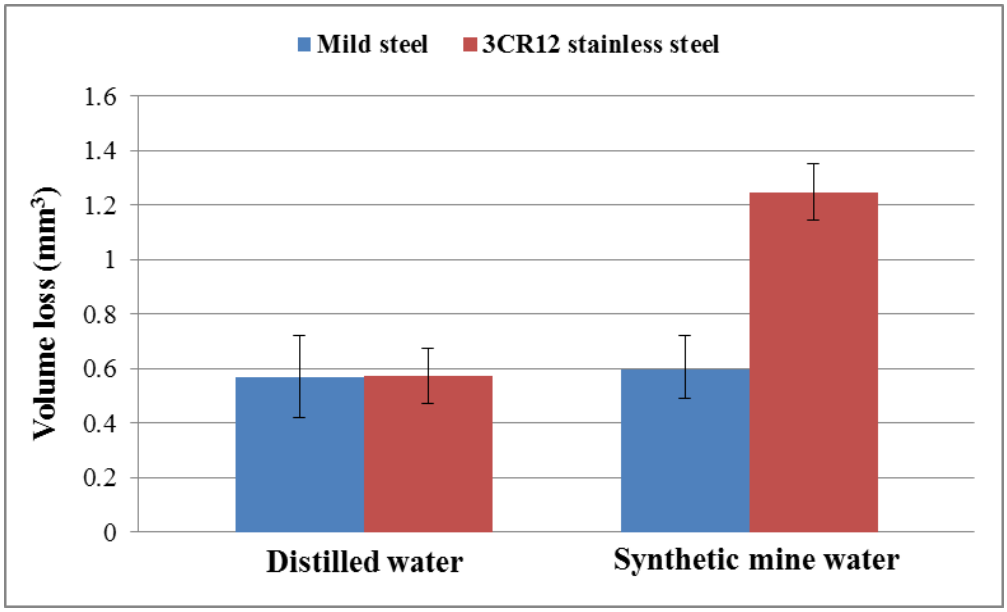


Figure 4. 23: Comparison of the average material volume loss of the WC- 6wt. % Co buttons sliding against mild steel and 3CR12 stainless steel in distilled water and synthetic mine solutions.

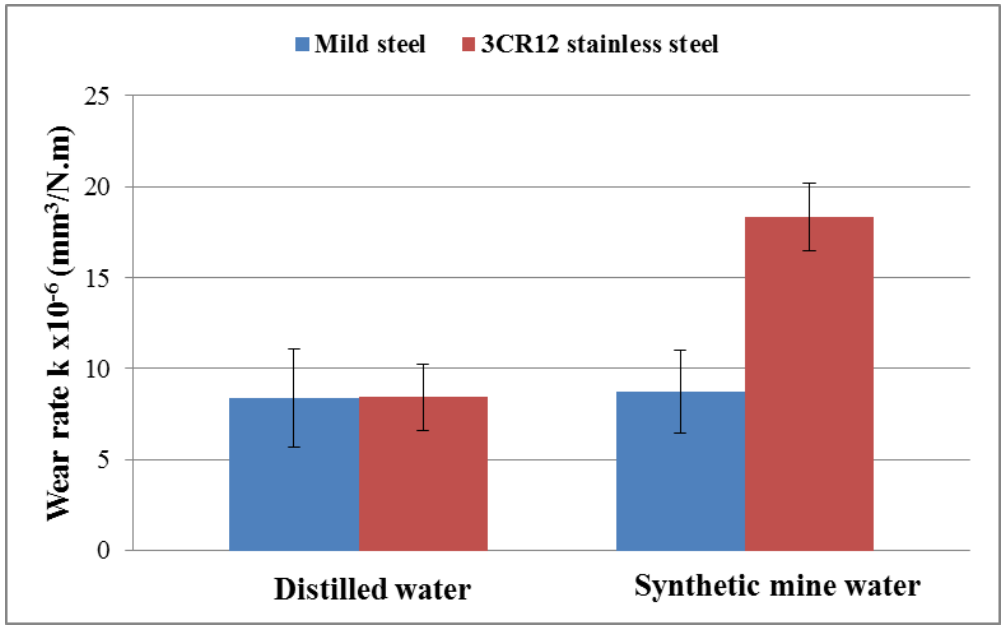


Figure 4. 24: Comparison of the average material volume loss of the WC-6 wt.% Co buttons sliding against mild steel and 3CR12 stainless steel in distilled water and synthetic mine solutions.

4.3 Wear scar analyses

4.3.1 Typical wear tracks

Figure 4.25 shows a typical wear track on the steel counterface while Figure 4.26 shows wear mark on the WC-6 wt.% Co (See appendix E for more wear tracks). These wear tracks were as a result of sliding action between the two bodies. The material removed on the surface of the steel counterface lead to the formation of the track and metal upsets as seen on the edges of the track which is an indication of deformation or material smearing.



Figure 4. 25: Typical wear track on the steel counterfaces caused by the WC-6 wt.% Co buttons during sliding.

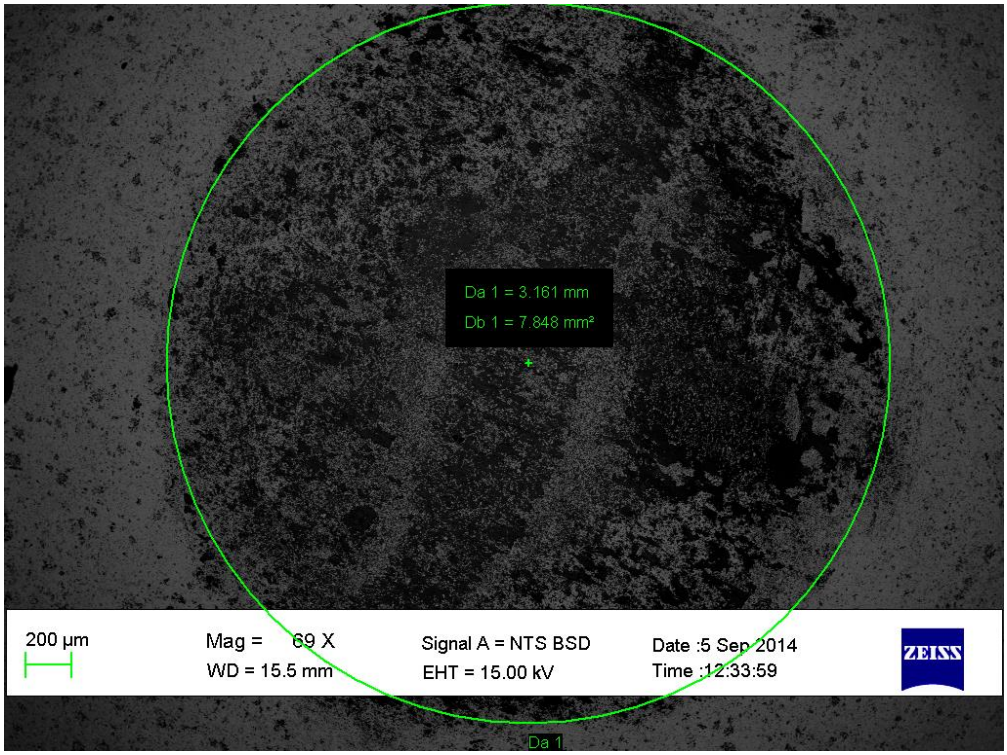


Figure 4. 26: Typical wear scar on the WC-6 wt.% Co buttons caused by the sliding action.

4.3.2 Wear scars of mild steel and WC-6 wt.% Co buttons in distilled water and synthetic mine water

Figure 4.27 shows the wear scars of mild steel in distilled and synthetic mine water. The wear scar reflects scratching, plastic deformation and micro cracking of the mild steel samples when exposed to distilled water (a and b) whereas severe plastic deformation, micro cracking and cold welding was seen in synthetic mine water (c and d). As stated in section 4.3.1, evidence of plastic deformation was seen on the edges of the wear tracks.

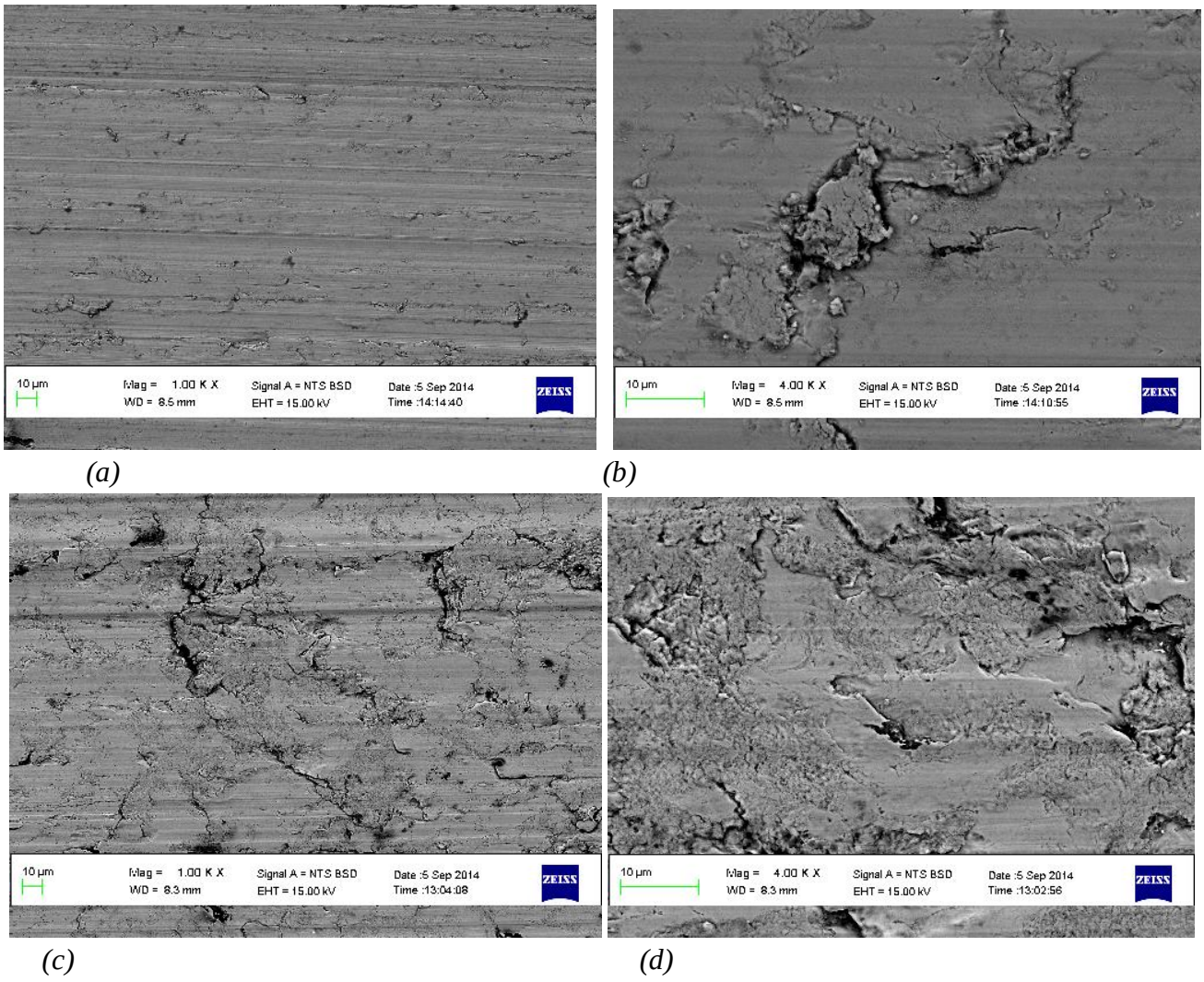
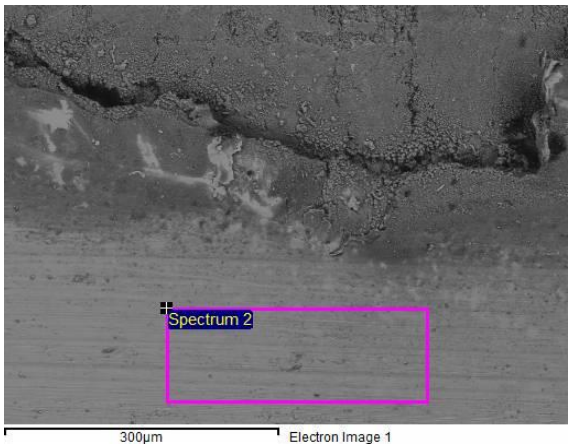
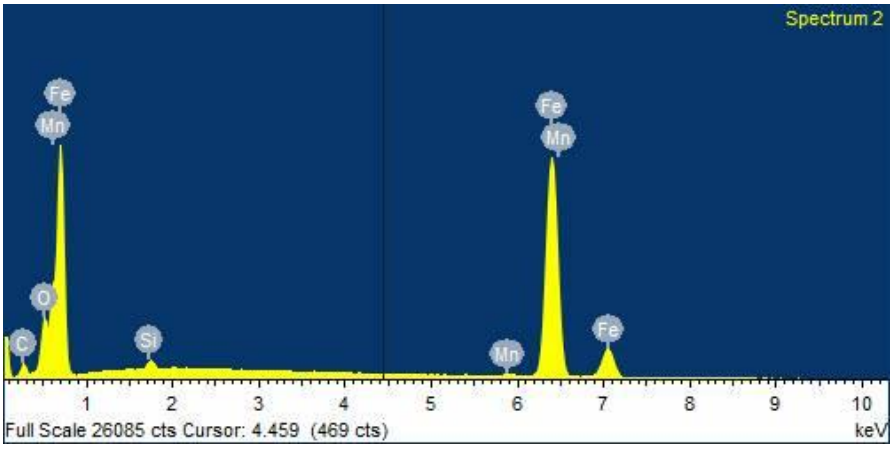


Figure 4. 27: Wear scars of mild steel sample sliding against WC-6 wt.% Co, (a) and (b) in distilled water, (c) and (d) in synthetic mine water.

Figures 4.28 and 4.29 indicate the EDS spectrum of the wear track on the mild steel sample in distilled water and synthetic mine water respectively. Tables 4.6 and 4.17 show the elemental composition of the spectrums. Both spectra, showed the presence of oxygen, whereas the EDS spectrum on the wear scar of the mild steel in synthetic mine water showed the presence of synthetic mine water, components such as calcium (Ca), which may indicate oxide formation on the worn surface.



a.

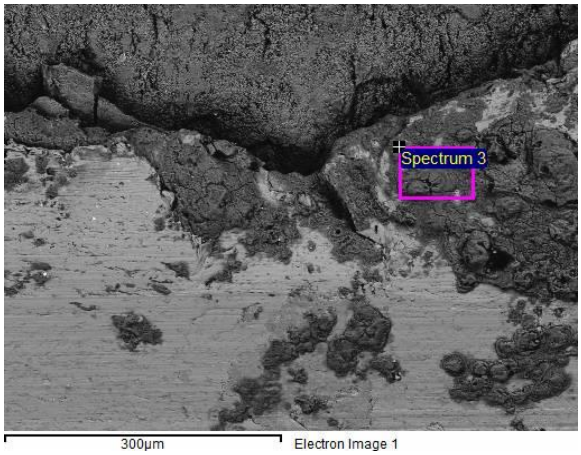


b.

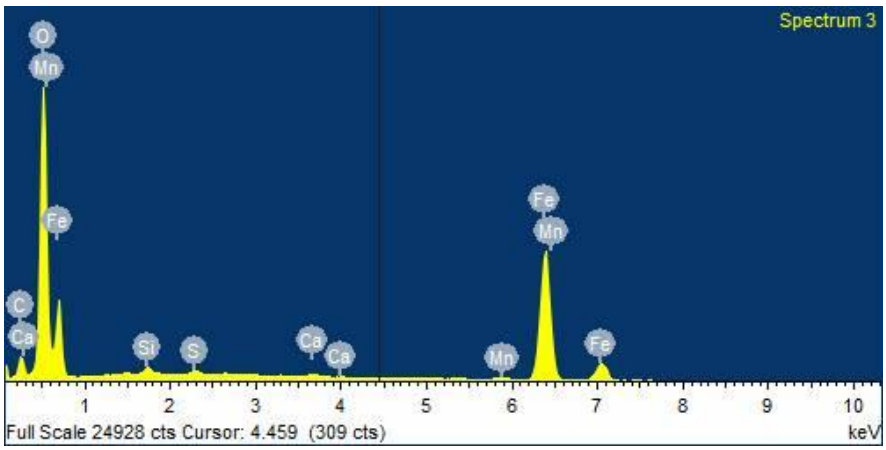
Figure 4. 28: EDS analyses on the wear scar of the mild steel in distilled water (a) spectrum area (b) spectrum analysis.

Table 4. 6: Elemental composition of mild steel wear scar in distilled water.

Element	Weight%	Atomic%
C K	5.01	17.43
O K	5.95	15.53
Si K	0.59	0.88
Mn K	0.68	0.51
Fe K	87.77	65.64
Totals	100.00	100.00



a.



b.

Figure 4. 29: EDS analyses on the wear scar of the mild steel in synthetic mine water (a) Scanned spectrum area (b) spectrum analysis.

Table 4. 7: Elemental composition of mild steel wear scar in synthetic mine water.

Element	Weight%	Atomic%
C K	6.79	15.11
O K	33.48	55.91
Si K	0.48	0.46
S K	0.27	0.23
Ca K	0.36	0.24
Mn K	0.73	0.35
Fe K	57.88	27.69
Totals	100.00	100.00

Figure 4.30 shows the worn surface of the WC-6 wt.% Co buttons in distilled water and synthetic mine water sliding against the mild steel counterface. The wear mechanisms

of the buttons in both environments were found to be similar. Plastic deformation and removal of the ductile cobalt binder occurs first, thereby exposing the WC carbide grains to the environment which causes cracking. Adhesion of the counterface to the buttons occurred during wear, and this is attributed to the hardness differences between the buttons and the counterfaces.

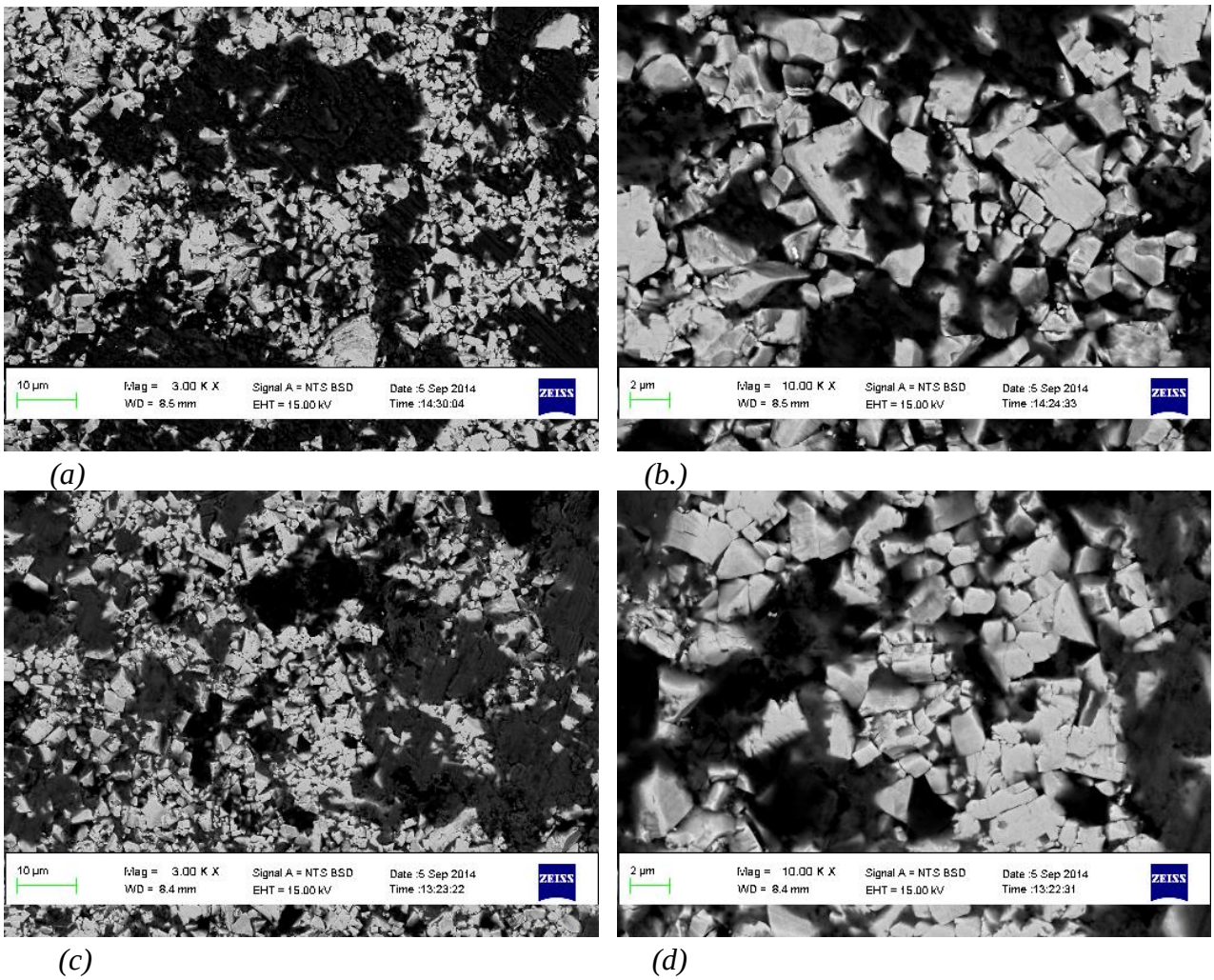
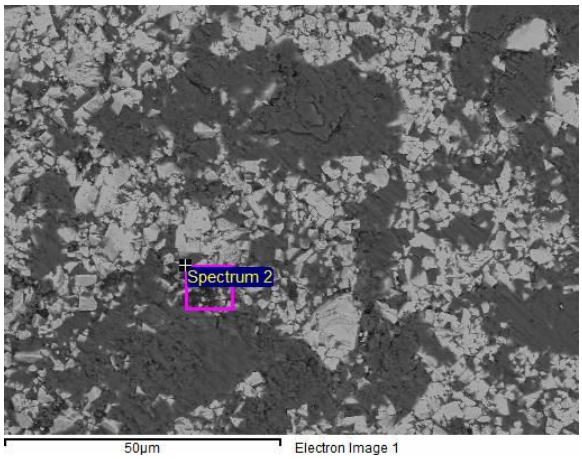


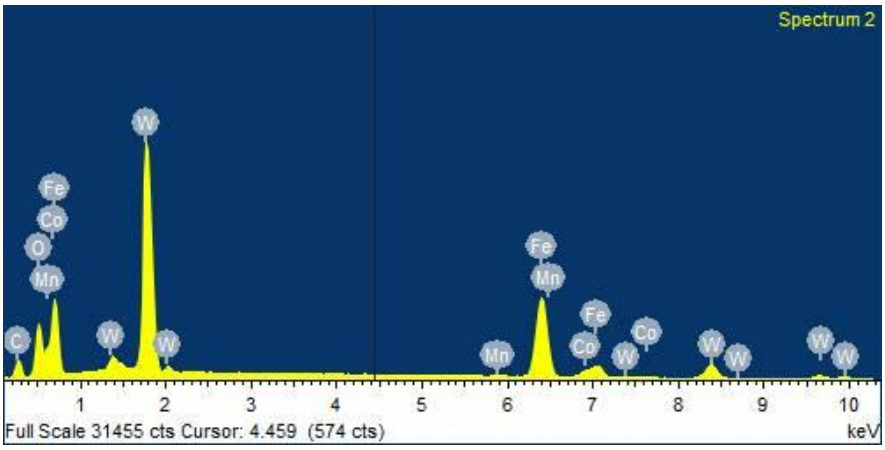
Figure 4. 30: Wear scars of WC-6 wt.% Co button sliding against mild steel, (a) & (b) in distilled water and (c) & (d) in synthetic mine water.

Figure 4.31 and Figure 4.32 are EDS spectra taken on the contact area of the WC-6 wt.% Co button after sliding against mild steel in distilled water and synthetic mine water respectively. Tables 4.8 and 4.9 provide the elemental composition done on the wear scar of the WC-6 wt.% Co buttons in the distilled water and synthetic mine water. The spectra indicate the presence of mild steel constituents on the wear scars of the cemented carbide buttons and this confirms that adhesion occurred during sliding. The

oxygen detected by the EDS analysis indicates that the possibility of oxidation with the highest concentration found in the synthetic mine water solution.



a.

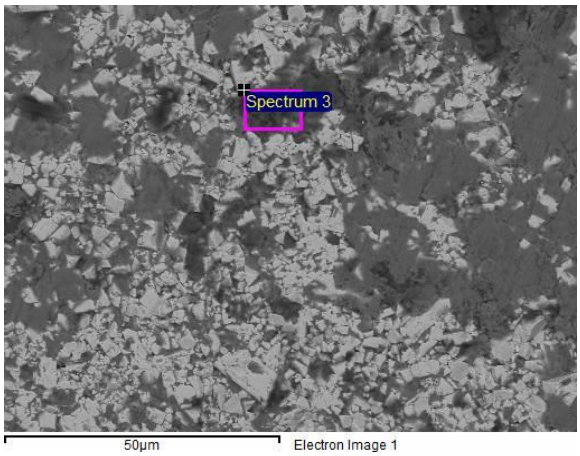


b.

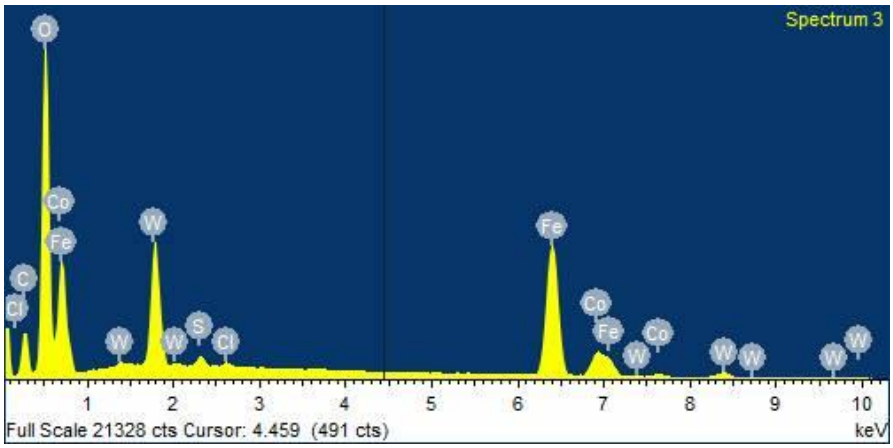
Figure 4. 31: EDS analyses on the wear scar of the WC-6 wt.% Co in distilled water (a) Scanned spectrum area (b) spectrum analysis.

Table 4. 8: Elemental composition on WC-6 wt.% Co button wear scar in distilled water.

Element	Weight%	Atomic%
C K	3.70	13.85
O K	4.17	11.72
Si K	0.44	0.70
Mn K	0.80	0.65
Fe K	90.89	73.09
Totals	100.00	100.00



a.



b.

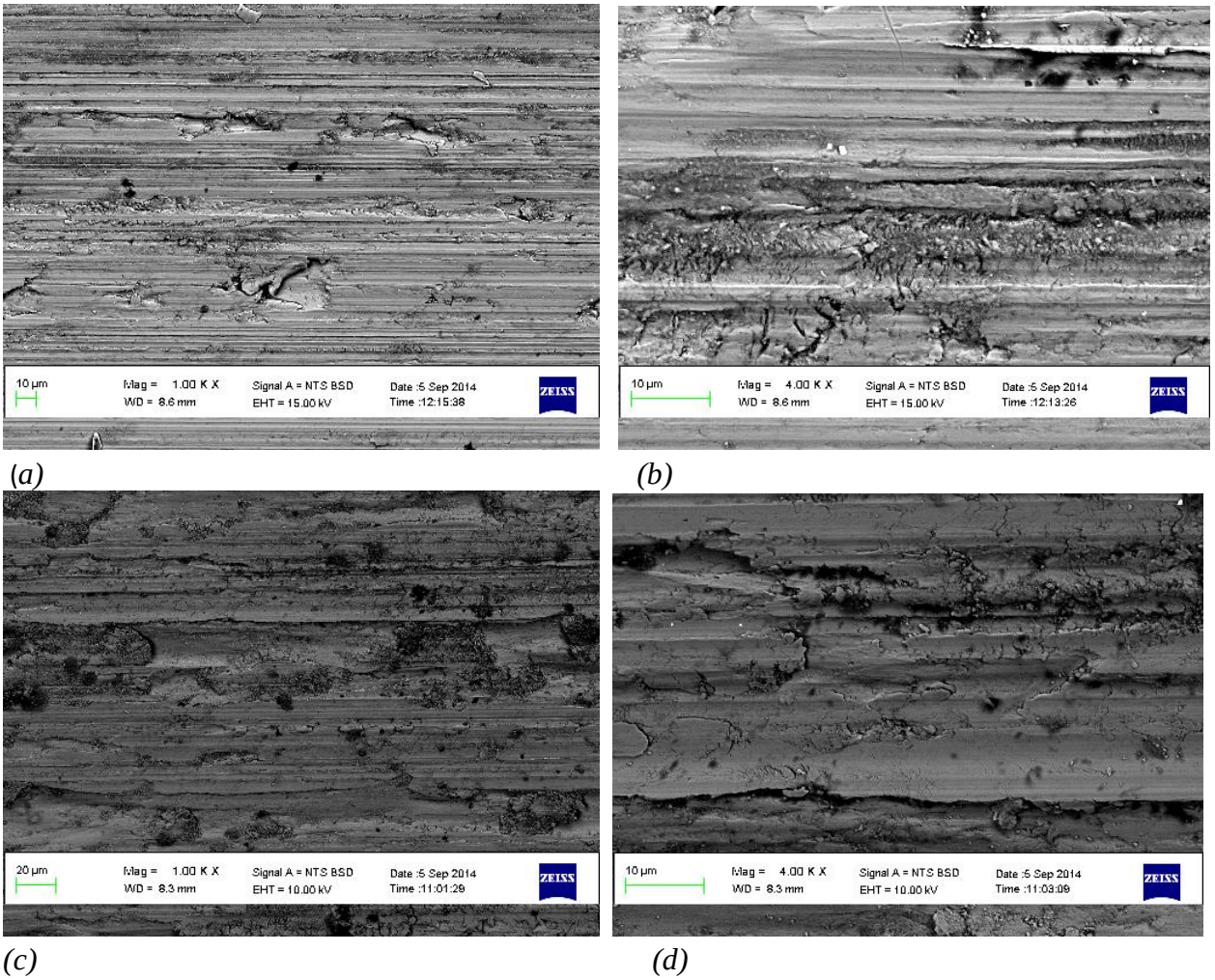
Figure 4. 32: EDS analyses on the wear scar of the WC-6 wt.% Co in synthetic mine water (a) Scanned spectrum area (b) spectrum analysis.

Table 4. 9: Elemental composition on cemented carbide button wear scar in synthetic mine water.

Element	Weight%	Atomic%
C K	8.74	20.66
O K	30.30	53.79
S K	0.56	0.50
Cl K	0.30	0.24
Fe K	36.49	18.56
Co K	7.96	3.84
W M	15.64	2.42
Totals	100.00	100.00

4.3.2 Wear scars of the stainless steel counterface and WC-6 %wt. Co in distilled water and synthetic mine water

Wear scars of the 3CR12 stainless steel counterface produced by the WC-6 wt.% Co during sliding are given by Figure 4.33 where (a) and (b) represent the distilled water environment, and (c) and (d) depict the synthetic mine water environment respectively. Shearing and micro peeling of the surface material followed by cold welding is seen on these wear scars. The damage was severe in synthetic mine water, and is normally referred to as galling [1].

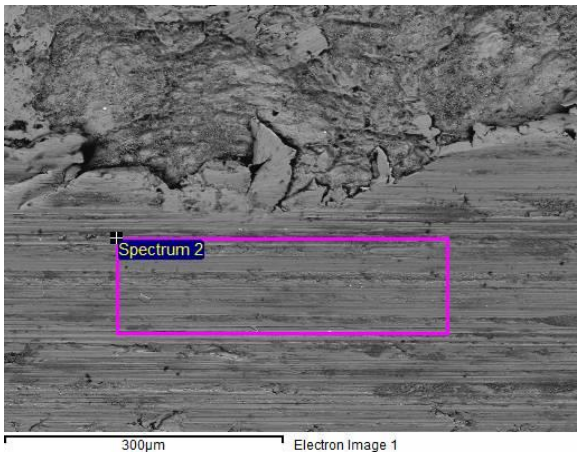


(a) *(b)*

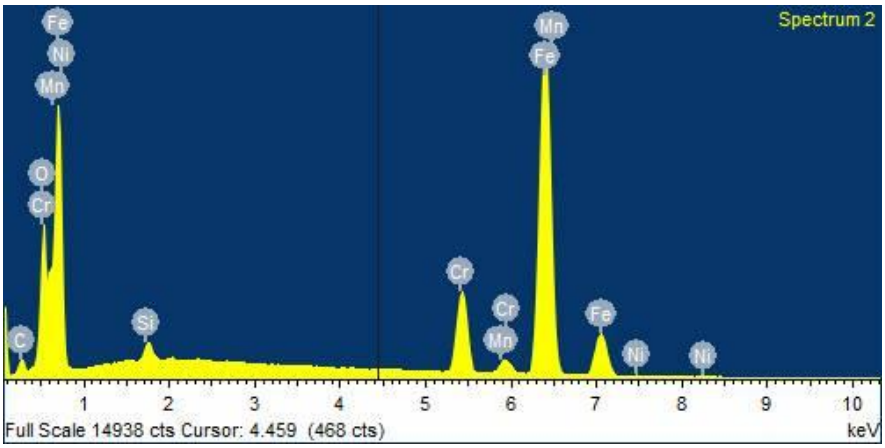
(c) *(d)*

Figure 4. 33: Wear scars of 3CR12 stainless steel, (a), (b) in distilled water and (c), (d) in synthetic mine water.

The EDS spectra of the 3CR12 stainless steel samples in distilled water and synthetic mine water are shown in Figures 4.34 and 4.35 respectively. These analyses were done in the area within the wear tracks. Tables 4.10 and 4.11 show the elemental composition and EDS spectrum on the wear scar of the 3CR12 stainless steel in synthetic mine water showed presence of synthetic mine water components such as calcium and chlorine.



a.

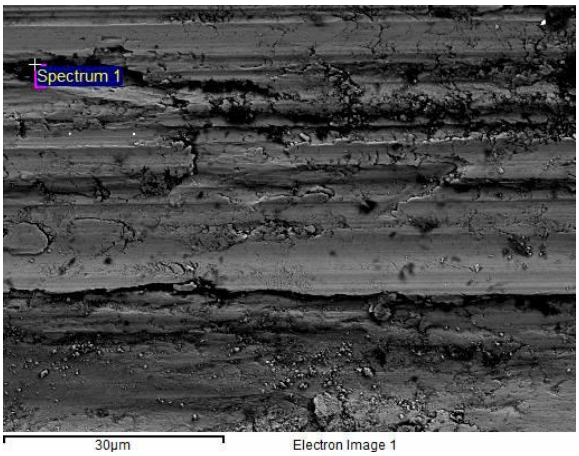


b.

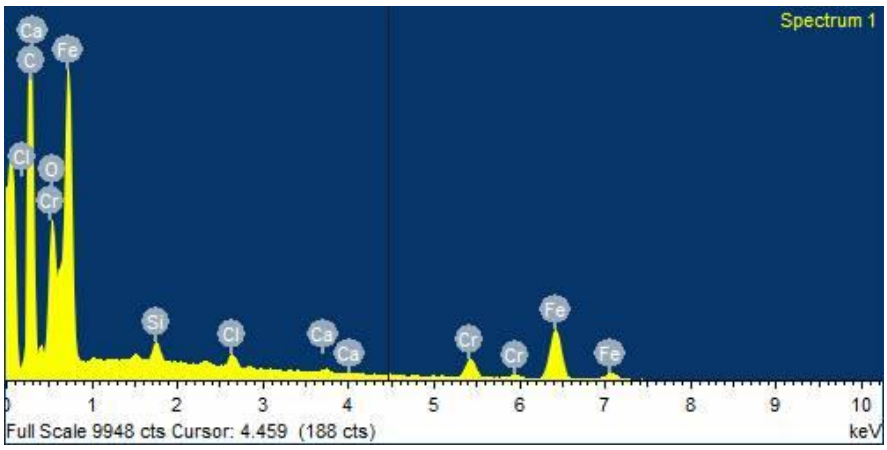
Figure 4. 34: EDS analyses on the wear scar of the 3CR12 stainless steel in distilled water (a) Scanned spectrum area (b) spectrum analysis.

Table 4. 10: Elemental composition on 3CR12 stainless steel wear scar in distilled water.

Element	Weight%	Atomic%
C K	3.10	10.94
O K	7.60	20.15
Si K	0.74	1.11
Cr K	10.35	8.44
Mn K	0.91	0.70
Fe K	76.74	58.25
Ni K	0.57	0.41
Totals	100.00	100.00



a.



b.

Figure 4. 35: EDS analyses on the wear scar of the 3CR12 stainless steel in synthetic mine water (a) Scanned spectrum area (b) spectrum analysis.

Table 4. 11: Elemental composition on 3CR12 stainless steel wear scar in synthetic mine water.

Element	Weight%	Atomic%
C K	24.94	55.66
O K	6.19	10.37
Si K	0.66	0.63
Cl K	0.80	0.61
Ca K	0.32	0.22
Cr L	9.23	4.76
Fe L	57.85	27.76
Totals	100.00	100.00

Figure 4.36 shows the wear scars of the WC-6 wt.% Co buttons when sliding against stainless steel in both synthetic mine water and distilled water. Similar mechanisms as those found against mild steel were observed, wherein plastic deformation and extrusion of the soft Co phase occurred leaving the WC grains exposed and unsupported, resulting in micro-cracking followed by grain pull out.

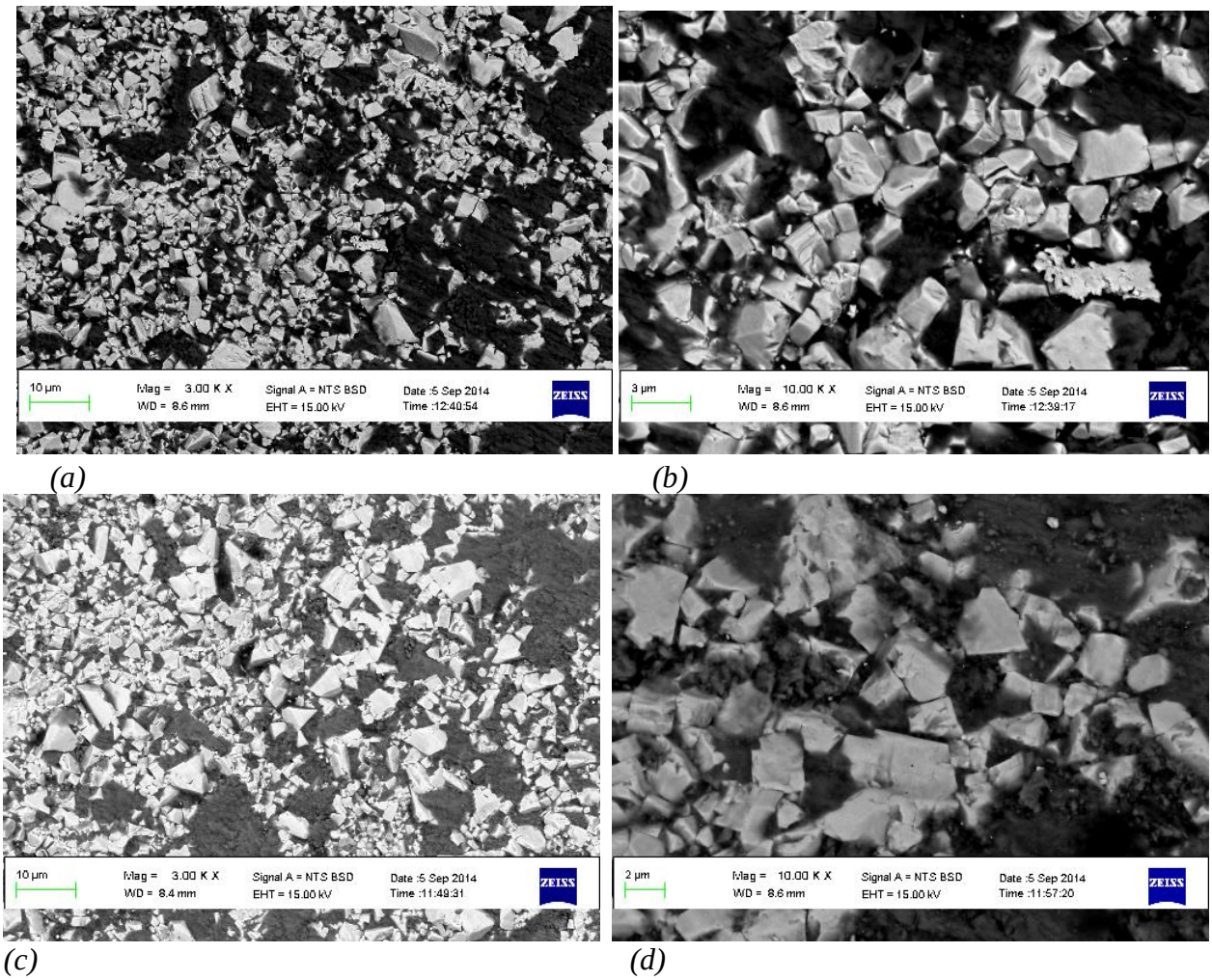
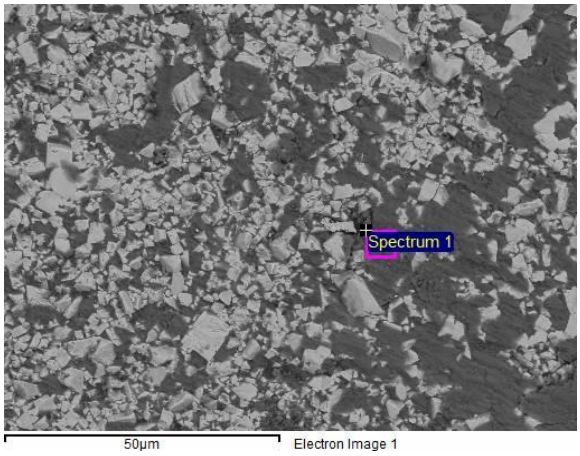
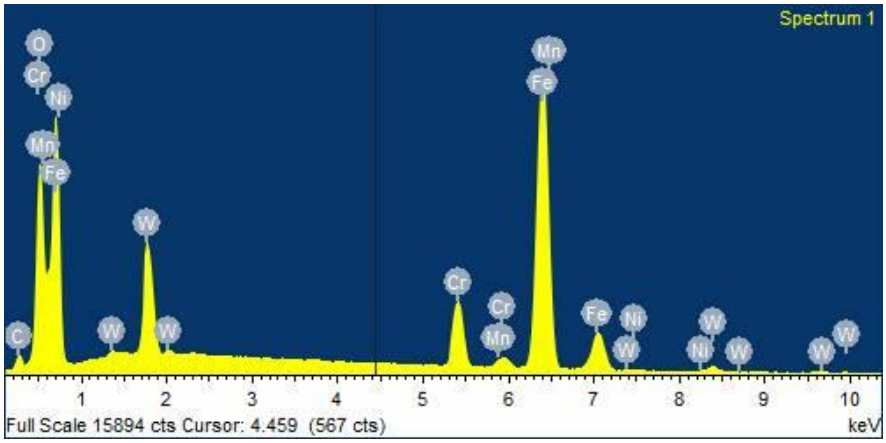


Figure 4. 36: Wear scars of WC-6 wt.% Co buttons (a) & (b) in distilled water, (c) & (d) in synthetic mine water.

The EDS spectra of the WC-6 wt.% Co buttons sliding against 3CR12 stainless steel in distilled water and synthetic mine water are shown in Figures 4.37 and Figure 4.38 respectively. All spectra show the presence of the steel's constituents, which is an indication of adhesion taking place during sliding. The composition of elements found on the wear scars is given in Tables 4.12 and 4.13, Oxygen was detected in both environments and the presence of synthetic mine water constituents were also noted on the wear scars.



a.

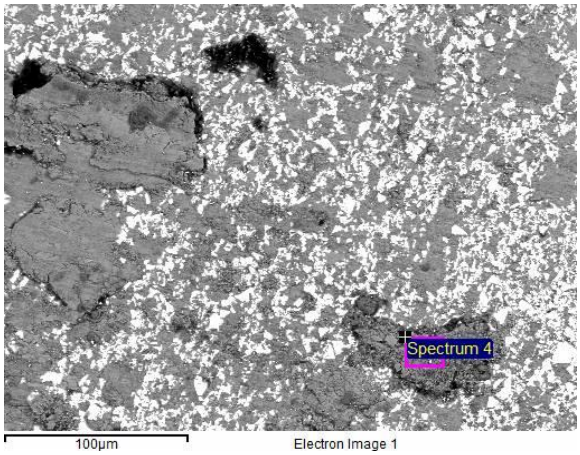


b.

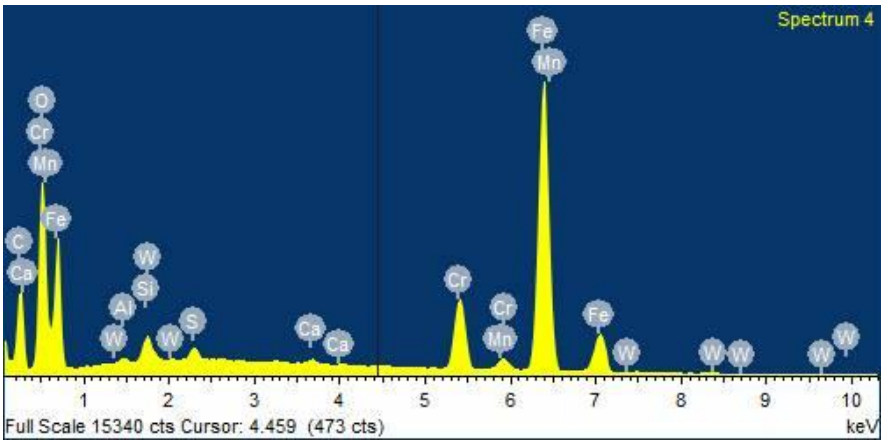
Figure 4. 37: EDS analyses on the wear scar of the WC-6 wt.% Co in distilled water (a) Scanned spectrum area (b) spectrum analysis.

Table 4. 12: Elemental composition on WC-6 wt.% Co button wear scar in distilled water.

Element	Weight%	Atomic%
C K	2.64	9.32
O K	11.84	31.42
Cr K	8.25	6.74
Mn K	0.63	0.48
Fe K	64.32	48.92
Ni K	0.55	0.40
W M	11.78	2.72
Totals	100.00	100.00



a.



b.

Figure 4. 38: EDS analyses on the wear scar of the WC-6 wt.% Co in synthetic mine water (a) Scanned spectrum area (b) spectrum analysis.

Table 4. 13: Elemental composition on WC-6 wt.% Co button wear scar in synthetic mine water.

Element	Weight%	Atomic%
C K	13.14	33.87
O K	12.60	24.38
Al K	0.17	0.20
Si K	0.57	0.63
S K	0.48	0.46
Ca K	0.24	0.19
Cr K	8.48	5.05
Mn K	0.59	0.33
Fe K	62.62	34.71
W M	1.09	0.18
Totals	100.00	100.00

4.4 Corrosion tests

Corrosion tests were conducted on the steel counterfaces and the WC-6 wt.% Co cemented carbide button in distilled water and synthetic mine water. Two tests were conducted per sample per environment to check the repeatability.

4.2.1 Corrosion of WC-6 wt.% Co buttons

The polarisation behavior of the WC-6 wt.% Co cemented carbides in distilled water and synthetic mine water is shown in Figure 4.39. The response of the cemented carbide in synthetic mine water is characterised by a lower potential and a higher current density compared to exposure in distilled water. This indicates that there is a higher tendency for the cemented carbide to corrode in synthetic mine water than in distilled water. The cemented carbide shows pseudo-passivation in synthetic mine water, interrupted by noise, which may be attributed to the chemical activity on the exposed surface and changes in the surface characteristics. Clear pseudo-passivation is seen in distilled water. Similar observations were made by Machio *et al* [40]. Table 4.14 presents the corrosion parameters for the cemented carbides tested in both solutions. Figure 4.40 illustrate the comparison of the cemented carbides buttons in the two solutions. The variation in corrosion rates as indicated by the error bars may be due to changes in the surface characteristics during exposure. Table 4.14 shows that high corrosion current were experienced by WC-6 wt.% Co in synthetic mine water than in distilled water hence high corrosion rate due to the fact that corrosion current is directly proportional to corrosion rate.

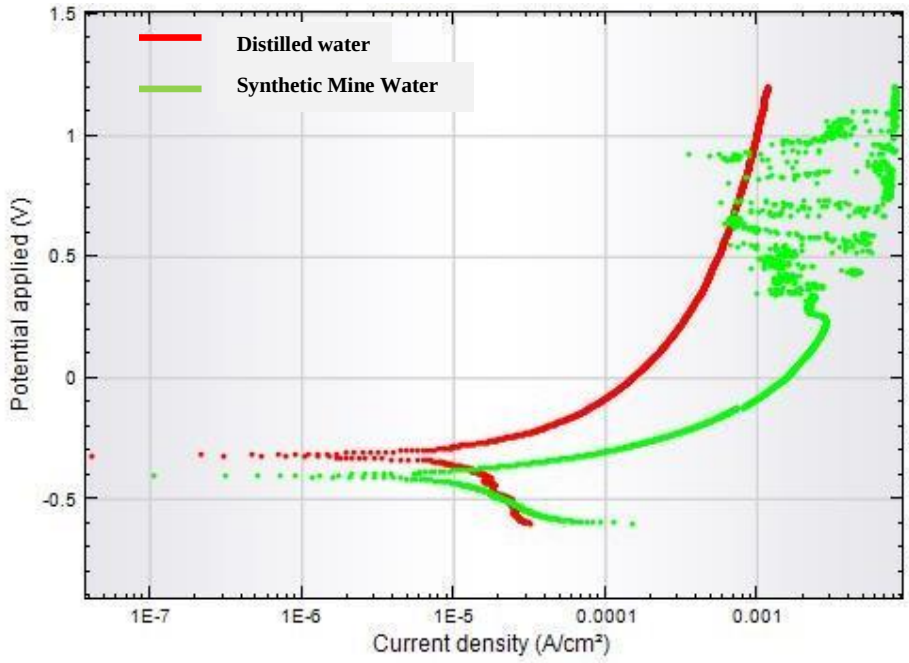


Figure 4. 39: Comparison of the potentiodynamic curves of the WC-6 wt.% Co buttons in distilled water and synthetic mine water.

Table 4. 14: Electrochemical corrosion parameters of the WC-6 wt.% Co buttons.

Environment	I_{corr} µA	E_{corr} mV	Corrosion rate (10^{-3})mmpy
Distilled water	2.05 ± 1.12	-0.359 ± 0.054	12.7 ±7.0
Synthetic mine water	3.42 ± 2.4	-0.416 ± 0.039	21 ±15

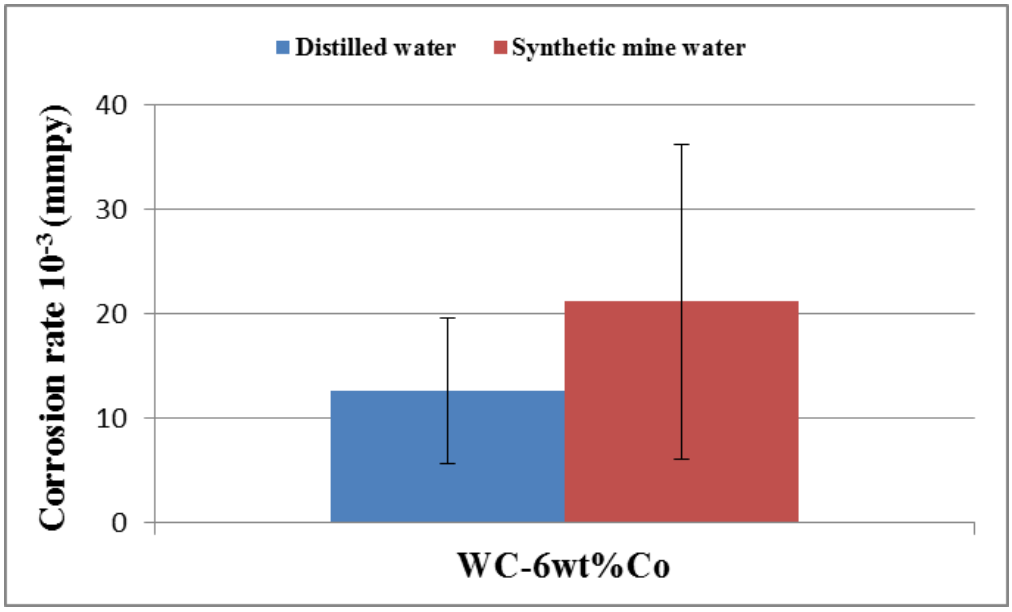


Figure 4. 40: Comparison of corrosion rates for the WC-6 wt.% Co buttons.

4.4.2 Corrosion of 3CR12 stainless steel

A comparison of the potentio-dynamic polarisation behavior of the 3CR12 stainless steel in the two solutions is shown in Figure 4.41. Both curves clearly show three regions namely: active, passive and trans-passive, which are typical for stainless steel [39]. A sharp trans-passive region was experienced in synthetic mine water which is associated with breaking of the passive layer due to the presence of chlorine and pits which were observed on the exposed surface. The polarisation curves of the 3CR12 stainless steel in synthetic mine water shows a lower potential (more negative) and high current density compared to when exposed to distilled water. When the 3CR12 stainless steel was exposed to distilled water, it exhibited a small active region and a large passive region whereas in synthetic mine water it showed the opposite trend. The more negative potential experienced in synthetic mine water indicate the higher tendency to corrode in this solution.

Table 4.15 gives a summary of the corrosion parameters while Figure 4.42 illustrates the comparison of the corrosion rates. Higher corrosion rates were experienced in synthetic mine water compared to distilled water and this is in agreement with the polarization curves.

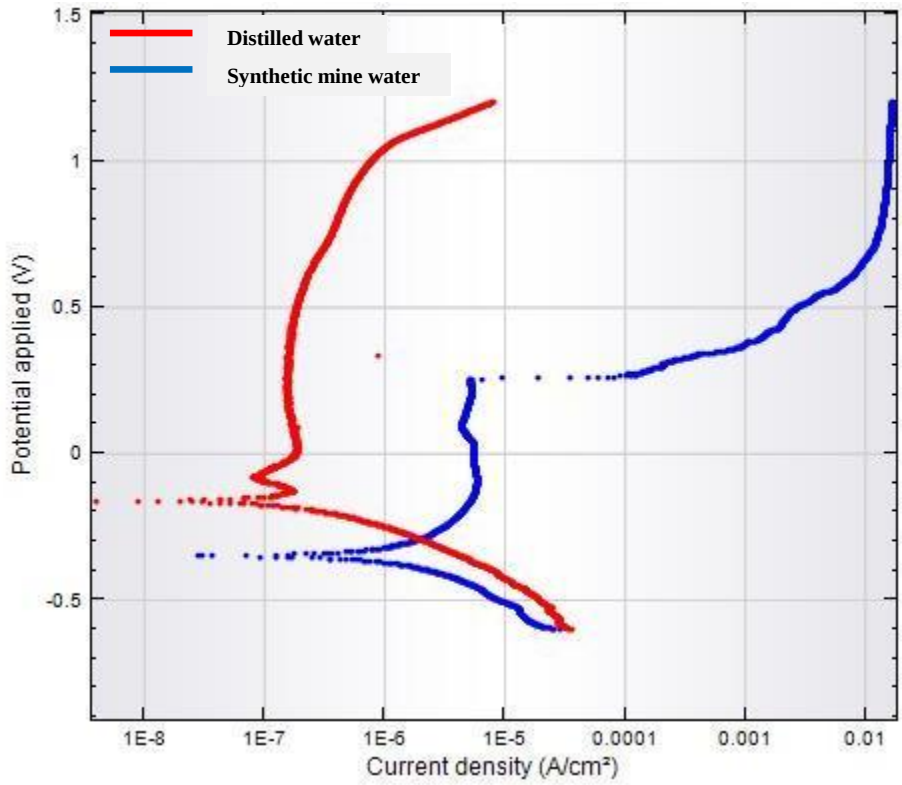


Figure 4. 41: Comparison of potentio-dynamic curves for 3CR12 stainless steel in distilled and synthetic mine water.

Table 4. 15: Electrochemical corrosion parameters for 3CR12 stainless steel.

Environment	I_{corr} nA	E_{corr} mV	Corrosion rate (10^{-3}) mmpy
Distilled water	18.63 ±14.4	-0.184 ± 0.032	0.61 ±0.41
Synthetic mine water	175.5 ±64.3	-0.358 ± 0.023	5.75 ±2.1

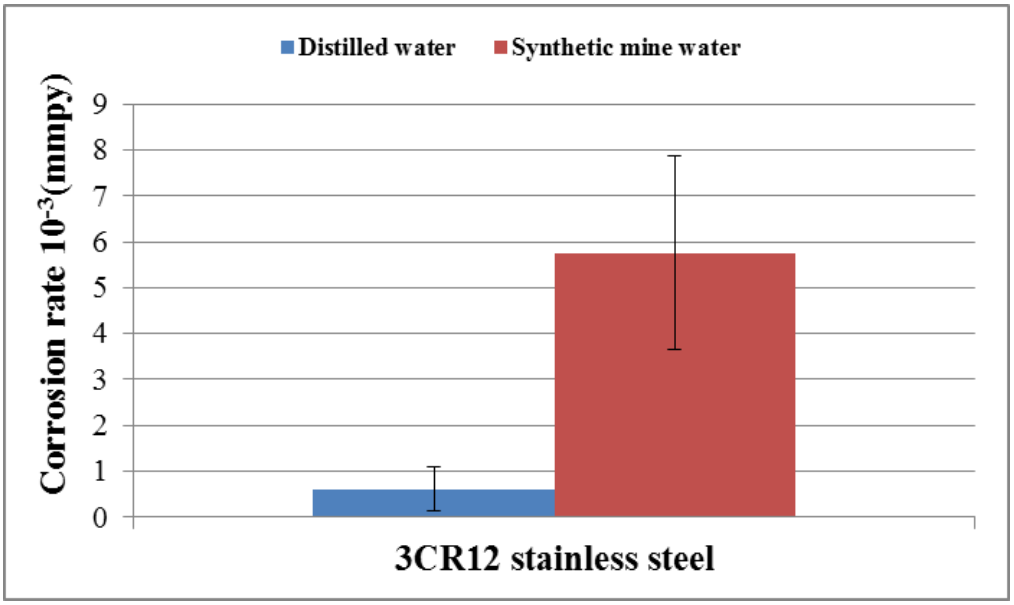


Figure 4. 42: Comparison of corrosion rates for 3CR12 stainless steel in distilled water and synthetic mine water.

4.4.3 Corrosion of mild steel

The polarisation behavior of mild steel in distilled water and synthetic mine water is illustrated in Figure 4.43. Both curves show active regions wherein the samples corrode as the applied potential gets increase. There is no passive region that can be identified. The response in synthetic mine water is characterised by a higher current density compared to distilled water, but the potential is relatively at the same level. Table 4.16 gives a summary of the corrosion parameters, where it can be seen that there is a higher corrosion rate in synthetic mine water than in distilled water. Figure 4.44 shows the comparison of the corrosion rates of mild steel when exposed to both solutions.

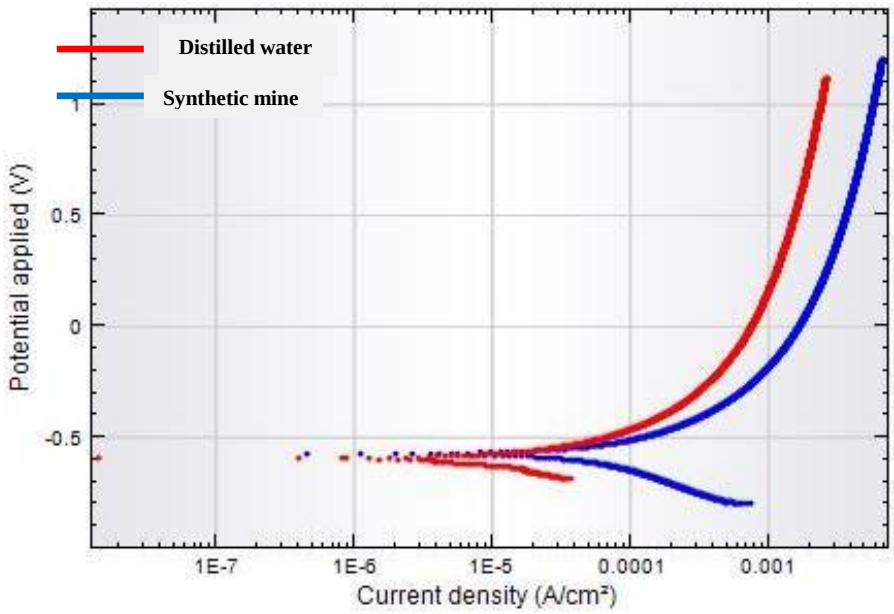


Figure 4. 43: Comparison of potentiodynamic curves of the mild steel in distilled and synthetic mine water.

Table 4. 16: Electrochemical corrosion parameters for mild steel.

Environment	I_{corr} µA	E_{corr} mV	Corrosion rate (10^{-3})mmpy
Distilled water	0.859	-0.6	30.2
Synthetic mine water	6.42	-0.562	225

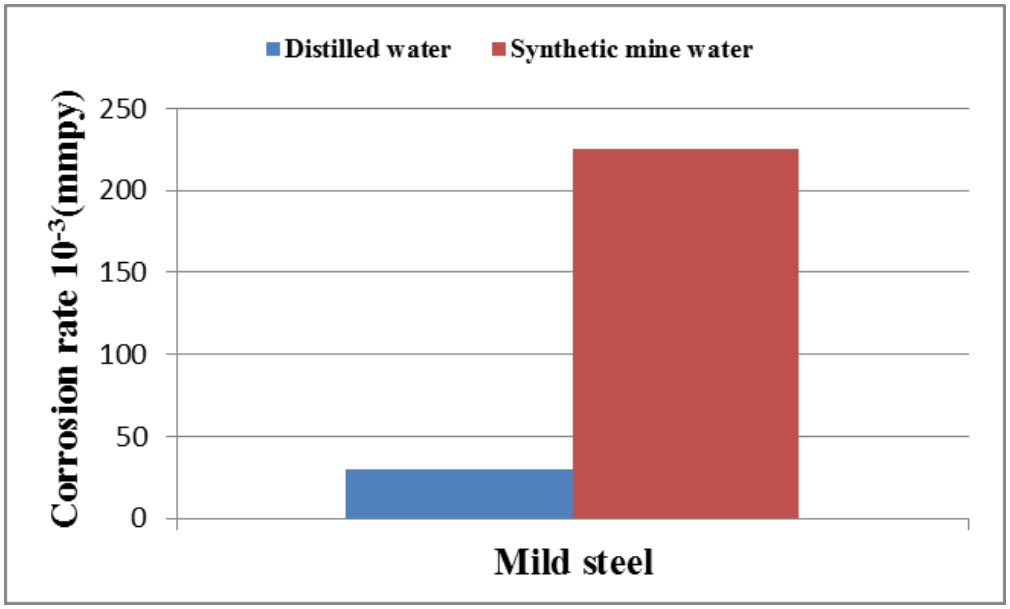


Figure 4. 44: Comparison of corrosion rates for the mild steel in distilled water and synthetic mine water.

4.4.4 Corrosion rates comparison of WC-6wt%Co buttons, mild steel and 3CR12 stainless steel

Figure 4.45 shows the comparison of corrosion rates of WC-6 wt.% Co buttons, mild steel and 3CR12 stainless steel in both distilled and synthetic mine water. The 3CR12 stainless steel showed better corrosion resistance when compared to mild and cemented carbide in both distilled and synthetic mine water. The corrosion rate of 3CR12 stainless steel in distilled water was 0.61 $x10^{-3}$ mmpy which was very small to appear in Figure 4.45. Mild steel showed highest tendency to corrode in both environments. Each material experienced an increase in corrosion as the environment changed from distilled to synthetic mine water which is an indication that synthetic mine water is an aggressive environment compared to distilled water.

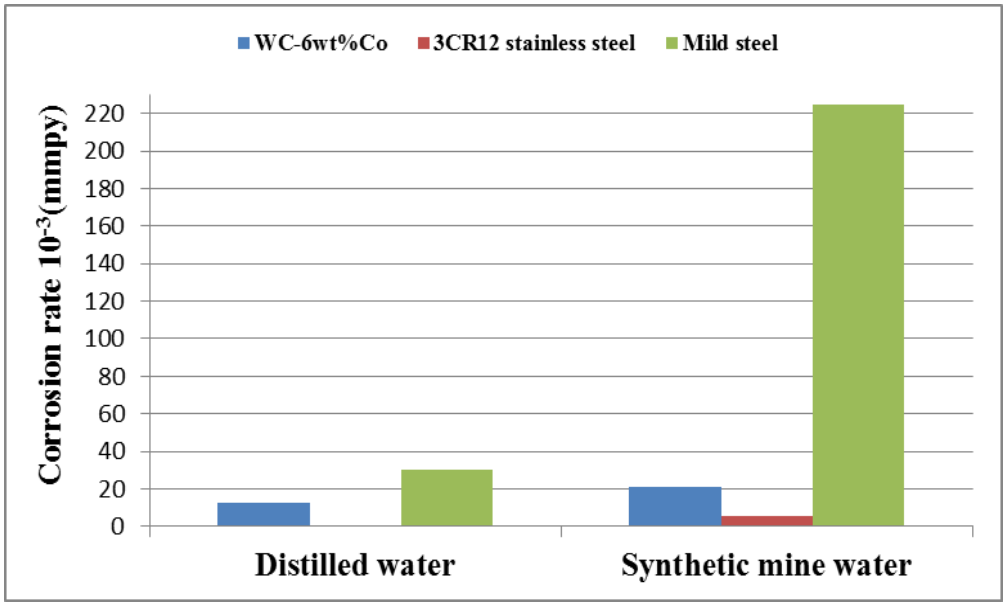


Figure 4. 45: Corrosion rates of all samples in distilled and synthetic mine water.

Chapter 5

Discussion

The aim of this project was to study the corrosive wear behaviour of WC-6 wt.% Co hardmetals in a mining environment. The reciprocating wear behaviour was determined by sliding the WC-6 wt. % Co against two industrial steels in a pin-on-flat configuration whereas the corrosion behaviour was determined in a standard potentio-dynamic corrosion setup. For both tests synthetic mine water was used to simulate the mining environment while distilled water was used as a control electrolyte.

5.1 Microstructural analysis

The microstructure of mild steel was a typical carbon steel structure consisting of ferrite and pearlite. The orientation of the grains indicated that this steel was rolled during production. The 3CR12 is ferritic stainless steel and the microstructure consisted of ferrite matrics and plates of martensite that were also aligned to one direction, as a result of rolling during manufacturing. The WC-6 wt.% Co button microstructure consisted of the typical angular tungsten carbide grains of various sizes, and the cobalt matrix between the tungsten carbide grains. The variation in size of tungsten carbide grains may be attributed to the size of powder particles used during production and the influence of the sintering process.

On the material properties, the WC-6 wt.% Co buttons showed a low level of porosity, as well as an acceptable density of 14.9 $g.cm^{-3}$ which is in the range of typical densities for this grade [1]. This gives an indication that the mixing and sintering process was efficient during the manufacturing process. The hardness of this material was about 7% below the typical hardness range for this grade (6 wt.% Co) [1]. This may be due to grain coarsening during manufacturing, and the grain distribution within the structure. The fracture toughness of the cemented carbide obtained is comparable with that obtained in the study conducted by Scieszka [41].

The XRD phase analyses of mild steel and 3CR12 stainless steel showed the typical constituents of these materials with no undesired phases which could negatively affect the properties. The same applied to the cemented carbide button; no detrimental phases

such eta (η) phase was detected; only WC and Co phases were present. Co showed its existence in crystalline form and this was confirmed by the XRD spectrum with no dome shape.

5.2 Corrosion behavior of the test materials

Corrosion can be explained in terms of electrochemical reactions. Potentio-dynamic anodic polarisation is the characterisation of a metal by its current and potential relationship. The specimen potential is scanned in the positive direction, acting as an anode thereby allowing it to corrode or to form an oxide coating. The measurements obtained are used to determine the corrosion characteristics of the metal involved [43].

5.2.1 Corrosion of WC-6 wt.% Co buttons

The polarization of the WC-6 wt.% Co cemented carbide in distilled and synthetic mine water is shown in Figure 4.39. The behaviour in distilled water shows an active region which increases with potential, without any sign of passivation, whereas pseudo-passivation is experience when exposed to synthetic mine water (which was interrupted by noise). Similar observations of pseudo-passivation behaviour in WC-6 wt.% Co cemented carbides were made by Machio *et al* [40]. The noise experienced was attributed to the change in surface characteristics, due to possible chemical reactions during the course of the test. The comparison of polarisation curves of the WC-6wt%Co cemented carbide in synthetic mine and distilled water showed that a lower potential and higher current density were experienced in synthetic mine water. The polarisation behavior together with Figure 4.40 and Table 4.14 gives an indication that there is higher tendency of WC-6 wt.% Co to corrode in synthetic mine water than in distilled water. It was interesting to note that corrosion occurred in distilled water; the reasoning for this is unclear. According to Faraday's law, the mass of primary products formed at an electrode is directly proportional to the quantity passed, therefore the greater the current density the higher the corrosion rate [37, 39]. The corrosion rate for the WC-6 wt.% Co buttons was found to be 40% higher in synthetic mine water than in distilled water, which was used as a control solution.

5.2.2 Corrosion of 3CR12 stainless steel

Stainless steels are generally well known for their resistance to corrosion. This is due to the formation of a thin passive layer which protects the metal from chemical attack in an oxidising environment [1]. The formation of this thin passive layer helps in maintaining low corrosion rates, and any break down of this film leads to localised corrosion, i.e. pits and crevices [39]. The polarisation behaviour of 3CR12 stainless steel in distilled water and synthetic mine water is illustrated in Figure 4.41. In both environments this material showed a typical polarisation curve which is characterised by active, passive and trans-passive regions. The exposure of 3CR12 stainless steel in distilled water showed a large passivation region compared to exposure in synthetic mine water. Small passivation region is attributed to the interruption of the passive region due to possible chemical reactions (film break down) in synthetic mine water. A sudden breakup of the passive region followed by an increase in current density at a relatively constant potential was experienced in synthetic mine water. This sudden breakup of the passive layer was possibly caused by pitting (see appendix H) due to the presence of chlorine atoms, which are well known for breaking the passive layer [44]. The Cl^- ions are small in size and enable penetration through passive oxide film and are aggressive enough to attack steel and initiate pits [44]. The higher tendency for corrosion in synthetic mine water was as a result of lower potential and high corrosion rate, due to the high corrosion density; this is confirmed by Table 4.15 and Figure 4.42. All the tests indicate that synthetic mine water is an aggressive environment when referenced to distilled water. The corrosion rate of the 3CR12 stainless steel was found to be 89 % higher in synthetic mine water than in distilled water.

5.2.3 Corrosion of mild steel

The polarisation behavior of mild steel in distilled and synthetic mine water is shown in Figure 4.43. Both polarisation curves show active regions wherein the samples corrode as the applied potential increases. There was no passive region that could be identified, and this is attributed to the fact that normal carbon steel has no tendency to form thin protective layers [37]. Instead when iron is exposed it is oxidized to Fe^{2+} and Fe^{3+} which are the corrosion products [37]. These polarisation curves for mild steel exposed in both environments shows that there is a higher current density experienced over the scanning potential, in synthetic mine water compared to distilled water. As mentioned

previously, a high current density leads to high corrosion rates as indicated in Figure 4.43 and Table 4.16.

5.2.4 Comparison of corrosion response of test materials

The effect of the corrosion environment on all the materials tested is shown by Figure 4.45. It can be seen that 3CR12 stainless steel showed the highest resistance to corrosion compared to both the cemented carbide and mild steel, despite the formation of pits. This is due to the ability of the 3CR12 stainless steel to form a thin oxide film which assists in the reducing corrosion rate. Mild steel showed poor resistance to corrosion in both environments when compared to the WC-6 wt.% Co cemented carbide and 3CR12 stainless steel, this is as result of mild steel being unable to form protective layer due to absence of alloying elements such as chromium. All samples showed an increase in corrosion rate when the environment was changed from distilled to synthetic mine water.

5.3 Reciprocating wear of the test materials

In the wear tests conducted, in each environmental condition (distilled water and synthetic mine water) three cemented carbide buttons were tested against three samples from each steel counterface. The summation of individual mass loss which was converted to volume loss using density according to Eq. 7 was conducted to obtain the average cumulative volume loss for each steel counterface. The average material volume loss for the WC-6 wt.% Co was determined by measuring the area of the wear scar. Examination of the wear scars was conducted to determine the wear mechanism of the different materials.

In general each material surface possesses a certain degree of asperities. These asperities form the initial contact points between two surfaces under static loading and they deform until the real contact area supports the load [32, 42]. Under relative sliding motion, adhesive wear or galling can occur by the shearing and deformation of asperities, followed by cold welding with the weaker material between the two yielding surfaces [32, 42]. Hardness is also used as an indirect measure of wear resistance, but the important hardness is said to be the one that is attained at the interface during

sliding [42]. These aspects are discussed in sections 5.3.1 which address the corrosive wear synergism between the tungsten carbide alloys and the steel counterfaces.

5.3.1 Reciprocating wear synergism between WC-6 wt.% Co and mild steel

Figure 4.10 and Figure 4.11 are the graphs of average volume loss for mild steel in distilled water and synthetic mine water respectively. An increase in the average volume loss was noted as a function of sliding distance, in both distilled water and synthetic mine water and this may be attributed to the variation in surface structure as sliding progressed. A consistently higher level of average material volume loss was seen on the mild steel samples exposed to synthetic mine water compared to distilled water; an indication of the aggressiveness of the synthetic mine water (see Figure 4.12). This high material volume loss was attributed to the possible chemical reactions that occurred while testing in synthetic mine water and the change in colour of the samples provided evidence of the possible occurrence of chemical reactions (see appendix E).

An initial decrease in the wear rate coefficient during the first 106 m of sliding, followed by a steady increase was noted in distilled water. In synthetic mine water the wear rate stabilized at a sliding distance of 150 m and remained steady for the remainder of the test. A decrease in dimensional wear coefficient may be attributed to the running-in phase at the beginning of the wear process. According to Hutchings [32] the running-in phase is a very complex stage of wear, and it can either increase or decrease as a result of possible work hardening, change in surface chemistry or plastic deformation of asperities [32].

The wear mechanism observed on the mild steel sliding against WC-6 wt.% Co was scratching, smearing and groove formation in distilled water, whereas severe plastic deformation followed by cold welding was observed in synthetic mine water, (Figure 4.27). Plastic deformation and shearing of the mild steel was due to its hardness which was about 87% lower than that of the WC-6 wt.% Co buttons. According to Hutching [32], the hardness ratio of the worn material to that of counter body is one of the critical parameters in wear applications. Generally when the hardness ratio stays below the critical value of 0.5 to 0.8, indentation will occur and these critical values have been found to form transition between mild and severe wear. When the hardness of the worn

material approaches that of the counter body the rate at which it wears reduces [32]. In this case the hardness ratio ($H_{Mild\text{-}steel}/H_{WC\text{-}Co}$) was 0.12 which is below the critical values; therefore the wear regime experienced by the mild steel is a severe form of wear. A wear depth of 0.29 mm was obtained in synthetic mine water compared to the 0.14 mm wear depth in distilled water (see appendix G), this supports the high volume loss experience by mild steel in synthetic mine water. It is quite evident that the change in environment had an influence on the wear and corrosion behaviour of both mild steel and WC-6 wt.% Co which is an indication of the synergistic effect between wear and corrosion.

5.3.2 Reciprocating wear synergism between WC-6 wt.% Co and 3CR12 stainless steel

Similar behaviour to that of mild steel was observed in the 3CR12 stainless steel, where there was an increase in the average material volume loss as a function of sliding distance in both distilled and synthetic mine water (Figures 4.16 and 4.17). The comparison as illustrated in Figure 4.18 showed that a higher average material volume loss was experienced in synthetic mine water than in distilled water, once again an indication of the aggressiveness of the mine water solution.

An increase in the dimensional wear coefficient occurred for the first 109 m in synthetic mine water followed by a steady decrease for the remainder of the test, whereas a steady decrease occurred in distilled water, which tended to stabilize as the sliding distance increased, (see Figures 4.19 and 4.20). The dimensional wear rate coefficient of 3CR12 stainless steel sliding against WC-6 wt.% Co was found to be 44% higher in synthetic mine water than in distilled water. A similar situation to mild steel was noted where the samples changed in colour in the vicinity of the wear track during the sliding test, which indicated the occurrence of a chemical reaction (see appendix E).

The wear scars of the 3CR12 stainless steel were given by Figure 4.33. Shearing and micro peeling of the surface material followed by cold welding was observed on the wear track. The severe damage which occurred in synthetic mine water is normally referred to as galling, which is a more severe form of adhesive wear [1, 42]. The galling phenomenon was caused by the yielding of stainless steel due to its mechanical

properties being lower than that of WC-6 wt.% Co i.e. the hardness ratio (H_{3CR12}/H_{WC-Co}) was 0.13 meaning that higher degree of indentation leading to higher wear rates was expected on 3CR12 stainless steel. Due to this ratio being lower that the critical values, the form of wear experienced was in severe region of the wear map. Pitting was observed on the 3CR12 stainless steel; pits can cause changes on the surface characteristics and raises the stress concentration factor which may lead to reduction in strength of the material [15, 39]. Once the strength of the material reduces, then the material becomes prone to high wear rates which is what 3CR12 stainless steel experienced. On the other hand 3CR12 stainless steel has a high work hardening rate and tendency to form martensitic structure during sliding; this structure is hard, brittle and has high tensile residual stresses which are bad for wear applications [1]. As it was seen in mild steel, the wear rates on 3CR12 stainless steel increased as the solution was changed, with wear depth of 0.10 mm in distilled water and 0.376 mm in synthetic mine water (see appendix G). The change in severity of damage and wear rates as the solution was changed to synthetic mine water also gave an indication on the synergistic effect between corrosion and wear.

5.3.3 Comparison of the corrosive wear synergisms of the WC-6 wt.% Co buttons sliding against mild steel and 304L stainless steel

The average material volume loss of the WC-6 wt.% Co buttons was estimated by measuring wear scar area generated by the sliding action between the buttons and the steel counterfaces. Variation in contact area was noted during the test hence the average material volume loss. Comparison of the sliding pairs in a reference solution (distilled water) and synthetic mine was done. It was noted that there was a slight difference in wear behaviour of the WC-6 wt.% Co buttons when sliding against mild steel counterface in distilled water than 3CR12 stainless steel. The dimensional wear rate coefficient indicated that there was about 0.4% difference in the wear behaviour of these buttons against both counterfaces in distilled water.

When the environment was changed to synthetic mine water, the average material volume loss of the WC-6 wt.% Co increased in both sliding pairs (Figure 4.23). The highest average material volume loss was observed in a WC-6 wt.% Co/3CR12 stainless steel sliding pair than in a WC-6 wt.% Co/mild steel sliding pair. This may be

attributed to the high work hardening rate possessed by the 3CR12 stainless steel as well as the change in environment. The 3CR12 stainless steel has high work hardening rate than mild steel due to tendency to form hard martensite at the surface [1]. The work hardened 3CR12 stainless steel surface made it difficult for the buttons to indent the surface hence caused the buttons to experience wear. This change in wear behaviour of the WC-6 wt.% Co/3CR12 stainless steel sliding pair supports the theory that, wear is not an intrinsic material property but a system property [8], meaning that any change in parameter within the system will bring change the wear behaviour.

The dimensional and dimensionless wear coefficients showed that the WC-6 wt.% Co/3CR12 stainless steel sliding pair in synthetic mine water was 52% severe than WC-6 wt.% Co/mild steel sliding pair (see Figure 4.24 and Table 5.1). This behaviour was influenced by the change in surface characteristics of the materials due to sliding and the corrosion response of these material in synthetic mine water.

Table 5. 1: Wear coefficients for the sliding pairs in synthetic mine water.

Sliding pair	Wear coefficients	
	k 10^{-6} (mm^3/N.m)	K (10^{-4})
WC-6 wt.% Co/mild steel	8.74	1.14
WC-6 wt.% Co/3CR12 stainless steel	18.3	2.39

Large wear scar contact area was seen when sliding buttons against 3CR12 stainless steel than mild steel. This was due to the formation wider wear track as a result of extensive material yielding on the 3CR12 stainless steel, similar behaviour was noted in the study done by van der Merwe [45]. This resulted in low contact stresses when compared to that of mild steel (see appendix D), however high wear rates were experienced by these button when in a 3CR12 stainless steel sliding pair. Though stainless steel had higher hardness than mild steel, it experienced higher wear rates in both solutions due to its hardening effect and possible change in microstructure from austenitic to martensitic.

All cemented carbide buttons sliding against both steel counterface exhibited similar wear mechanism. The Co binder is a ductile matrix; therefore it plastically deformed and got smeared off as a result of the shear stresses generated by the steel counterface during sliding. Due to binder matrix removal, WC grains remained unsupported and

exposed to the contact stresses. High contact stresses gets generated between exposed WC and counterface material as sliding process progresses and this resulted in micro cracking and breaking of WC grains, see Figures 4.31 and 4.37. The presence of the counterface constituents was detected by the EDS analysis on the buttons wear scars. This is an indication of the material transfer from the steel counter faces to the WC-6 wt.% Co buttons during wear. The transfer of material from one material to the other during wear is described as adhesion due to the yielding followed by plastic deformation as a result of hardness difference between both steel counterfaces (87 - 88 % lower) and WC-6 wt.% Co.

5.4 Experimental testing error

In corrosion testing, the determination of the Tafel plots by drawing the tangent lines on the polarisation curve is subjective. It is subjected to human error and may have an influence in terms of the standard deviation on the results obtained.

In the wear testing rig, loading must be symmetric around the axis, and any misalignment may induce vibration on the loading lever which may influence the experimental set-up in terms of wear tracks which will be formed. The wear track provides important information to determine the wear mechanism. It is also critical that the counterface (steel) and the pin (carbide) are properly secured into their housing; as any movement will influence the results.

Chapter 6

Conclusions

The main conclusions drawn from the research are listed below:

- The microstructural characterization showed that the WC-6 wt.% Co had typical angular WC grains with cobalt as the matrix. The grain size was Type 6-M according to ASTM B390-92. No detrimental phases, which could compromise the properties of the WC-6 wt.% Co buttons, were detected; density and fracture toughness were within a range of the typical 6 wt.% Co grade except for hardness which was about 7% lower.

- The corrosion behavior of WC-6 wt.% Co, as referenced to distilled water, was found to be 40% higher in synthetic mine water. Pseudo passivation was also noted in synthetic mine water.

- A higher average material volume loss was experienced by the WC-6 wt.% Co in the WC-6 wt.% Co/3CR12 stainless steel sliding pair compared to the WC-6 wt.% Co/mild steel sliding pair in synthetic mine water, this was possibly due to relatively high initial hardness and increased transitional hardness of 3CR12 stainless steel during sliding. The dimensional wear rate coefficient of the WC-6 wt.% Co in synthetic mine water was found to be 52 % higher in the first sliding system. Both the counterfaces and the buttons showed a change in color which was an indication of the chemical reactions during sliding.

- The wear mechanism of the mild steel was characterized by plastic deformation and grooving caused by ploughing. The wear mechanism of the 3CR12 stainless steel was plastic deformation, groove formation and galling, which is a severe form of adhesive wear. The cemented carbide buttons showed the typical wear mechanisms characterized by removal of the ductile Co binder, followed by micro-cracking of exposed WC grains. Material transfer of the steel counterfaces onto the WC-6 wt.% Co buttons was confirmed by EDS analysis.

- The influence in wear and corrosion behaviour of the WC-6 wt.% Co was noted as the solution was changed from distilled to synthetic mine indicating the

synergistic effect, meaning that the combined effect of corrosion and wear will be detrimental and reduce the life of the WC-6 wt.% Co.

Chapter 7

Future studies

- The current research was based on two steel as counterfaces. Different materials with relatively higher hardness can be used to study further the effect of change in hardness of the counterfaces on the reciprocating wear behavior of cemented carbide buttons.
- Monitoring of friction as the sliding distance increases can be beneficial. This can be used to verify the relationship between surface friction and wear.
- Comparative studies using different grades of cemented carbides should be done to determine which grades have the best corrosive wear resistance.
- The XPS (or similar) technique should be employed to quantify the oxidation and corrosion mechanisms on both the wear scars and corroded surfaces.
- Investigating the changes in the wear test parameters such as sliding distance, reciprocating frequency and applied loading would provide further information on the corrosive wear synergism.

References

[1] P.J. Blau, *Friction, lubrication and wear technology*, ASM International, USA, Vol. 18, pp. 337-1677, 1992.

[2] E.M. Trent, P.K. Wright, *Metal Cutting*, 4th ed., Butterworth-Heinemann, Boston, pp. 175-185, 2000.

[3] J.W. Pridgeon, E.L. Langer, *Metallography and microstructure*, ASM Internationals, Ohio, Vol. 9, pp. 513-527, 1985.

[4]] E. Lassner, W.D. Schubert, *Tungsten: properties, chemistry, technology of the elements, alloys and chemical compounds*, Plenum Publishers, New York, pp. 321-353, 1999.

[5] G.S. Upadhyaya, *Cemented tungsten carbide: properties and testing*, Noyes Publications, New Jersey, pp. 243-244, 1998.

[6] R.G. Bayer, *Engineering design for wear*, 2nd ed., Marcel Dekker, New York, pp. 2-4, 2004.

[7] J Finger, D Blankenship, *Handbook of best practices in geothermal drilling*, Sandia national laboratory, New Mexico, pp 38-42, 2010.

[8] W.A. Glaeser, D.A. Rigney, *Source book on wear control technology*, 1st ed., American Society of Metals, Ohio, pp *1-2,271-276,* 1978.

[9] A. From, A *wear test mimicking the tribological situation in rock drilling*, Diploma Thesis, Uppsala University, pp 5-36, 2012.

[10] P.H. Shipway, J.J. Hogg, *Dependence of micro-scale abrasion mechanism of WC-Co hard metals on abrasive type*, Wear, Vol. 259, pp. 44–51, 2005.

[11] K. Bony, P. De Baets, J. Vleugels, S. Huang, O. Van der Biest, B. Lauwers, *Impact of Cr_3C_2/VC addition on the dry sliding friction and wear response of WC–Co cemented carbides*, Wear, Vol. 267, pp. 1642–1652, 2009.

[12] P.J. Juhani, K. Viljus, M. Letunovitš, *Two-body abrasive wear of WC-Co hard-metals in wet and dry environments*, Proc. 8th International conference DAAAM Baltic Industrial Engineering, Estonia, Ed. T. Otto, pp. 621-626, 2012.

[13] X. Ren, H. Miao, Z. Peng, *A review of cemented carbides for rock drilling: An old but still tough challenge in geo-engineering*, Int. Journal of Refractory Metals and Hard Materials, Vol. 39, pp. 61-77, 2013.

[14] P.H. Shipway, L. Howell, *Micro-scale abrasion-corrosion behavior of WC-Co hard metals and HVOF sprayed coatings*, Wear, Vol. 258, pp. 303-312, 2005.

[15] www.kennametal.com.

[16] P.C. Angelo, R. Subramanian, *Powder metallurgy: Science, technology and applications*, PHI learning Private Limited, New Delhi, pp. 196-203, 2008.

[17] http://www.generalcarbide.com/designers-guide.

[18] D.G.F. O'Quigley, S. Luyckx, M.N. James, *An empirical ranking of a wide range of WC-Co grades in terms of their abrasion resistance measured by ASTM standard B611-85 test*, International Journal of Refractory Metals and Hard Materials, Vol. 15, pp.73-79, 1997.

[19] S.D. Creamer, B.S. Covino, Jr, *Corrosion: Materials*, ASM International, Materials Park Ohio, Vol. 13B, pp. 513-524, 2005.

[20] S.F. Krar, A.R. Gill, *Exploring advanced manufacturing technologies*, 1st ed., Industrial Press Inc., New York, pp. 930, 2003.

[21] http://www.dcu.ie/sites/default/files/mechanical_engineering/pdfs/manuals/DensityDeterminationManual.pdf.

[22] http://www.hardmaterials.sandvik.com/sandvik/0130/HI/SE03411.nsf/7a5364adb7735b05412568c70034ea1b/651f6e334db04c46c125707600562c88/$FILE/Cemented%20Carbide.pdf.

[23] J. Gurland, *Microstructural aspects of the strength and hardness of cemented tungsten Carbide*, Brown University, pp. 1-16, 1969.

[24] S.I Cha, S.H. Hong, G.H. Ha, B.K. Kim, *Mechanical properties of WC-10%Co cemented carbides sintered from nano crystalline spray convention processed powder*, International Journal of Refractory Metals and Hard Materials, Vol.19, pp. 397-403, 2001.

[25] D.R. Askalend**,** *The Science and engineering of materials*, 3rd ed., Nelson Thomes Ltd, United Kingdom, pp. 776, 1998.

[26] N. Sacks, *The wear and corrosive wear response of tungsten carbide-cobalt hard metals under wood cutting and three body abrasion condition*, Ph.D. Thesis, University of Erlangen-Nurnberg, pp. 56, 2002.

[27] H.E. Exner, *The influence of sample preparation on the surface stress state and Palmqvist's method for toughness testing of cemented carbides*, Brown University, pp. 1-20, 1968.

[28] D.K Shetty, I.G Wright, P.N Mincer, A.H Clauer, *Indentation fracture of WC-Co cermets*, Journal of Material Science, Vol. 20, pp.1873-1892, 1985.

[29] R Spiegler, S Schmadder , L.S. Sigl, *Fracture toughness evaluation of WC-Co alloys by indentation testing*, Journal of Hard Materials, Vol.1 , pp. 147-158, 1990.

[30] MJ Neale and M Gee, *A guide to wear problems and testing for industries*, Professional Engineering Publishing Limited, United Kingdom, pp. 3-40, 110, 2000.

[31] Y. Qiao, Y.R. Liu, T.E. Fischer, *Sliding and abrasive wear resistance of thermal-sprayed WC-Co coatings*, Journal of Thermal Spray Technology, Vo. 10(1), pp.118-125, 2001.

[32] I.M. Hutchings, *Tribology: friction and wear of engineering materials*, Edward Arnold, UK, pp. 77, 1992.

[33] A. Abdelbary, M.N. Abouelwafa, I.M El Fahham, A.I Gomaa, *A new reciprocating tribometer for wear testing under different fluctuating loading conditions*, AEJ-Alexandrian Engineering Journal, Vol 43, pp.615-619.

[34] S. Luyckx, A. Love, *The relationship between the abrasion resistance and the hardness of WC-Co alloys*, The Journal of the South African Institute of Mining and Metallurgy, Vol. 104(10), pp. 579-582, 2004.

[35] J. Pirso, Sergei Letunovitš, M. Viljus, *Friction and wear behaviour of cemented carbides*, Elsevier, Wear, Vol. 257, pp. 257–265, 2004.

[36] K. Bonny, P. De Baets, J. Vleugels, S. Huang, B. Lauwers, *Dry Reciprocating Sliding Friction and Wear Response of WC–Ni Cemented Carbides*, Tribology Letter 31, pp. 199–209, 2008.

[37] Z. Ahmad, *Principles of corrosion engineering and corrosion control*, 1st ed., Elsevier Science and Technology, 2006.

[38] P.A. Schweitzer, *Fundamentals of corrosion: mechanism, causes and preventative methods*, CRC Press, Boca Raton Florida, pp. 14-25 ,2010.

[39] R.W. Revie and H.H. Uhling, *Corrosion and corrosion control: an introduction to corrosion science and engineering*, 4th ed, A John Wiley & Sons Inc. Publications, Hoboken New Jersey, pp. 419, 2008.

[40] C.N. Machio, D.S. Konadu, J.H. Potgieter, S. Potgieter-Vermaak, J. van der Merwe, *Corrosion of WC-VC-Co hardmetal in neutral chloride containing media*, Hindawi Publishing Corporation, pp. 2-9, 2013.

[41] S.F. Scieszka, *The wear transition as means for hardmetal fracture toughness evaluation*, International Journal of Refractory Metals and Hard Materials, 19, pp. 101-108, 2001.

[42] *Review of the wear and galling characteristics of stainless steel*, American Iron and Steel Institute, Washington D.C, pp. 2- 27, 1978.

[43] "*Basics of corrosion measurements*" Application notes corr-1, EG&G Princeton Applied Research, Princeton, NJ, 1980.

[44] R.T Loto, *Pitting corrosion of austenitic stainless steel type 304 in acidic chloride media*, Journals of Materials and Environmental Science, Vol. 4(4), pp. 448-459, 2013.

[45] R. van der Merwe, *Friction and sliding wear of wc-co inserts containing mixed carbides (tic, tac, nbc)*, Masters Thesis, University of the Witwatersrand, pp 77-87, 2011.

Appendix A: Hardness test data

Appendix A provides the hardness test data that was used to calculate the average hardness of the materials. No formula was used since the hardness machine automatically calculates the values after indentation. Tables A.1 and A.2 are the test data for the WC-6 wt.% Co cemented carbide buttons whereas Tables A.3 and A4 are for mild steel and 3CR12 stainless steel respectively. In the tables below, d1 and d2 represents the diagonals of the indentation.

Table A. 1: Vickers hardness test data for WC-6 wt.% Co sample 1.

Indent	d1(µm)	d2(µm)	HV_{30}
1	204.3	203.7	1336.8
2	202.5	203.8	1348
3	202.9	205.5	1334.2
4	202.7	205.3	1334.8
5	200.2	204.4	1361.4
Average hardness			1343.04
Standard deviation			11.69

Table A. 2: Vickers hardness test data for WC-6 wt.% Co sample 2.

Indent	d1(µm)	d2(µm)	HV_{30}
1	204.2	206.2	1321.2
2	205.9	207.4	1302.7
3	204.4	207.2	1313.5
4	204.1	205.4	1327
5	206.1	204.9	1317.3
Average hardness			1316.34
Standard deviation			9.114439

Table A. 3: Vickers hardness test data for mild steel.

Indent	d1(µm)	d2(µm)	HV_{30}
1	595.5	597.1	156.5
2	595.1	604	154.8
3	603.6	594.9	154.9
4	596.1	598.2	156
5	594.4	597.4	156.7
Average			156
standard deviation			0.88713

Table A. 4: Vickers hardness test data for 3CR12 stainless steel.

Indent	d1(µm)	d2(µm)	HV_{30}
1	575.1	556.5	173.8
2	577.5	565.4	170.4
3	582.8	551.8	172.9
4	579.9	561.9	170.7
5	582.7	563.5	169.4
Average			171
Standard deviation			1.836573

Appendix B: Fracture toughness data

As indicated in section 3.1.4 Eq. 3, the Palmqvist technique using Shetty formula was utilised determining fracture toughness. Table B.1 and B.2 shows the test results and calculations done whereas Figure B.1 indicate the Palmqvist method.

Table B. 1: Fracture toughness data for WC-6 wt.% Co buttons.

SAMPLE 1									
Crack 1 (µm)	**Crack 2 (µm)**	**Crack 3 (µm)**	**Crack 4 (µm)**	**Σ Cracks (µm)**	**HV_{30}**	**Hardness (GPa)**	**K_{IC} ($MPa.m^{1/2}$)**	**$K_{IC(AV)}$**	**Standard deviation**
25.823	41.371	23.101	53.437	143.732	1336.8	13.114	14.6	14.6	1.01
70.999	17.05	44.744	14.142	146.935	1348	13.224	14.5		
26.311	12.263	27.47	66.545	132.589	1334.2	13.089	15.2		
42.148	34.034	16.93	18.222	111.334	1334.8	13.094	16.5		
50.71	15.347	41.244	28.124	135.425	1361.4	13.355	15.1		
SAMPLE 2									
Crack 1 (µm)	**Crack 2 (µm)**	**Crack 3 (µm)**	**Crack 4 (µm)**	**Σ Cracks (µm)**	**HV_{30}**	**Hardness (Pa)**	**K_{IC} ($MPa.m^{1/2}$)**		
42.282	47.938	45.544	37.012	172.776	1321.2	12.961	13.2		
60.371	12.715	23.642	39.735	136.463	1302.7	12.779	14.8		
41.689	29.293	38.901	47.337	157.22	1313.5	12.885	13.8		
45.761	20.031	45.135	54.357	165.284	1317.3	12.923	13.5		

Appendix C: Density and porosity data

The density of the WC-6 wt.% Co was determined using Archimedes' principle whereas the density of the counterfaces was done by measuring the weight and volume of the samples.

Table C. 1: Density data for the WC-6 wt.% Co buttons.

Suspended weight (g)	**Wet weight(g)**	**Dry weight(g)**	**Density (g/cm^3)**	**Open porosity**
10.524	11.2793	11.279	14.93314	0.039719
10.5239	11.2798	11.279	14.92129	0.105834
10.523	11.2799	11.279	14.90157	0.118906
10.5237	11.2801	11.279	14.91142	0.145426
10.5235	11.2802	11.279	14.90551	0.158583
Average density			14.91459	0.113694
Standard deviation			0.012756	0.046323

Table C. 2: Density data for the mild steel.

Mass (g)	**Volume (cm^3)**	**Density (g/cm^3)**
65.762	8.4	7.829
65.121	8.4	7.753
64.989	8.4	7.737
65.214	8.4	7.764
65.56	8.4	7.805
65.61	8.4	7.811
Average density		7.783
Standard deviation		0.037

Table C. 3: Density data for the 3CR12 stainless steel.

Mass (g)	**Volume (cm^3)**	**Density (g/cm^3)**
64.506	8.4	7.679
64.325	8.4	7.658
64.535	8.4	7.683
64.518	8.4	7.681
64.503	8.4	7.679
64.426	8.4	7.670
Average density		7.675
Standard deviation		0.010

Appendix D: Reciprocating wear data

This appendix provides the test data used to calculate average material volume loss and wear rate coefficient for the materials. Table D.1, D.4, D.7 and D.10 are the mass loss data of the mild steel and 3CR12 stainless steel in distilled water and synthetic mine water. Tables D.2, D.5, D8 and D.11 are the volume loss data for the two steel counterfaces in the two solutions. Table D.3, D.6, D.9 and D.12 are the wear rate coefficient data for both materials in the two solutions. Tables D13 to D16 list the wear coefficient data of the WC-6 wt.% Co buttons sliding against the two steel counterfaces in the two solutions.

Table D. 1: Mass loss data for the mild steel sliding against WC-6 wt.% Co in distilled water.

Sample 1			**Sample 2**			**Sample 3**			Average Cumulative mass loss (g)
Mass (g)	Mass loss (g)	Cumulative mass loss (g)	Mass (g)	Mass loss (g)	Cumulative mass loss	Mass (g)	Mass loss (g)	cumulative mass loss (g)	
65.762	0	0	65.121	0	0	64.989	0	0	0
65.746	0.016	0.016	65.111	0.01	0.01	64.981	0.008	0.008	0.011
65.738	0.008	0.024	65.1	0.011	0.021	64.975	0.006	0.014	0.020
65.73	0.008	0.032	65.082	0.018	0.039	64.968	0.007	0.021	0.031
65.721	0.009	0.041	65.068	0.014	0.053	64.958	0.01	0.031	0.042
65.705	0.016	0.057	65.055	0.013	0.066	64.946	0.012	0.043	0.055
65.695	0.01	0.067	65.038	0.017	0.083	64.934	0.012	0.055	0.068

Table D. 2: Volume loss data for the mild steel sliding against WC-6 wt.% Co in distilled water.

Sliding distance (m)	**Sample 1** Volume removed (mm^3)	**Sample 2** Volume removed (mm^3)	**Sample 3** Volume removed (mm^3)	Average volume removed (mm^3)	Standard deviation
53.235	2.044	1.290	1.034	1.456	0.525
106.496	3.066	2.709	1.810	2.528	0.647
159.744	4.087	5.031	2.714	3.944	1.165
212.992	5.237	6.837	4.007	5.360	1.419
266.24	7.281	8.513	5.558	7.117	1.485
319.488	8.558	10.706	7.109	8.791	1.810

Table D. 3: Wear rate coefficient data for the mild steel sliding against WC-6 wt.% Co in distilled water.

Sliding distance (m)	**Sample 1** k (mm^3/N.m)	**Sample 2** k (mm^3/N.m)	**Sample 3** k (mm^3/N.m)	Average k (mm^3/N.m)	Standard deviation
53.235	0.000180	0.00011	9.12E-05	0.0001	4.6E-05
106.496	0.000135	0.00012	7.98E-05	0.00011	2.9E-05
159.744	0.000120	0.00015	7.98E-05	0.00012	3.4E-05
212.992	0.000115	0.00015	8.83E-05	0.00012	3.1E-05
266.24	0.000128	0.00015	9.80E-05	0.00013	2.6E-05
319.488	0.000126	0.00016	1.04E-04	0.00013	2.7E-05

Table D. 4: Mass loss data for the mild steel sliding against WC-6 wt.% Co in synthetic mine water.

Sample 1			**Sample 2**			**Sample 3**			Average Cumulative Mass loss (g)
Mass (g)	Mass loss (g)	Cumulative mass loss (g)	Mass (g)	Mass loss (g)	Cumulative mass loss (g)	Mass (g)	Mass loss (g)	cumulative mass loss (g)	
65.214	0	0	65.56	0	0	65.61	0	0	0
65.194	0.02	0.02	65.539	0.021	0.021	65.592	0.018	0.018	0.0197
65.185	0.009	0.029	65.525	0.014	0.035	65.581	0.011	0.029	0.031
65.172	0.013	0.042	65.513	0.012	0.047	65.57	0.011	0.04	0.043
65.158	0.014	0.056	65.499	0.014	0.061	65.555	0.015	0.055	0.0573
65.144	0.014	0.07	65.481	0.018	0.079	65.541	0.014	0.069	0.0727
65.128	0.016	0.086	65.469	0.012	0.091	65.523	0.018	0.087	0.088

Table D. 5: Volume loss data for the mild steel sliding against WC-6 wt.% Co in synthetic mine water.

Sliding distance (m)	**Sample 1** Volume removed (mm^3)	**Sample 2** Volume removed (mm^3)	**Sample 3** Volume removed (mm^3)	Average volume removed (mm^3)	Standard deviation
53.248	2.576	2.691	2.305	2.524	0.198
106.498	3.735	4.484	3.713	3.978	0.439
159.744	5.410	6.022	5.121	5.518	0.460
212.992	7.213	7.816	7.042	7.357	0.407
266.24	9.016	10.122	8.834	9.324	0.697
319.488	11.077	11.660	11.139	11.292	0.320

Table D. 6: Wear rate coefficient data for the mild steel sliding against WC-6 wt.% Co in synthetic mine water.

Sliding distance (m)	**Sample 1**	**Sample 2**	**Sample 3**	Average k (mm^3/N.m)	Standard deviation
	k (mm^3/N.m)	k (mm^3/N.m)	k (mm^3/N.m)		
53.248	0.000227	0.00024	0.000203	0.00022	1.7E-05
106.496	0.000165	0.0002	0.000164	0.00018	1.9E-05
159.744	0.000159	0.00018	0.000151	0.00016	1.4E-05
212.992	0.000159	0.00017	0.000155	0.00016	9E-06
266.24	0.000159	0.00018	0.000156	0.00016	1.2E-05
319.488	0.000163	0.00017	0.000164	0.00017	4.7E-06

Table D. 7: Mass loss data for the 3CR12 stainless steel sliding against WC-6 wt.% Co in distilled water.

Sample 1			**Sample 2**			**Sample 3**			Average Cumulative Mass loss (g)
Mass (g)	Mass loss (g)	Cumulative mass loss (g)	Mass (g)	Mass loss (g)	Cumulative mass loss (g)	Mass (g)	Mass loss (g)	cumulative mass loss (g)	
64.506	0	0	64.325	0	0	64.535	0	0	0
64.469	0.037	0.037	64.284	0.041	0.041	64.495	0.04	0.04	0.039333
64.442	0.027	0.064	64.244	0.04	0.081	64.456	0.039	0.079	0.074667
64.418	0.024	0.088	64.21	0.034	0.115	64.418	0.038	0.117	0.106667
64.389	0.029	0.117	64.189	0.021	0.136	64.383	0.035	0.152	0.135
64.358	0.031	0.148	64.156	0.033	0.169	64.353	0.03	0.182	0.166333
64.326	0.032	0.18	64.128	0.028	0.197	64.327	0.026	0.208	0.195

Table D. 8: Volume loss data for the 3CR12 stainless steel sliding against WC-6 wt.% Co in distilled water.

Sliding distance (m)	**Sample 1**	**Sample 2**	**Sample 3**	Average Volume removed (mm^3)	Standard deviation
	Volume removed (mm^3)	Volume removed (mm^3)	Volume removed (mm^3)		
53.24	4.818	5.354	5.213	5.128	0.278
106.488	8.334	10.578	10.296	9.736	1.222
159.736	11.459	15.017	15.248	13.908	2.124
212.992	15.236	17.760	19.809	17.602	2.291
266.24	19.273	22.069	23.719	21.687	2.248
319.488	23.440	25.726	27.107	25.424	1.852

Table D. 9: Wear rate coefficient data for the 3CR12 stainless steel sliding against WC-6 wt.% Co in distilled water.

Sliding distance (m)	**Sample 1**	**Sample 2**	**Sample 3**	Average k (mm^3/N.m)	Standard deviation
	k (mm^3/N.m)	k (mm^3/N.m)	k (mm^3/N.m)		
53.24	0.0004249	0.0004721	0.0004597	0.0004522	2.449E-05
106.488	0.0003674	0.0004663	0.0004539	0.0004292	5.388E-05
159.736	0.0003368	0.0004414	0.0004482	0.0004088	6.242E-05
212.992	0.0003358	0.0003915	0.0004367	0.000388	5.05E-05
266.24	0.0003399	0.0003892	0.0004183	0.0003824	3.963E-05
319.488	0.0003445	0.000378	0.0003983	0.0003736	2.722E-05

Table D. 10: Mass loss data for the 3CR12 stainless steel sliding against WC-6 wt.% Co in synthetic mine water.

Sample 1			**Sample 2**			**Sample 3**			Average Cumulative mass Loss
Mass (g)	Mass loss (g)	Cumulative mass loss (g)	Mass (g)	Mass loss (g)	Cumulative mass loss (g)	Mass (g)	Mass loss (g)	cumulative mass loss (g)	
64.518	0	0	64.503	0	0	64.426	0	0	0
64.448	0.07	0.07	64.449	0.054	0.054	64.364	0.062	0.062	0.062
64.38	0.068	0.138	64.363	0.086	0.14	64.299	0.065	0.127	0.135
64.314	0.066	0.204	64.312	0.051	0.191	64.234	0.065	0.192	0.195667
64.243	0.071	0.275	64.268	0.044	0.235	64.175	0.059	0.251	0.253667
64.194	0.049	0.324	64.229	0.039	0.274	64.115	0.06	0.311	0.303
64.146	0.048	0.372	64.184	0.045	0.319	64.066	0.049	0.36	0.350333

Table D. 11: Volume loss data for the 3CR12 stainless steel sliding against WC-6 wt.% Co in synthetic mine water.

Sliding distance (m)	**Sample 1**	**Sample 2**	**Sample 3**	Average Volume removed (mm^3)	Standard deviation
	Volume removed (mm^3)	Volume removed (mm^3)	Volume removed (mm^3)		
53.24	9.114	7.032	8.084	8.077	1.040
108.488	17.967	18.232	16.559	17.586	0.899
159.736	26.560	24.873	25.033	25.489	0.931
212.984	35.804	30.603	32.726	33.044	2.615
266.24	42.184	35.682	40.549	39.471	3.382
319.998	48.432995	41.542	46.938	45.638	3.625

Table D. 12: Wear rate coefficient data for the 3CR12 stainless steel sliding against WC-6 wt.% Co in synthetic mine water.

Sliding distance (m)	**Sample 1**	**Sample 2**	**Sample 3**	Average k (mm^3/N.m)	Standard deviation
	k (mm^3/N.m)	k (mm^3/N.m)	k (mm^3/N.m)		
53.24	0.0008037	0.0006201	0.0007128	0.0007122	9.178E-05
106.488	0.0007921	0.0008038	0.00073	0.0007753	3.965E-05
159.736	0.0007806	0.0007311	0.0007358	0.0007491	2.737E-05
212.984	0.0007892	0.0006746	0.0007214	0.0007284	5.764E-05
266.232	0.0007439	0.0006292	0.0007151	0.0006961	5.964E-05
319.48	0.0007117	0.0006105	0.0006898	0.0006707	5.326E-05

Table D. 13: Wear data for the WC-6 wt.% Co button sliding against mild steel counterfaces in distilled water.

Button	Wear Scar dia (mm)	Wear scar height (mm)	Volume loss (mm^3)	k (mm^3/N.m)	Contact Area (mm^2)	Ŧ Stress (MPa)
1	2.945	0.119	0.405	5.95E-06	5.285	40.303
2	3.167	0.137	0.542	7.97E-06	7.879	27.034
3	3.452	0.163	0.767	1.13E-05	9.358	22.761
Average values			0.571	8.39E-06		30.033
Standard deviation			0.149	2.68E-06		9.147

Table D. 14: Wear data for the WC-6 wt.% Co buttons sliding against mild steel counterfaces in synthetic mine water.

Button	Wear scar dia (mm)	Wear scar height (mm)	Volume loss (mm^3)	k (mm^3/N.m)	Contact Area (mm^2)	Ŧ Stress (MPa)
1	3.101	0.132	0.498	7.32E-06	7.553	28.20
2	3.461	0.164	0.775	1.14E-05	9.409	22.64
3	3.122	0.133	0.512	7.52E-06	7.656	27.82
Average values			0.595	8.74E-06		26.22
Standard deviation			0.127	2.29E-06		3.108

Table D. 15: Wear data of the WC-6 wt.% Co buttons sliding against 3CR12 stainless steel counterfaces in distilled water.

Button	Wear scar dia (mm)	Wear scar height (mm)	Volume loss (mm^3)	k (mm^3/N.m)	Contact Area (mm^2)	Stress (MPa) ŧ
1	3.395	0.158	0.717	1.05E-05	9.053	23.528
2	3.097	0.131	0.496	7.28E-06	7.535	28.268
3	3.114	0.133	0.507	7.44E-06	7.617	27.964
Average values			0.573	8.42E-06		26.587
Standard deviation			0.102	1.83E-06		2.653

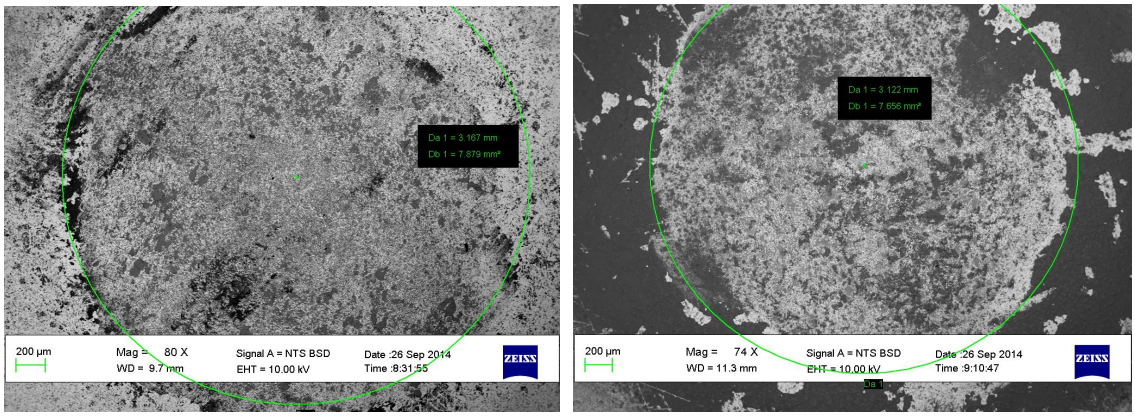
Table D. 16: Wear data for the WC-6 wt.% Co buttons sliding against 3CR12 stainless steel counterfaces in synthetic mine water.

Button	Wear scar dia (mm)	Wear scar height (mm)	Volume loss (mm^3)	k (mm^3/N.m)	Contact Area (mm^2)	ŧ Stress (MPa)
1	3.825	0.201	1.159	1.70E-05	11.49	18.538
2	3.851	0.204	1.191	1.75E-05	11.65	18.283
3	4.004	0.220	1.394	2.05E-05	12.59	16.918
Average values			1.248	1.83E-05		17.913
Standard deviation			0.104	1.87E-06		0.871

ŧ, the stress in Tables D.13 to D.16 are calculated using the area of the WC-6 wt.% Co wear scars

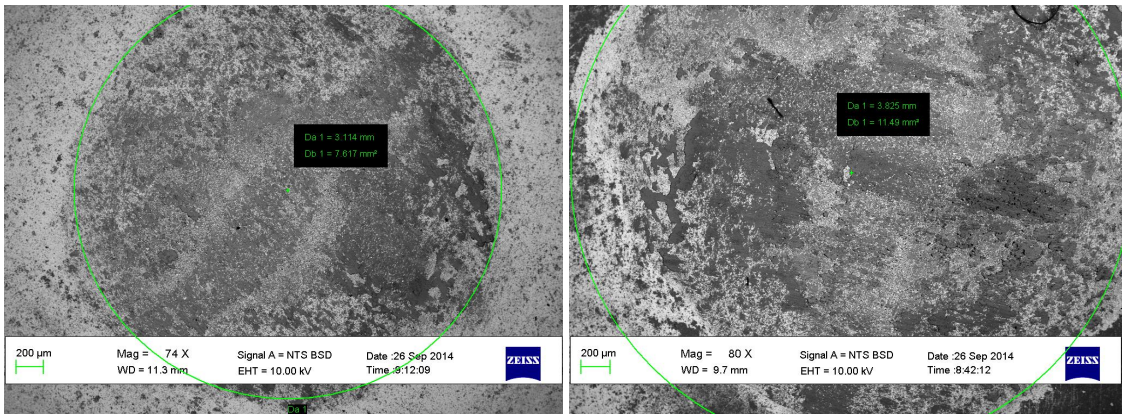
Appendix E: Contact areas of WC-6 wt.% Co buttons and steel counterfaces during wear testing

Figure E1 provides the typical wear scars obtained on the WC-6 wt.% Co at the point of contact and figure E2 the typical wear tracks produced on the steel counterfaces by the WC-6 wt.% Co during sliding.



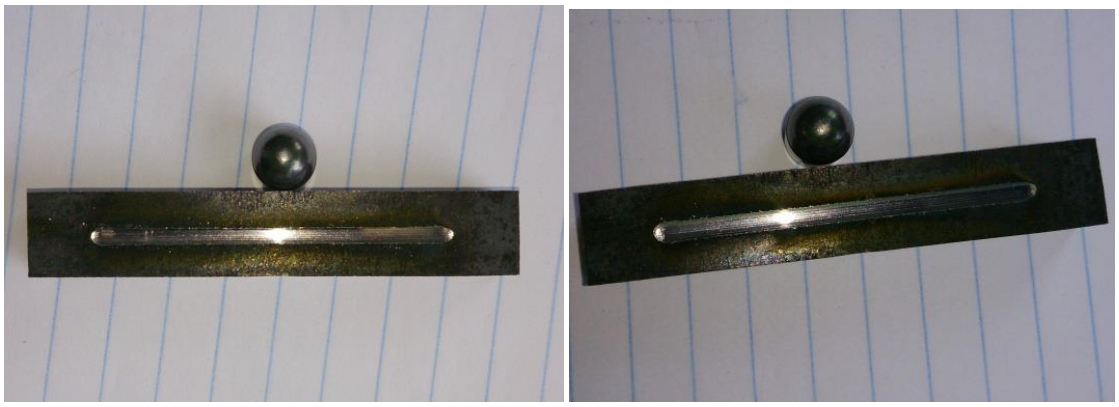
(a) (b)

Figure E. 1: Wear scar contact area for the WC-6 wt.% Co buttons sliding against mild steel in distilled water, (b) synthetic mine water.



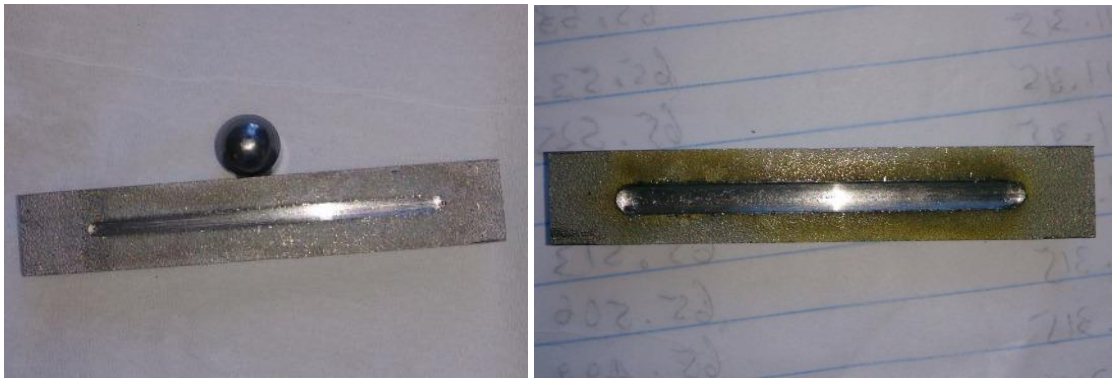
(a) (b)

Figure E. 2: Wear scar contact area for the WC-6 wt.% Co buttons sliding against 3CR12 stainless steel in (a) distilled water, (b) synthetic mine water.



(a) (b)

Figure E. 3: Wear tracks produced by the WC-6 wt.% Co buttons on mild steel in (a) distilled water, (b) synthetic mine water.



(a) (b)

Figure E. 4: Wear tracks produced by the WC-6 wt.% Co on 3CR12 stainless steel in (a) distilled water, (b) synthetic mine water.

Appendix F: Corrosion data and repeatability polarization curves

Appendix F, gives an outline of the corrosion data as well as the polarisation curves that were obtained during the corrosion tests.

Table F. 1: Corrosion data for the WC-6 wt.% Co buttons.

		I_{corr} (µA)	E_{corr} (mV)	Corrosion rate (10^{-3} mmpy)
Distilled water	Test 1	2.84	-0.32	17.6
	Test 2	1.25	-0.397	7.73
Average		2.045	-0.3585	12.665
Standard deviation		1.124	0.0544	6.979
Synthetic mine water	Test 1	5.14	-0.388	31.8
	Test 2	1.69	-0.443	10.5
Average		3.415	-0.4155	21.15
Standard deviation		2.439	0.03889	15.061

Table F. 2: Corrosion data for the 3CR12 stainless steel.

		I_{corr} (nA)	E_{corr} (mV)	Corrosion rate (10^{-3} mmpy)
Distilled water	Test 1	28.8	-0.161	0.943
	Test 2	8.46	-0.206	0.277
Average		18.63	-0.1835	0.61
Standard deviation		14.382	0.0318	0.471
Synthetic mine water	Test 1	221	-0.342	7.24
	Test 2	130	-0.374	4.26
Average		175.5	-0.358	5.75
Standard deviation		64.346	0.0226	2.107

Table F. 3: Corrosion data for the mild steel.

	I_{corr} (µA)	E_{corr} (mV)	Corrosion rate (10^{-3})mmpy
Distilled water	0.859	-0.6	30.2
Synthetic mine water	6.42	-0.562	225

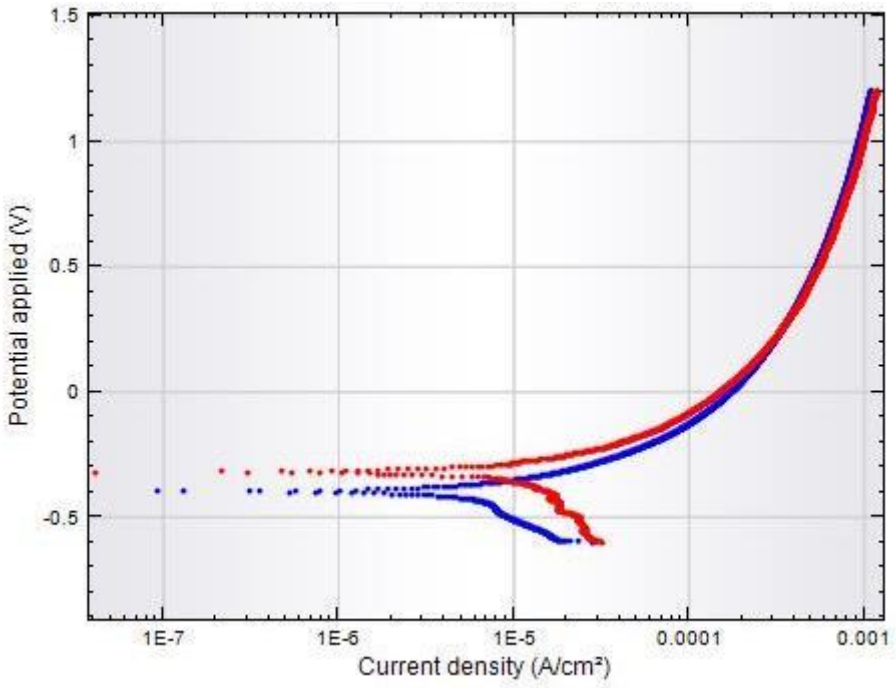


Figure F. 1: Polarisation curves for WC-6 wt.% Co showing repeatability in distilled water.

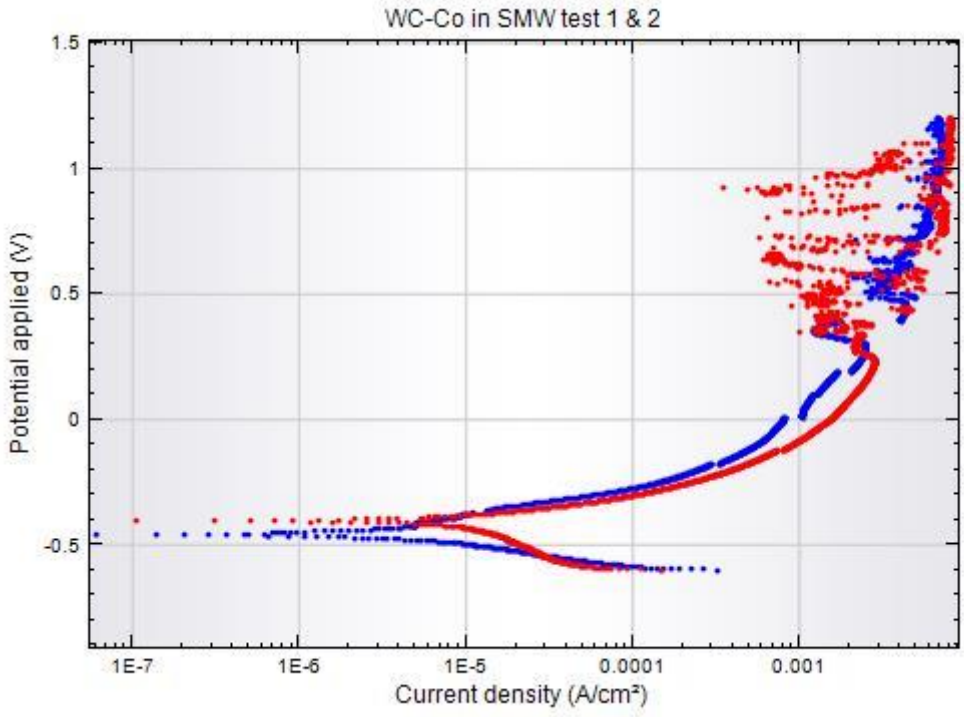


Figure F. 2: Polarisation curves for the WC-6 wt.% Co showing repeatability in synthetic mine water.

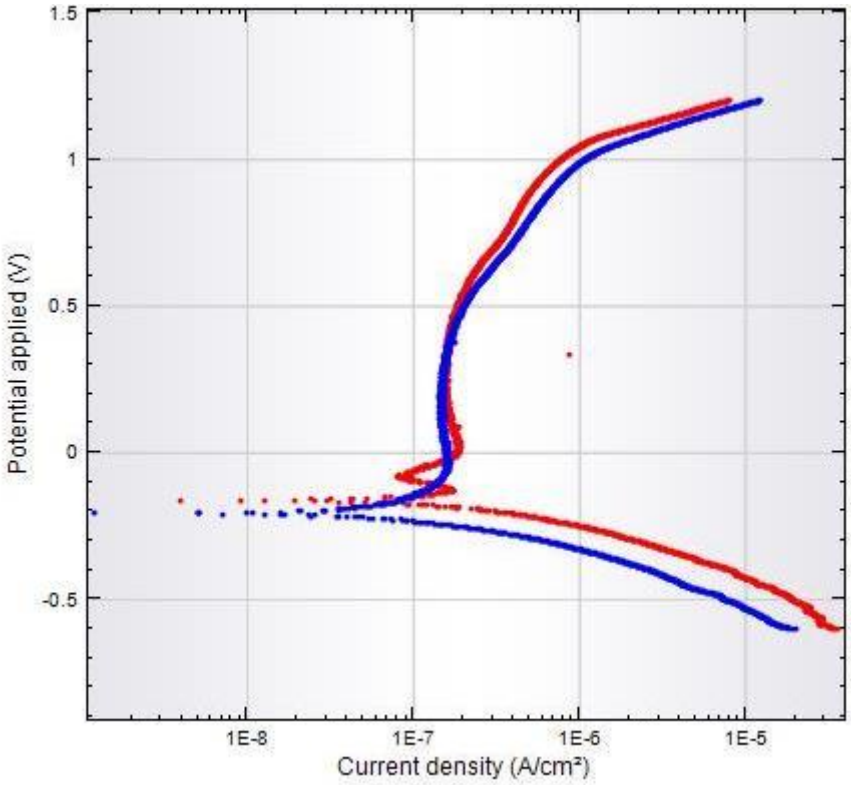


Figure F. 3: Polarisation curves for the 3CR12 stainless steel showing repeatability in distilled water.

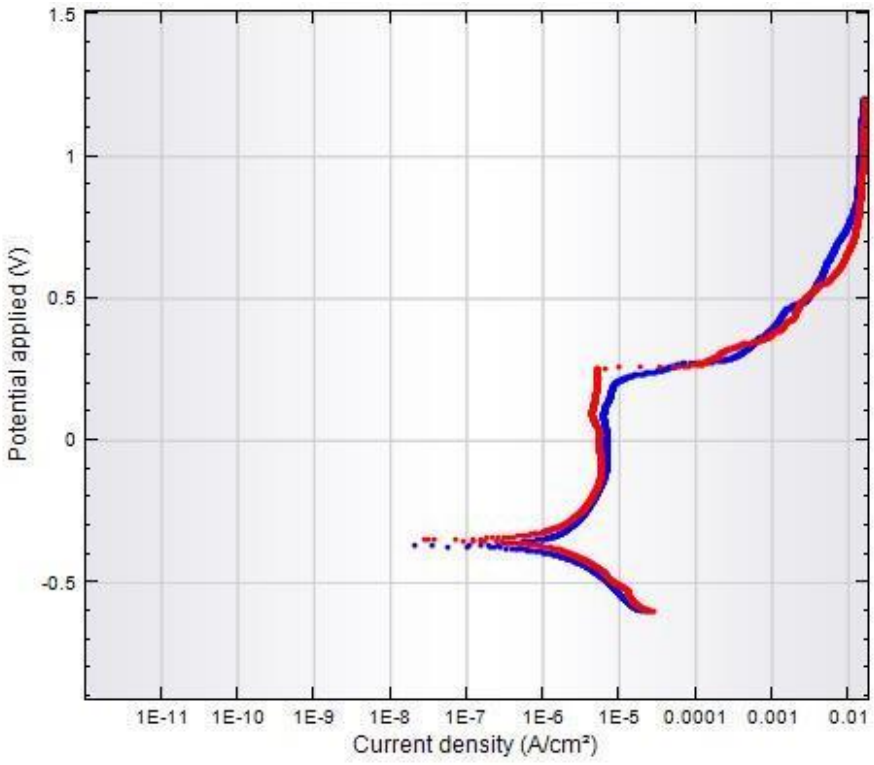


Figure F. 4: Polarisation curves for the 3Cr12 stainless steel showing repeatability in synthetic mine water.

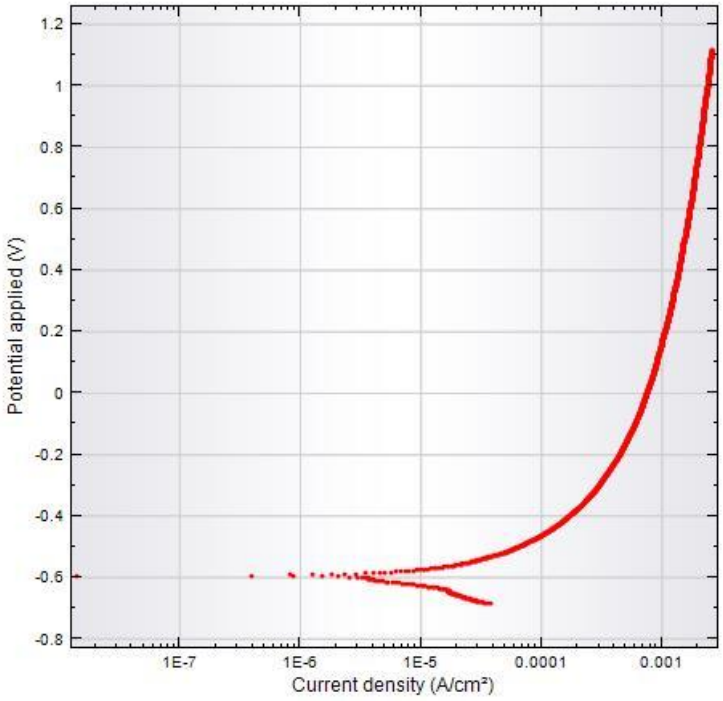


Figure F. 5: Polarisation curve for the mild steel in distilled water.

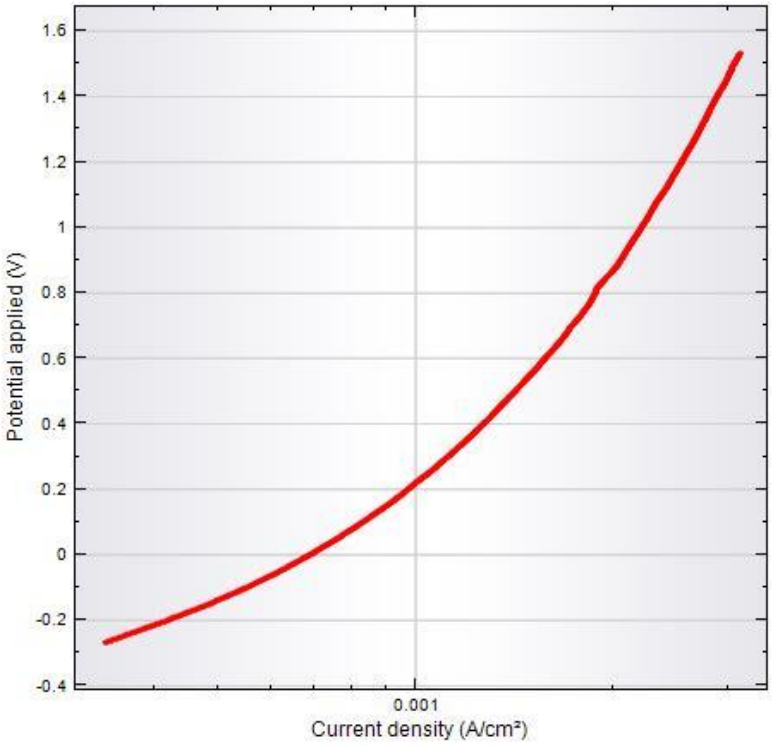


Figure F. 6: Polarisation curve for the mild steel in distilled water.

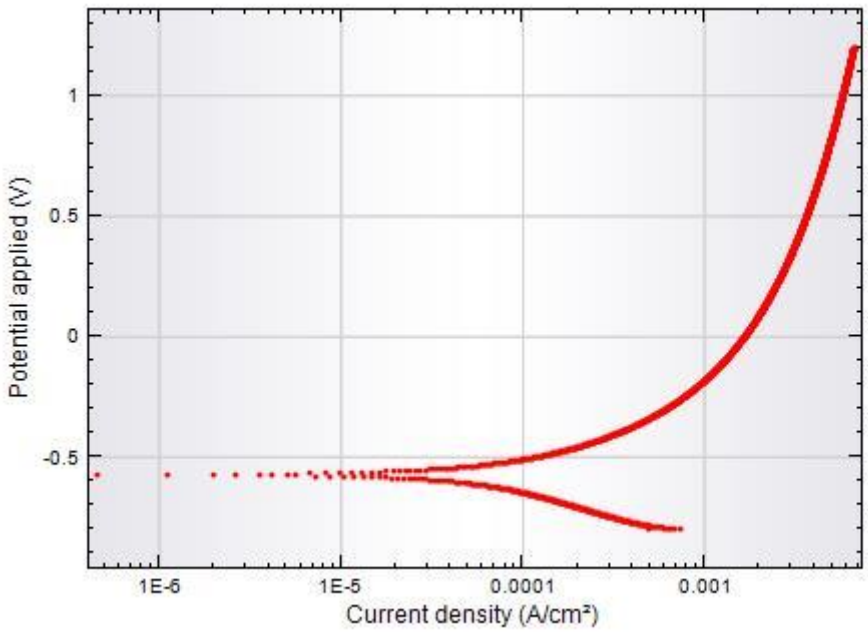


Figure F. 7: Polarisation curve for the mild steel in synthetic mine water.

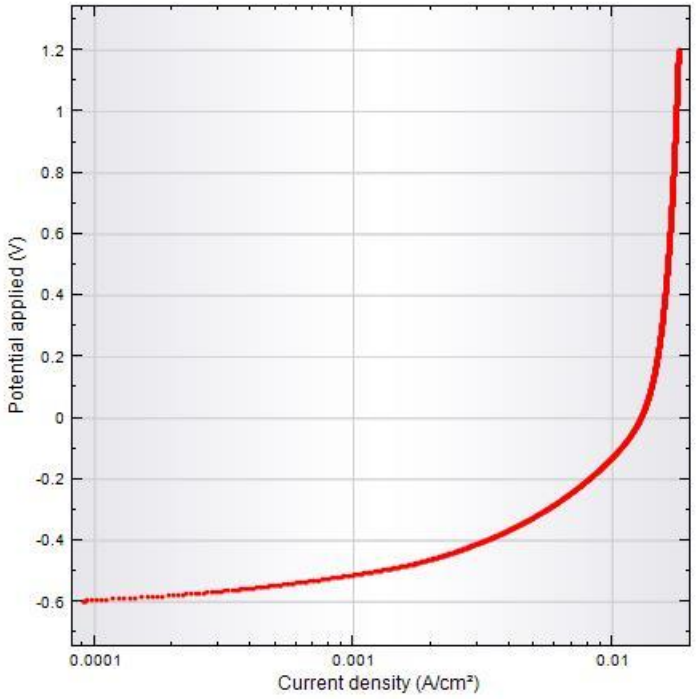
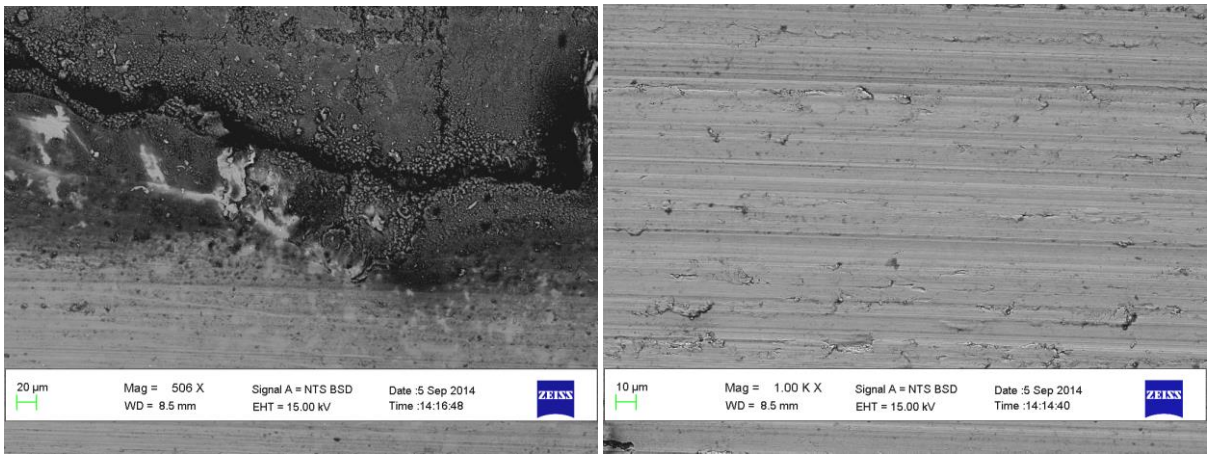


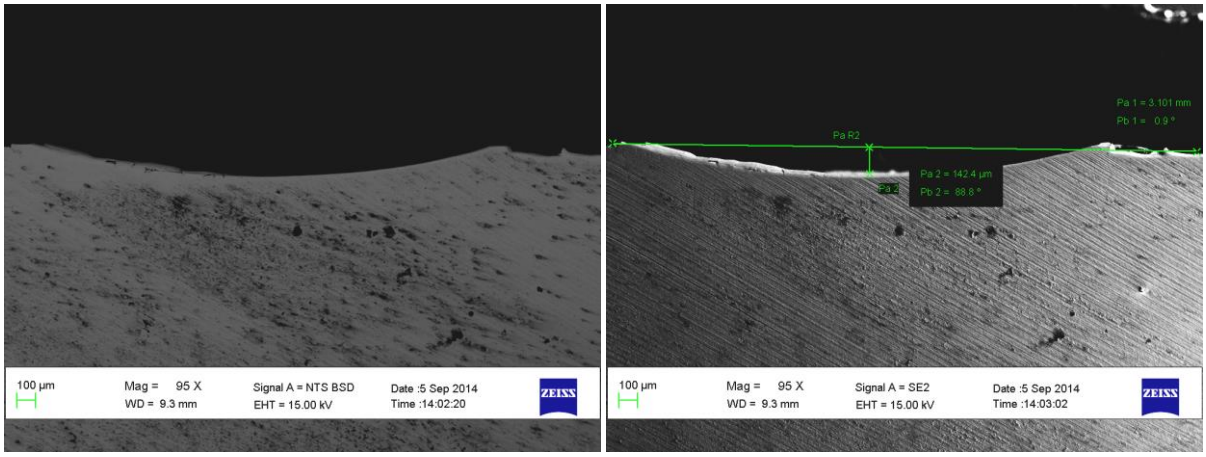
Figure F. 8: Polarization curve for the mild steel in synthetic mine water.

Appendix G: SEM images of the wear scars

Appendix G gives additional SEM wear scar images done to further understand and determine the wear mechanism on the materials tested.



(a). (b).



(c) (d)

Figure G. 1: Wear scars on mild steel sliding against WC-6 wt.% Co buttons in distilled water (a and b) Plane view, (c and d) cross section view.

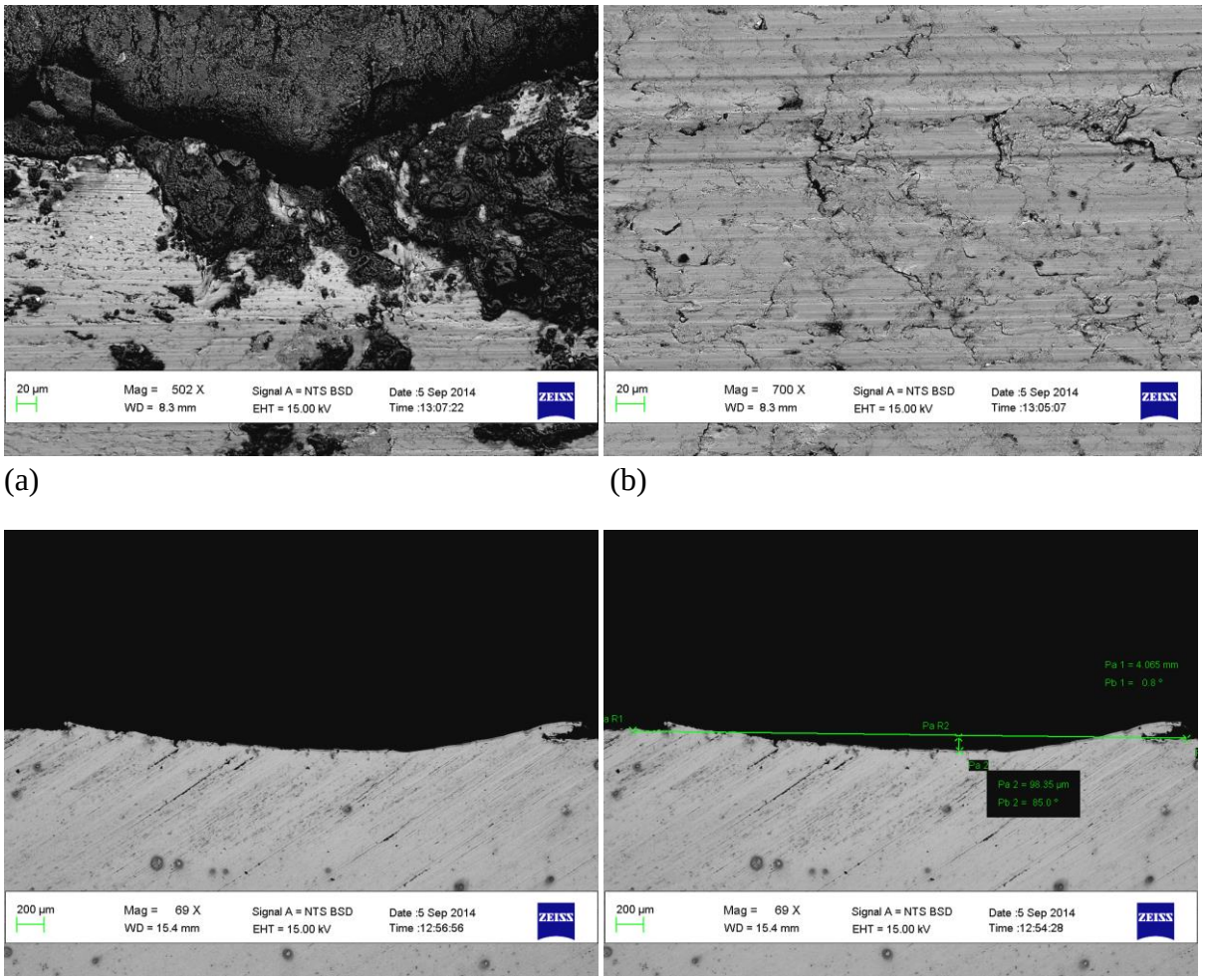


Figure G. 2: Wear scars on mild steel sliding against WC-6 wt.% Co buttons in distilled water (a and b) plane view, (C and d) cross section view)

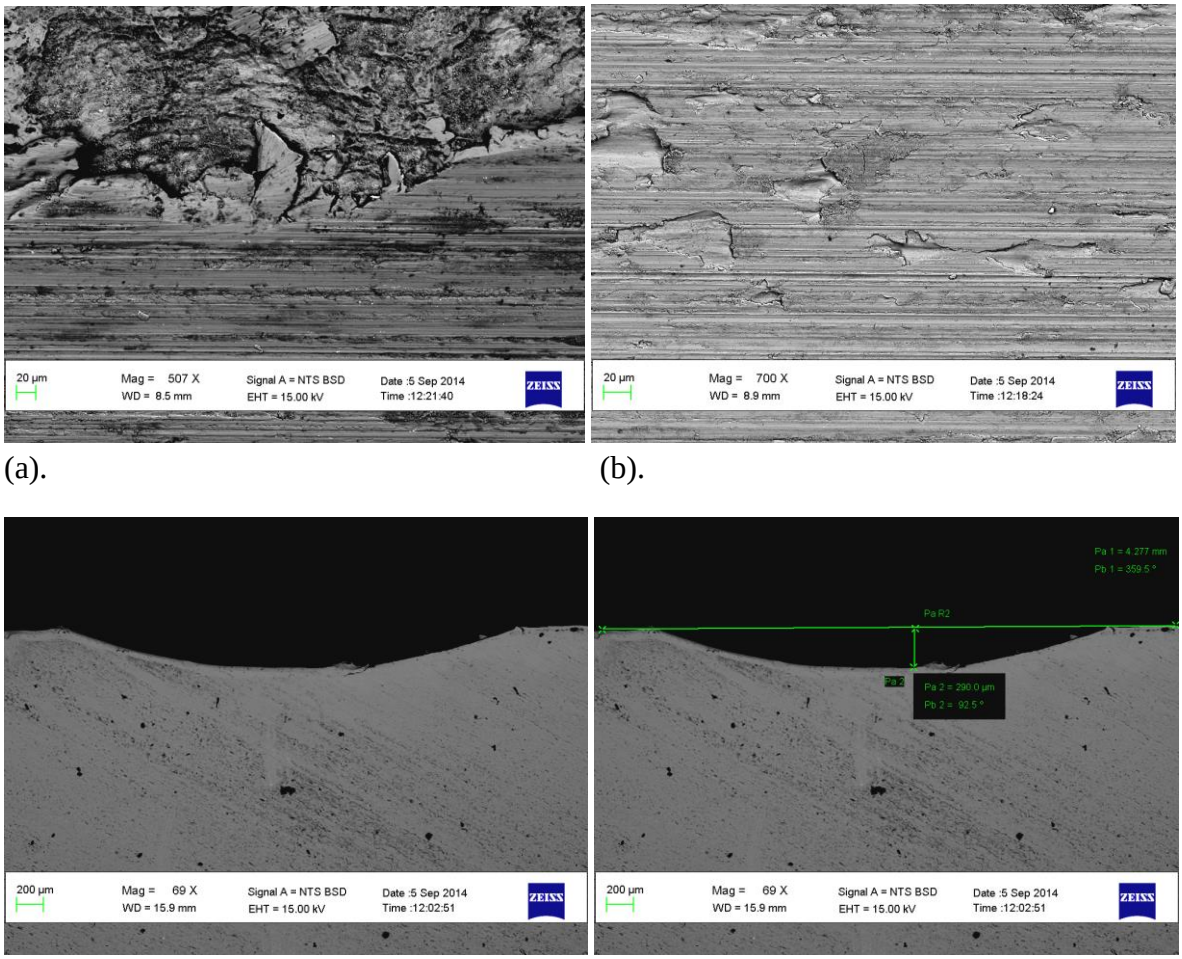


Figure G. 3: Wear scars on 3CR12 stainless steel sliding against WC-6 wt.% Co in distilled water (a and b) plane view, (c and d) cross section view.

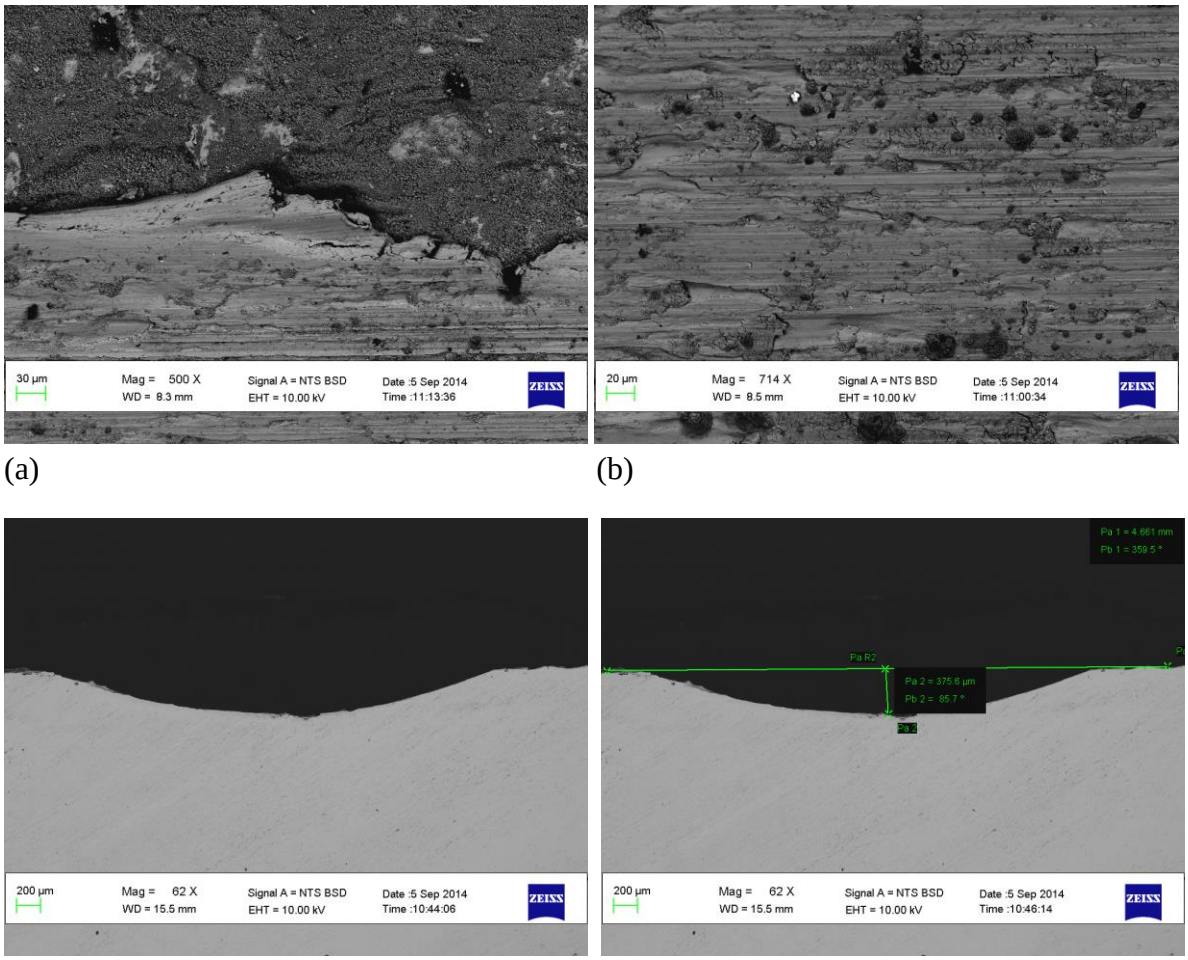


Figure G. 4: Wear scars on 3CR12 stainless steel sliding against WC-6 wt.% Co buttons in synthetic mine water (a and b) plane view, (c and d) cross section view.

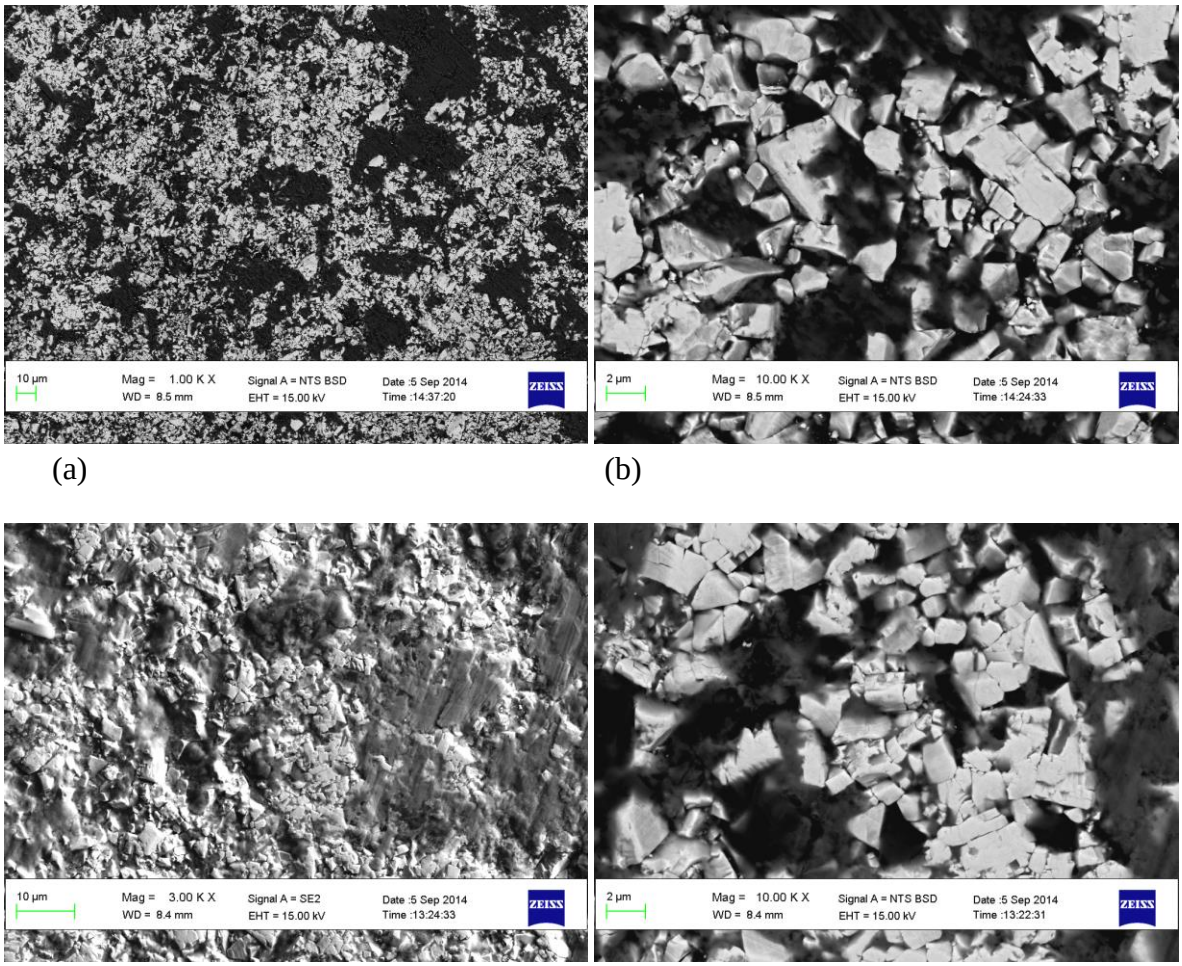


Figure G. 5: Wear scars on WC-6 wt.% Co sliding against mild steel in (a and b) distilled water, (c and d) synthetic mine water.

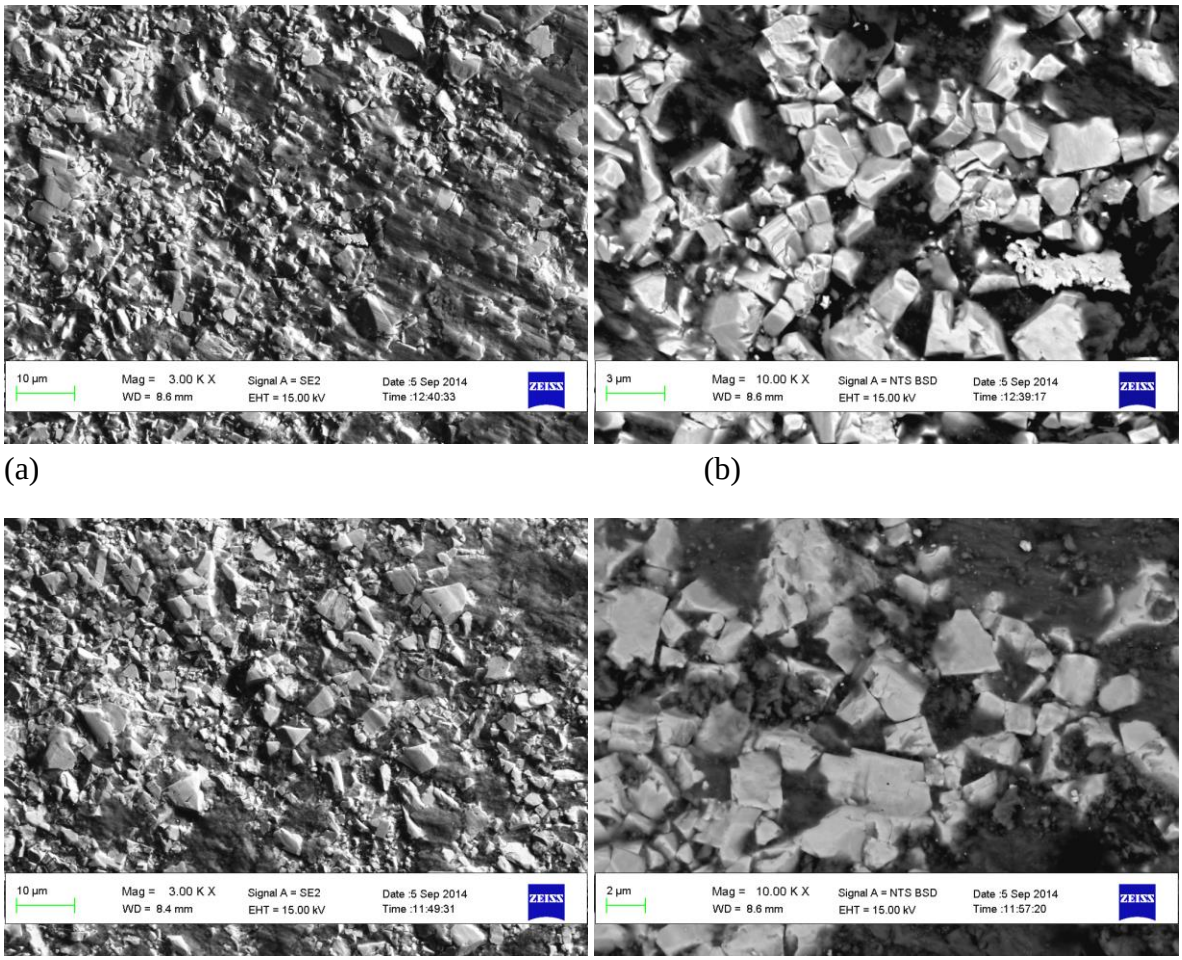


Figure G. 6: Wear scars on WC-6 wt.% Co sliding against 3CR12 stainless steel in (a and b) distilled water, (c and d) synthetic mine water.

Appendix H: Corrosion surface

This appendix shows the corrosion surface of the 3CR12 stainless steels.

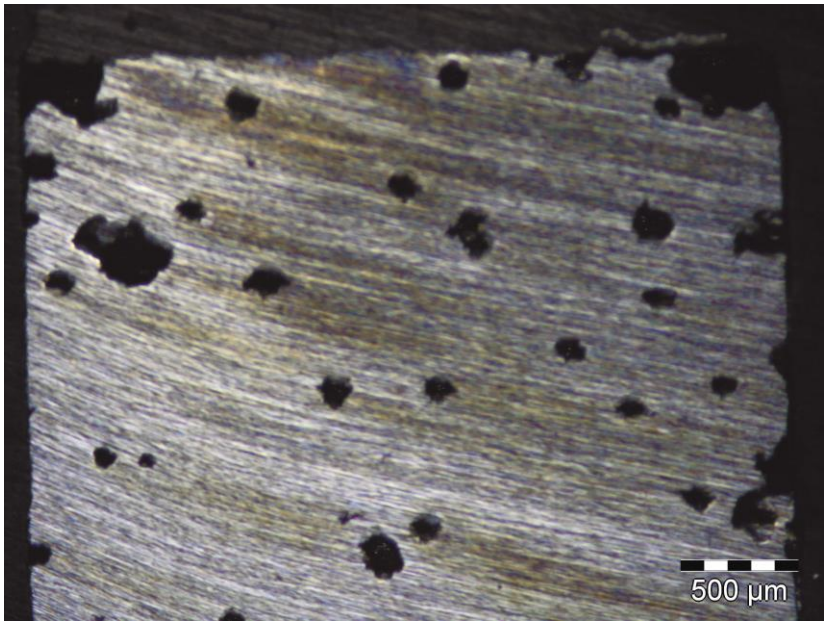


Figure H. 1: Corroded surface for the 3CR12 stainless steel.